

CRYSTAL STRUCTURE PREDICTION BASED ON DENSITY FUNCTIONAL THEORY

Inauguraldissertation

zur
Erlangung der Würde eines Doktors der Philosophie
vorgelegt der
Philosophisch–Naturwissenschaftlichen Fakultät
der Universität Basel
von

Maximilian Kei Amsler
aus Bözen, Aargau

Basel, 2014

Originaldokument gespeichert auf dem Dokumentenserver der Universität Basel
edoc.unibas.ch



Dieses Werk ist unter dem Vertrag "Creative Commons Namensnennung – Keine kommerzielle Nutzung – Keine Bearbeitung 3.0 Schweiz" lizenziert. Die vollständige Lizenz kann unter creativecommons.org/licences/by-nc-nd/3.0/ch eingesehen werden.

Genehmigt von der Philosophisch-Naturwissenschaftlichen Fakultät
auf Antrag von:

Prof. Dr. Stefan Goedecker

Dr. Luigi Genovese

Basel, den 22. Mai 2012

Prof. Dr. Martin Spiess
Dekan



Namensnennung – Keine kommerzielle Nutzung – Keine Bearbeitung 3.0 Schweiz (CC BY-NC-ND 3.0 CH)

Sie dürfen: **Teilen** – den Inhalt kopieren, verbreiten und zugänglich machen

Unter den folgenden Bedingungen:



Namensnennung – Sie müssen den Namen des Autors/Rechteinhabers in der von ihm festgelegten Weise nennen.



Keine kommerzielle Nutzung – Sie dürfen diesen Inhalt nicht für kommerzielle Zwecke nutzen.



Keine Bearbeitung erlaubt – Sie dürfen diesen Inhalt nicht bearbeitet, abwandeln oder in anderer Weise verändern.

Wobei gilt:

- **Verzichtserklärung** – Jede der vorgenannten Bedingungen kann aufgehoben werden, sofern Sie die ausdrückliche Einwilligung des Rechteinhabers dazu erhalten.
- **Public Domain (gemeinfreie oder nicht-schützbare Inhalte)** – Soweit das Werk, der Inhalt oder irgendein Teil davon zur Public Domain der jeweiligen Rechtsordnung gehört, wird dieser Status von der Lizenz in keiner Weise berührt.
- **Sonstige Rechte** – Die Lizenz hat keinerlei Einfluss auf die folgenden Rechte:
 - Die Rechte, die jedermann wegen der Schranken des Urheberrechts oder aufgrund gesetzlicher Erlaubnisse zustehen (in einigen Ländern als grundsätzliche Doktrin des fair use bekannt);
 - Die **Persönlichkeitsrechte** des Urhebers;
 - Rechte anderer Personen, entweder am Lizenzgegenstand selber oder bezüglich seiner Verwendung, zum Beispiel für Werbung oder Privatsphärenschutz.
- **Hinweis** – Bei jeder Nutzung oder Verbreitung müssen Sie anderen alle Lizenzbedingungen mitteilen, die für diesen Inhalt gelten. Am einfachsten ist es, an entsprechender Stelle einen Link auf diese Seite einzubinden.

To my parents, my sister and my friends

Contents

1	Introduction	1
2	Energy Landscapes	5
2.1	Density Functional Theory	6
2.1.1	The many-body Schrödinger equation	8
2.1.2	Kohn-Sham formalism	10
2.1.3	Functionals	11
2.1.4	Forces and stresses	12
2.2	Correlation of search space with PES accuracy: a case study on silicon . .	14
2.2.1	Characterizing the potential energy surface of the Si ₁₆ cluster by MHM efficiency	15
2.2.2	Average curvatures of the PES at local minima	15
2.2.3	Configurational density of states in bulk silicon	17
2.2.4	Summary	20
3	Structure prediction	21
3.1	Local geometry optimization	21
3.1.1	Steepest descent	23
3.1.2	BFGS	24

3.1.3	FIRE	26
3.1.4	Comparison of geometry optimization methods	27
3.2	Global structural optimization methods	29
3.2.1	Database searching and data mining	30
3.2.2	Simulated annealing	31
3.2.3	Metadynamics	32
3.2.4	Basin hopping	33
3.2.5	Genetic algorithm	34
3.2.6	Particle swarm optimization	35
3.2.7	Random search	37
3.3	Minima hopping method	38
3.3.1	The algorithm	39
3.3.2	Minima hopping method vs. other methods	40
3.3.3	Generalization to periodic systems	42
3.3.4	Softening and optimizing cell parameters	44
3.3.5	Seeding initial structures	46
3.3.6	Parallelization and lattice vector prediction	49
3.3.7	Volume constraints	53
4	Applications	55
4.1	Structure of Binary Lennard-Jones Mixtures	56
4.1.1	Parametrization of the Lennard-Jones potential	56
4.1.2	Putative ground state structures	58
4.1.3	Summary	59
4.2	Crystal Structure of Cold Compressed Graphite	60
4.2.1	Structural identification and formation mechanism	60

4.2.2	Energetic, dynamical and electronic properties	63
4.2.3	Experimental evidences	64
4.2.4	Summary	67
4.3	High pressure structures of disilane and their superconducting properties .	69
4.3.1	Screening high-pressure phases with Lenosky tight-binding	69
4.3.2	Superconductivity and dynamical stability of the <i>Cmcm</i> phase . . .	72
4.3.3	Summary	75
4.4	Novel structural motifs in low energy phases of LiAlH_4	76
4.4.1	Structural search	77
4.4.2	Characterization of the $p\text{-}P2_1/c$ phase	78
4.4.3	Low temperature synthesis of polymeric LiAlH_4	81
4.4.4	Summary	82
5	Conclusions and Outlook	85
A	Stress and strain	89
B	Derivation of the Parrinello-Rahman equation's of motion	91
C	E_{diff} parameter	94
D	Additional material for Disilane	95
D.1	Dynamical stability and the structural evolution with pressure	95
D.2	Superconductivity	96
D.3	Raman and IR activity	100
E	Additional material for LiAlH_4	103
E.1	Structural data	103
E.2	Neutron diffraction	108

INTRODUCTION

In solids, the arrangement of the constituent atoms in the crystal structure fundamentally determines almost all properties of a material. The possibility to resolve structures and to create three-dimensional models of crystals became possible by the discovery of X-rays by Wilhelm Conrad Röntgen in 1895. Shortly thereafter, major advances were achieved in crystallography, especially based on the work of Max von Laue and William Lawrence Bragg with the development of X-ray diffraction techniques in the early 20th century.

Knowing the crystal structure is absolutely mandatory for any further theoretical investigations of a material and is the foundation for *ab initio* modeling of a large number of its properties. Predicting the crystal structure of an unknown material even before it is synthesized is therefore the fundamental target in computational materials design. However, the complexity of this task is immense and its feasibility has been questioned until a couple of decades ago [1]. Within the recent years, new structural search algorithms have been proposed and, thanks to increasing computational resources at hand, have been successfully applied to various materials.

The potential of computational crystal structure prediction and materials design is based on its flexibility, speed and low financial cost. Where experimental design and synthesis of a single novel material is a complex and time-consuming process with no guarantee of success, a carefully designed computational prediction scheme can scan multiple compounds at different compositions and conditions at the same time. For example experiments at extreme conditions such as high pressure or temperature environments as they exist in planetary cores quickly become economically unaffordable, or the conditions under study simply cannot be created in the laboratory due to technical limitations. With computer simulations however such conditions can be easily modeled in a virtual laboratory. The economical benefits of employing such computational tools have not only been recognized in materials design, but also in biology and pharmacy where the demand for efficient and reliable structure prediction methods is rapidly increasing [2, 3].

A very common and simple way of predicting favorable crystal structures is extracting structural information of similar known materials from databases. The energetically most stable structure is identified and gives the putative ground state. However, this approach has a limited success rate when the ground state is an unknown structure, which can only be found by performing an extensive search. Similarly, data mining is capable of predicting new crystalline structures based on a set of experimental data and/or *ab initio* calculations [4, 5, 6, 7]. However, a completely unconstrained and flexible search method would be preferable which can go beyond the predefined structures in a database.

Recently, more advanced methods for crystal structure prediction have been developed and applied, which allow a systematic search for the ground state structure based solely on the system's composition and the external conditions. The most promising of these methods and their applications on crystal structure prediction include random search, simulated annealing, genetic algorithms and metadynamics. The minima hopping method (MHM) was designed in 2004 as an alternative approach [8]. It allows an efficient exploration of a high dimensional potential energy surface (PES) of complex systems, while progressing toward the global minimum structure, and has been successfully applied to various isolated systems such as Lennard-Jones and silicon clusters [8, 9, 10], fullerene materials [11, 12], complex biological molecules [13] and large gold clusters [14]. The MHM has also been used in other applications, such as providing realistic atomic force microscopy (AFM) tips for AFM simulations [15, 16, 17]. In this thesis we present a generalization of the MHM to periodic systems with pressure and volume constraints, and its application to the following materials:

- Binary Lennard-Jones mixtures were investigated with cells up to 320 particles. These benchmark system were initially designed to model glassy energy landscapes and thus pose great challenges for any crystal structure prediction method. With the MHM we were able to identify many structures which are much lower in energy than any previous predictions, demonstrating its predictive power even for extremely hard optimization problems.
- Motivated by above results, we then studied carbon systems under pressure directly at the density functional theory level. Unexplained optical, electronic and structural changes in high pressure experiments of cold compressed graphite indicate the existence of a novel carbon phase. Several theoretical structures of this phase have been proposed in literature, such as *M*-carbon, *W*-carbon or bct- C_4 -carbon. With MHM simulations we identified two novel carbon allotropes, *M10*-carbon and *Z*-carbon. In a close collaboration with an experimental group in Lyon, France, we found evidences in the Raman spectrum of compressed graphite that *Z*-carbon is indeed the most promising structure among all previously proposed candidates.
- Hydrogen is a highly promising candidate in the ongoing search for high temperature superconductors. However, metalization of hydrogen requires extremely high

pressures, inaccessible with today's technical capabilities. Chemical pre-compression of hydrogen together with heavier elements in a compound was proposed as a possible pathway towards high T_c superconductivity. We investigated disilane, a readily available and therefore promising candidate material, and identified a novel crystalline metallic phase which is stable against elemental decomposition above roughly 100 GPa. In contrast to earlier predictions, our investigations reveal that disilane shows a moderate electron-phonon coupling and a T_c of about 20K at 100 GPa. This result is in good agreement with other investigations in similar silane materials.

- Hydrogen has been touted as a promising alternative energy source due to its clean reaction with oxygen without producing greenhouse gases. For mobile applications in fuel cell vehicles a safe, reversible and energetically dense hydrogen storage material is required. LiAlH_4 is a promising candidate with more than 10wt% hydrogen contents. However, its instability towards decomposition during long storage periods remains a problematic issue for practical applications. To address this problem we performed a systematic structural search within the density functional theory framework and identified a whole class of low-energy phases. Instead of the molecular ionic configuration commonly encountered in such metal hydrides, these novel phases contain polymeric AlH_4 -substructures. Their discovery and possible production in low temperature synthesis might have a profound impact on the stability and hydrogenation/rehydrogenation properties of LiAlH_4 .

This thesis is structured as follows. In chapter 2 we give an overview on how to characterize energy landscapes. The density functional theory is briefly described, as it is used in subsequent sections and in chapter 4 to make accurate predictions of crystal structures. A comparative study on different descriptions of the energy landscapes of silicon systems are presented at the end of the chapter. In chapter 3, the efficiency of local geometry relaxations schemes are described and compared in the framework of the MHM. Various approaches and techniques in crystal structure prediction schemes are discussed in section 3.2. We then present how the MHM is generalized for periodic systems in section 3.3. Several schemes to improve the efficiency of the MHM are discussed in detail. Finally, chapter 4 contains the applications of the MHM, based on *ab initio* calculations.

The major part of this thesis has been published in different peer reviewed journals. Section 2.2 has been partially published in Physical Review B [18], whereas parts of section 3.3 and 4.1 have been published in the Journal of Chemical Physics [19]. The applications on cold compressed graphite (section 4.2), disilane (section 4.3) and the work on LiAlH_4 (section 4.4) have been separately published in Physical Review Letters [20, 21, 22] and in the European Physical Journal B [23].

ENERGY LANDSCAPES

One of the most fundamental properties in computational modeling of a compound is its (free) energy as a function of internal degrees of freedom, the potential energy surface (PES), also referred to as Born-Oppenheimer surface. In an isolated system these coordinates are the atomic positions, whereas in crystals the lattice parameters contribute as well. A majority of physical properties can be derived from the knowledge of how the energy depends on these degrees of freedom. Stationary points on the PES are of utmost importance, especially for studying structures and thermodynamics of a compound. Such points correspond to a set of atomic and cell coordinates at which the gradient of the energy vanishes. The second order partial derivatives of the energy, which are combined in the Hessian matrix, can be used for further characterization. Local minima correspond to stable structures at which all eigenvalues of the Hessian are positive, and the energetic ordering of the minima indicates the thermodynamic stability of the different phases. Second order derivatives of stable structures also determine the phonons, bulk moduli and compressibility of a phase. Electronic properties such as band-structures and optical properties can be computed using *ab initio* methods. On the other hand, the barrier heights of transition states connecting two minima give rise to the kinetics of the system, such as diffusion coefficients or defect formation. Such transition states are essentially first order saddle points on the energy landscape, where the gradients vanish and the Hessian matrix contains exactly one negative eigenvalue. Methods to find such transition states are for example nudged elastic band [24, 25], the string method [26, 27], the splined saddle method [28] or the enhanced splined saddle method [29], which have been widely discussed in literature.

The PES can be subdivided into regions each uniquely related to a local minimum. Such a region, called basin of attraction or catchment basin, is defined as the set of configurations on the PES which end up at the identical final structure when used as a starting point for a small step-size steepest descent relaxations. A set of neighboring basins is defined as a super-basins. A super-basin is called a funnel if the lowest local minimum within

the super-basin can be reached from any other basin without crossing barriers that are very high. The barrier heights should not be larger than the average difference in energy between the local minima within the funnel. Systems containing multiple funnels are an especially big challenge for global geometry optimization algorithms.

Energy landscapes can be characterized by analyzing the energetic distribution of local minima and the transition states connecting them. In systems described by PES' with staircase-like forms, where only one funnel exists and very few local minima have competitively similar energies separated by low barriers, the ground state can be easily found with any crystal structure prediction scheme. Thus, such systems are referred to as structure seekers. Ionic crystals such as simple salts fall within this category. On the other hand, PES' with a sawtooth topography, where a large amount of structures have very similar energies populating several funnels with no well defined global minimum, lead to amorphous, glassy structures and are therefore referred to as glass formers. It is a challenging task to perform global optimization on such systems [30, 31]. Disconnectivity graphs [30] are a helpful tool to characterize energy landscapes. In the tree-like graphs, where the vertical axis represents the energy, every branch corresponds to a local minimum in the system. A collection of minima within the same super-basin is combined to a single branch, where the connecting node corresponds to a threshold barrier height. These nodes can be further combined to higher energy nodes, which then represent funnels. The overall shape of the disconnectivity graphs is characteristic for a specific system, where "palm-tree" shaped graphs correspond to structure seekers, and "banyan-tree" graphs represent glass formers. An example for two model energy landscapes is shown in Figure 2.1

In principle, the exact PES can be obtained by solving the many-body Schrödinger equation to obtain the ground state wave-function within the Born-Oppenheimer approximation. However, this is not feasible for any realistic material and approximative methods have to be employed. Up to several hundred atoms can be treated within the density functional theory. Semi-empirical methods, such as Tight-Binding, are required for simulations on even larger scales, which use further approximations and empirical parametrization at the cost of accuracy. Force fields completely neglect quantum mechanical treatment of the electrons. The energy landscape is represented in an analytical form which is parametrized based on experimental data or highly accurate quantum mechanical calculations. Most force fields contain two- and three-body interactions, which include bond-stretching, bond-bending and torsional terms. Although systems with millions of atoms can be treated with force fields, a good parametrization is mandatory for meaningful results, and they are very often not transferable to configurations far beyond the fitting database.

2.1 Density Functional Theory

A system with N electrons can in principle be fully described by solving the stationary many-body Schrödinger equation. Due to the complexity of the problem, even for systems

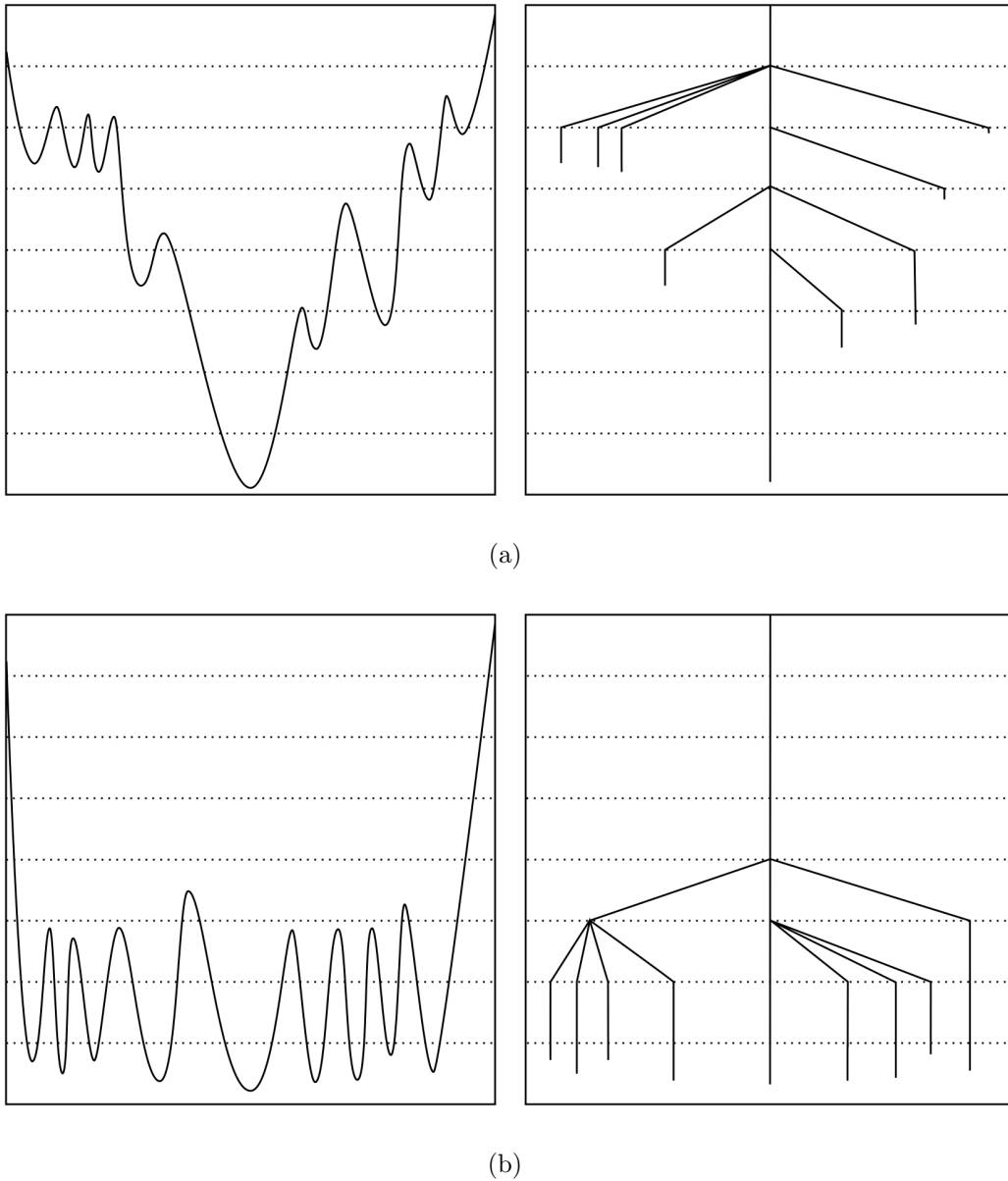


Figure 2.1: Disconnectivity graphs can visualize the characteristics of an energy landscape. Two different model systems are shown in this plot. Panel (a) describes a structure seeker and resembles a palm-tree. The global minimum is well defined, and the barriers heights decrease simultaneously with the energies of the local minima. Panel (b) represents a glassy energy landscape with a “banyan-tree” disconnectivity graph. Several minima compete with the ground state, and the funnels are separated by large energy barriers compared to the energy differences of the local minima.

with a small number of electrons approximate methods have to be employed. Instead of treating the $3N$ -dimensional many-body wave-function, the density functional theory (DFT) operates in the electronic charge density with 3 spatial dimensions and the electrons are treated as independent particles in a mean-field theory. Due to its good description of structural properties of a large variety of materials at moderate computational cost it has become one of the most widely used methods in condensed matter physics [32, 33].

2.1.1 The many-body Schrödinger equation

The time-independent non-relativistic Schrödinger equation is given by

$$\hat{H}_{tot}\Psi_i(\mathbf{x}_1, \dots, \mathbf{x}_N, \mathbf{R}_1, \dots, \mathbf{R}_M) = E_{tot,i}\Psi_i(\mathbf{x}_1, \dots, \mathbf{x}_N, \mathbf{R}_1, \dots, \mathbf{R}_M) \quad (2.1)$$

\mathbf{r}_i and \mathbf{R}_i denote the spacial coordinates of the N electron and M nuclei in the system, respectively, while \mathbf{x}_i contains both spacial and the spin coordinates s_i of the electrons, $\mathbf{x}_i \equiv \mathbf{r}_i, s_i$. Ψ_i represents the wave-function of the i -th quantum state¹. Since the 0-th quantum state (the ground state) and the corresponding energy are generally of most interest we will hereon omit the index i unless required. \hat{H}_{tot} is the full Hamiltonian (in atomic units: $\hbar = m_e = e = 4\pi\epsilon_0 = 1$)

$$\hat{H}_{tot} = -\frac{1}{2} \sum_{i=1}^N \nabla_i^2 - \frac{1}{2} \sum_{A=1}^M \frac{1}{M_A} \nabla_A^2 - \sum_{i=1}^N \sum_{A=1}^M \frac{Z_A}{|\mathbf{r}_i - \mathbf{R}_A|} + \sum_{i=1}^N \sum_{j<i}^N \frac{1}{|\mathbf{r}_i - \mathbf{r}_j|} + \sum_{A=1}^M \sum_{B<A}^M \frac{Z_A Z_B}{|\mathbf{R}_A - \mathbf{R}_B|} \quad (2.2)$$

i and j run over the N electrons, whereas A and B run over the M nuclei. The first term represents the kinetic energy of the electrons, and the second term the kinetic energy of the nuclei. The third term describes the attractive electron-nucleus interaction, whereas the terms four and five describe the electron-electron and nucleus-nucleus Coulomb repulsion. Within the Born-Oppenheimer approximation the nuclei are treated as classical particles, such that the kinetic nuclei energies are neglected. Because of the large difference in their masses, the nuclei move much slower compared to the electrons. Therefore, the electrons can be described to move in the fixed potential coming from the nuclei. The last term is independent of the electronic coordinates and can be treated separately by only taking into account the nuclear repulsion energy

$$E_{nn} = \sum_{A=1}^M \sum_{B<A}^M \frac{Z_A Z_B}{|\mathbf{R}_A - \mathbf{R}_B|} \quad (2.3)$$

The electronic Hamiltonian is thus given by

$$\hat{H} = -\frac{1}{2} \sum_{i=1}^N \nabla_i^2 - \sum_{i=1}^N \sum_{A=1}^M \frac{Z_A}{|\mathbf{r}_i - \mathbf{R}_A|} + \sum_{i=1}^N \sum_{j<i}^N \frac{1}{|\mathbf{r}_i - \mathbf{r}_j|} = \hat{T} + \hat{V}_{en} + \hat{V}_{ee} \quad (2.4)$$

¹for convenience we assume that all wave-functions are normalized such that $\langle \Psi_i | \Psi_i \rangle = 1$

with the corresponding Schrödinger equation

$$\hat{H}\Psi = E\Psi \quad (2.5)$$

and the total energy is then

$$E_{tot} = E + E_{nn} \quad (2.6)$$

The high dimensionality of a quantum state $\Psi = \Psi(\mathbf{x}_1, \mathbf{x}_2, \dots, \mathbf{x}_N)$ makes it an impracticable object to deal with. Within the density functional theory, one uses the charge density as the basic quantity which is expressed in 3 spatial coordinates. This quantity is physically measurable and describes how the electronic charge is distributed in space. It is obtained by integrating over all spacial and spin coordinates in Ψ except for a one-electron spacial coordinate \mathbf{r}_1 :

$$\rho(\mathbf{r}_1) = N \int \dots \int |\Psi(\mathbf{x}_1, \mathbf{x}_1, \dots, \mathbf{x}_N)|^2 ds_1, d\mathbf{x}_2, d\mathbf{x}_3, \dots, d\mathbf{x}_N \quad (2.7)$$

with the normalization constraints

$$\rho(\mathbf{r} \rightarrow \infty) = 0 \quad \text{and} \quad \int_{-\infty}^{\infty} \rho(\mathbf{r}) d\mathbf{r} = N \quad (2.8)$$

where N is the total number of electrons in the system. Its interpretation is that an electron can be expected to be found in a volume element $d\mathbf{r}$ at \mathbf{r} with the probability of $\rho(\mathbf{r})d\mathbf{r}$.

The density functional theory is based on the fact that the many-body Schrödinger equation can in principle be solved exactly from a density functional. Hohnberg and Kohn showed in 1964 that there is a direct mapping of the ground state charge density $\rho(\mathbf{r})$ and the external potential V_{en} (to within a constant) [34]. In particular, since the potential itself determines the hamiltonian \hat{H} , all properties of the system are uniquely defined by the ground state charge density $\rho(\mathbf{r})$. The proof is straight forward. Assume that two external potentials V_{en}^1 and V_{en}^2 , which differ by more than a constant, give the identical charge density $\rho(\mathbf{r})$. They will lead to two different Hamiltonians \hat{H}^1 and \hat{H}^2 , and thus give rise to two different normalized ground state wave-functions Ψ_0^1 and Ψ_0^2 , which however have the same charge density. The variational principle states that the expectation value of the energy $E[\Psi] = \langle \Psi | \hat{H} | \Psi \rangle$ of an arbitrary state Ψ is greater or equal to the ground state energy $E[\Psi_0]$ given by the true ground state wave-function Ψ_0 . Since Ψ_0^2 is not the ground state of \hat{H}^1 , the energy expectation value will be higher if the ground state is not degenerate:

$$E_1 = \langle \Psi_0^1 | \hat{H}^1 | \Psi_0^1 \rangle < \langle \Psi_0^2 | \hat{H}^1 | \Psi_0^2 \rangle \quad (2.9)$$

Using $\hat{H}^1 = \hat{H}^2 + (\hat{H}^1 - \hat{H}^2)$ we obtain

$$\begin{aligned} E_1 < \langle \Psi_0^2 | \hat{H}^1 | \Psi_0^2 \rangle &= \langle \Psi_0^2 | \hat{H}^2 | \Psi_0^2 \rangle + \langle \Psi_0^2 | \hat{H}^1 - \hat{H}^2 | \Psi_0^2 \rangle \\ &= E_2 + \langle \Psi_0^2 | V_{en}^1(\mathbf{r}) - V_{en}^2(\mathbf{r}) | \Psi_0^2 \rangle = E_2 + \int \rho(\mathbf{r}) [V_{en}^1(\mathbf{r}) - V_{en}^2(\mathbf{r})] d\mathbf{r} \end{aligned} \quad (2.10)$$

On the other hand, using Ψ_0^1 as a trial wave function on \hat{H}^2 yields

$$\begin{aligned} E_2 &< \langle \Psi_0^1 | \hat{H}^2 | \Psi_0^1 \rangle = \langle \Psi_0^1 | \hat{H}^1 | \Psi_0^1 \rangle + \langle \Psi_0^1 | \hat{H}^2 - \hat{H}^1 | \Psi_0^1 \rangle \\ &= E_1 + \langle \Psi_0^1 | V_{en}^2(\mathbf{r}) - V_{en}^1(\mathbf{r}) | \Psi_0^1 \rangle = E_1 + \int \rho(\mathbf{r}) [V_{en}^2(\mathbf{r}) - V_{en}^1(\mathbf{r})] \mathbf{d}\mathbf{r} \end{aligned} \quad (2.11)$$

Combining the above two relations gives the contradictory inequality $E_1 + E_2 < E_2 + E_1$.

Consequently, the total energy can be expressed as a functional of the density as

$$E(\rho) = T[\rho] + E_{ee}[\rho] + E_{en}[\rho] = F_{HK}[\rho] + \int \rho(\mathbf{r}) V_{en} \mathbf{d}\mathbf{r} \quad (2.12)$$

where $F_{HK}[\rho]$ is independent of the external potential and is thus a universal functional, which means that, if the form of $F_{HK}[\rho]$ were known, it could be used for any many-electron system.

The second Hohnberg-Kohn theorem states that for any many-electron systems a functional $E[\rho]$ exists and that only the true ground state density minimizes this functional. For the proof we assume that \hat{H} is the Hamiltonian generated by the true ground state density ρ and its corresponding external potential V_{en} which gives rise to the ground state Ψ . We already know that any trial density $\tilde{\rho}$ fixes the Hamiltonian \hat{H} with its corresponding ground state wave-function $\tilde{\Psi}$. So, together with the variational principle for the wave-function, we can write

$$\langle \tilde{\Psi} | \hat{H} | \tilde{\Psi} \rangle = F_{HK}[\tilde{\rho}] + \int \tilde{\rho}(\mathbf{r}) V_{en} \mathbf{d}\mathbf{r} = E[\tilde{\rho}] \geq E[\rho] = \langle \Psi | \hat{H} | \Psi \rangle \quad (2.13)$$

2.1.2 Kohn-Sham formalism

In 1965, Kohn and Sham proposed that the interacting many-electrons problem could be transformed into a mean-field problem by a system of N non-interacting electrons moving in an effective field $V_S(\mathbf{r})$, giving the same ground state density as the interacting system [35]. For this reformulation the total energy needs to be written in terms of known quantities. The electron-electron interaction $E_{ee}[\rho]$ can be split up into the classical part $E_H[\rho]$, which is called the Hartree energy, and the unknown non-classical part $E_{\text{noncl}}[\rho]$, which contains the self-interaction correction, exchange and Coulomb correlation terms:

$$E_{ee}(\rho) = \frac{1}{2} \int \int \frac{\rho(\mathbf{r}_1)\rho(\mathbf{r}_2)}{|\mathbf{r}_1 - \mathbf{r}_2|} \mathbf{d}\mathbf{r}_1 \mathbf{d}\mathbf{r}_2 + E_{\text{noncl}}[\rho] = E_H[\rho] + E_{\text{noncl}}[\rho] \quad (2.14)$$

The non-interacting system of electrons can be expressed as a wave-function in the form of a Slater determinant, which is an antisymmetrized product of orthonormal Kohn-Sham spin orbitals $\psi_i(\mathbf{r}, s)$, which give rise to the single-particle kinetic energy $T_S[\rho]$:

$$T_S[\rho] = -\frac{1}{2} \sum_{i,s} \langle \psi_i | \nabla^2 | \psi_i \rangle, \quad \rho(\mathbf{r}) = \sum_{i,s} \psi_i(\mathbf{r}, s)^* \psi_i(\mathbf{r}, s) \quad (2.15)$$

For simplicity we will hereon restrict ourselves to closed shell systems. The Kohn-Sham orbitals satisfy the so-called Kohn-Sham equations

$$\left(-\frac{1}{2}\nabla^2 + V_S(\mathbf{r})\right)\psi_i = \epsilon_i\psi_i \quad (2.16)$$

where the electrons move in the effective field $V_S(\mathbf{r})$, called the Kohn-Sham potential. The total energy can be written in terms of $E_H[\rho]$, $T_S[\rho]$, $V_{en}[\rho]$, and an additional term E_{XC} which contains the correction of $T_S[\rho]$ to $T[\rho]$ together with the non-classical exchange and correlation contribution of the electron-electron interaction to give the exact energy $E[\rho]$:

$$E[\rho] = T_S[\rho] + E_H[\rho] + E_{en}[\rho] + E_{XC}[\rho] \quad (2.17)$$

It can be shown that the effective potential V_S is found by variations of the total energy with respect to the electron density

$$V_S(\mathbf{r}) = V_{en}(\mathbf{r}) + V_H(\mathbf{r}) + V_{XC}(\mathbf{r}) \quad (2.18)$$

where

$$V_H(\mathbf{r}) = \frac{\delta E_H}{\delta \rho(\mathbf{r})} = \int \frac{\rho(\mathbf{r}')}{|\mathbf{r} - \mathbf{r}'|} d\mathbf{r}' \quad (2.19)$$

is the Hartree potential and

$$V_{XC}(\mathbf{r}) = \frac{\delta E_{XC}}{\delta \rho(\mathbf{r})} \quad (2.20)$$

is the exchange-correlation potential.

In practice, the Kohn-Sham equations are solved self-consistently to obtain the ground state density. Starting from an initial wave-function (usually constructed from atomic orbitals) one obtains a charge density which is then used to find the effective potential $V_S[\rho]$. Then, the Kohn-Sham equations are solved to update the Kohn-Sham orbitals, which themselves give rise to a new charge density. This procedure is repeated until self-consistency is achieved.

2.1.3 Functionals

With the above formulation the ground state of a system can in principle be found exactly if one only knew the functional form of the exchange correlation functional E_{XC} . In practice, E_{XC} is replaced by simple approximations. It can be split up into the exchange and correlation part, E_X and E_C .

In the simplest approximation, the local density approximation (LDA) [35], E_{XC} only depends on the local charge density,

$$E_{XC}^{LDA}[\rho] = \int \rho(\mathbf{r})\epsilon_{XC}^{uni}(\rho(\mathbf{r}))d\mathbf{r} \quad (2.21)$$

where $\epsilon_{XC}^{uni}(\rho(\mathbf{r}))$ is the known exchange-correlation energy per particle of a uniform electron gas with the charge density as the one at point \mathbf{r} .

More accurate generalized gradient approximations (GGA) on the other hand also take into account the local gradients of the charge density [36, 37, 38, 39]:

$$E_{XC}^{GGA}[\rho] = \int \rho(\mathbf{r})\epsilon_{XC}(\rho(\mathbf{r}), \nabla\rho(\mathbf{r}))d\mathbf{r} \quad (2.22)$$

By definition LDA is exact for a homogeneous electron gas and gives overall reasonable results for systems with slow variations in the charge density. This is often the case in solids. However, LDA tends to underestimate interatomic bondlengths, especially on surfaces and isolated molecules where the assumption of a homogeneous electron gas is not valid. For such systems GGA give better results. The functional form of GGA are usually chosen such that they coincide with LDA in the limit of a homogeneous electron gas. Other functionals include meta-GGA, which additionally depends on the density of the kinetic energy, and hybrid functionals, which contain a portion of the exact exchange from Hartree-Fock calculations [40]. Hybrid functionals are commonly used in chemistry for molecules and give a considerable improvement on many properties which LDA or GGA fails to predict correctly.

2.1.4 Forces and stresses

Besides the total energy of a configuration, forces on the nuclei and stresses are important properties essential for most applications. Feynman showed in 1939 that atomic forces can be derived only from the electronic charge density. For any parametrization of the Hamiltonian with respect to a variable λ , where $\hat{H}(\lambda)\Psi(\lambda) = E(\lambda)\Psi(\lambda)$, its conjugate force can be written as

$$\begin{aligned} \frac{\partial E}{\partial \lambda} &= \frac{\partial}{\partial \lambda} \langle \Psi | \hat{H} | \Psi \rangle \\ &= \left\langle \Psi \left| \frac{\partial \hat{H}}{\partial \lambda} \right| \Psi \right\rangle + \left\langle \frac{\partial \Psi}{\partial \lambda} \left| \hat{H} \right| \Psi \right\rangle + \left\langle \Psi \left| \hat{H} \right| \frac{\partial \Psi}{\partial \lambda} \right\rangle \\ &= \left\langle \Psi \left| \frac{\partial \hat{H}}{\partial \lambda} \right| \Psi \right\rangle + E \left\langle \frac{\partial \Psi}{\partial \lambda} \left| \Psi \right\rangle + E \left\langle \Psi \left| \frac{\partial \Psi}{\partial \lambda} \right\rangle \right. \\ &= \left\langle \Psi \left| \frac{\partial \hat{H}}{\partial \lambda} \right| \Psi \right\rangle + E \frac{\partial}{\partial \lambda} \langle \Psi | \Psi \rangle \end{aligned} \quad (2.23)$$

The last term vanishes since we obtain for the normalized ground state wave-function $\langle \Psi | \Psi \rangle = 1$, leading to the so-called Hellman-Feynman theorem:

$$\frac{\partial E}{\partial \lambda} = \left\langle \Psi \left| \frac{\partial \hat{H}}{\partial \lambda} \right| \Psi \right\rangle \quad (2.24)$$

Applying the Hellman-Feynman theorem for the many-body Hamiltonian with respect to the atomic coordinates we see that only the electron-nucleus and nucleus-nucleus interaction contribute to the atomic forces. If we set $\lambda = \mathbf{R}_A^\alpha$, which is the cartesian component α of the position of nucleus A , and by inserting equations (2.3) and (2.4) in (2.24), we obtain an expression for the corresponding force component \mathbf{F}_A^α :

$$\mathbf{F}_A^\alpha = -\frac{\partial E}{\partial \mathbf{R}_A^\alpha} = -\int \rho(\mathbf{r}) \frac{\partial V_{en}}{\partial \mathbf{R}_A^\alpha} d\mathbf{r} - \frac{\partial E_{nn}}{\partial \mathbf{R}_A^\alpha} \quad (2.25)$$

The force therefore only depends on the charge density, independent of the (approximate) method from which it was obtained, particularly within DFT.

Besides the microscopic forces acting on atoms in a solid, macroscopic stress and strain describe the state of a condensed matter. The strain is defined as a deformation of a material and is closely related to the quantum mechanical virial theory. At an infinitesimal deformation, any point \mathbf{r} in space is displaced to \mathbf{r}' , which can be described by the second-order strain tensor ϵ :

$$\mathbf{r}' = (\mathbb{I} + \epsilon)\mathbf{r} \quad (2.26)$$

The full many-body wave-function $\Psi(\mathbf{x}_1, \dots, \mathbf{x}_N, \mathbf{R}_1, \dots, \mathbf{R}_M)$ as a function of all particles (electron and nuclei) coordinates is thereby transformed to

$$\Psi_\epsilon(\{\mathbf{q}_i\}) = \det(\mathbb{I} + \epsilon)^{1/2} \Psi(\{[\mathbb{I} + \epsilon]^{-1} \mathbf{q}_i\}) \quad (2.27)$$

where $\mathbf{q}_i = \{\mathbf{r}_k, \mathbf{R}_l\}$ now represent all spatial coordinates of electrons and nuclei.

The pre-factor $\det(\mathbb{I} + \epsilon)^{1/2}$ ensures that the normalization of Ψ is preserved in Ψ_ϵ . The Cauchy stress tensor σ is defined as the negative strain derivatives of the energy per unit volume Ω

$$\sigma_{\alpha\beta} = -\frac{1}{\Omega} \frac{\partial E}{\partial \epsilon_{\alpha\beta}} \quad (2.28)$$

One therefore needs to find the derivatives of the energy expectation value with respect to the strain tensor. In the most general case the energy expectation is given by some Hamiltonian $E_{tot}[\Psi] = \langle \Psi | \hat{H}_{tot} | \Psi \rangle = \langle \Psi | \hat{T} + \hat{V} | \Psi \rangle$, where \hat{T} is the kinetic energy of all particles (electrons and nuclei) and \hat{V} is the total potential energy operator of the system. One can express the stress tensor by inserting equation (2.27), (2.1) and the above formulation of the total energy into (2.28). Nielsen *et al.* [41] showed that

$$\sigma_{\alpha\beta} = -\frac{1}{\Omega} \sum_i \left\langle \Psi \left| \frac{1}{2\mu_i} \nabla_{i\alpha} \nabla_{i\beta} - \frac{1}{2} \sum_{j \neq i} \frac{(\mathbf{q}_j - \mathbf{q}_i)_\alpha (\mathbf{q}_j - \mathbf{q}_i)_\beta}{q_{ij}} \left(\frac{d}{dq_{ij}} \right) \hat{V} \right| \Psi \right\rangle \quad (2.29)$$

where i and j run over all electron and nuclei and $q_{ij} = |\mathbf{q}_j - \mathbf{q}_i|$ is the distance of the particle positions. The particle masses μ_i are given in units of electron masses. For an

isotropic deformation $\epsilon_{\alpha\beta} = \epsilon_0\delta_{\alpha\beta}$ one arrives at the virial theorem by taking the trace of above equation (2.29)

$$3P\Omega = -\text{Tr}(\sigma_{\alpha\beta})\Omega = 2E_{\text{kin}} + E_{\text{pot}} \quad (2.30)$$

which is valid for inter-particle potentials of Coulombic form [42], and where P is the pressure.

In DFT the electron positions are not treated directly, such that in practice each term in the energy expression (2.17) together with the nucleus-nucleus energy E_{nn} must be differentiated separately: the kinetic part of the non-interacting electrons σ_T , the Hartree stress σ_H , electron-nucleus stress σ_{en} , the exchange-correlation stress σ_{XC} and the nucleus-nucleus stress σ_{nn} . The explicit form within LDA was derived in Ref. [41].

2.2 Correlation of search space with PES accuracy: a case study on silicon

Exploring DFT energy landscapes is computationally several orders of magnitude more expensive compared to employing empirical force fields for the same material. A general approach is therefore to use a force field to quickly pre-screen the PES with low accuracy, and then refine the structures of particular interest at the DFT level. In this way the computational cost can be drastically reduced and usually works well for systems for which the atomic interactions can be accurately represented in a classical model. Ionic crystals, in which long-rang electrostatic potentials dominate, are a good example where available force fields provide an excellent representation of the DFT energy landscape. However, other systems are harder to model and are less transferable.

Silicon is a well studied element, and several different, widely employed potentials have been developed and used for large-scale calculations. They have been typically fitted to describe the ground state structures (and/or other known allotropes) and are usually tested to give reasonable values for some physical properties such as bulk moduli or melting temperatures. Other features of the the energy landscape however, such as energy barriers or metastable phases, are less well described. Four different silicon force fields were investigated in a comparative study, namely the Tersoff force field [43] the Stillinger-Weber (SW) force field [44], the environmental dependent interaction potential (EDIP) force field [45, 46, 47], the Lenosky modified embedded-atom method (MEAM) potential [48, 49] and an unpublished reparametrization thereof. They were compared to the more accurate Lenosky tight-binding scheme (LTB) [50] and, whenever possible, to DFT calculations, which were carried out with the BIGDFT wavelet code [51].

2.2.1 Characterizing the potential energy surface of the Si₁₆ cluster by MHM efficiency

One approach to test the accuracy of a force field is to investigate its performance beyond its fitting environment, which in this case are well studied crystalline or amorphous phases of silicon. To investigate the transferability of the different methods, the PES of the Si₁₆ cluster was explored systematically with all of the aforementioned classical many-body potentials, the tight-binding scheme and DFT. The MHM with free boundary conditions [8] (see section 3.3 for details) was used to map out the low-lying part of the energy landscape. The speed with which a system finds its ground state is evidently a physical property of the system and should carry over to most computational geometry-optimization algorithms. The efficiency also depends on the form of the corresponding potential as discussed in the introductory part of this chapter.

Considerable differences were found in the speed of finding the putative ground state configuration with the MHM when using the various potentials to describe the Si₁₆ cluster. Table 2.1 gives the average number \bar{n} of minima visited before finding the putative global minimum. The differences in \bar{n} can be ascribed to the overall shape of the energy landscape. A large \bar{n} indicates a high configurational density of states and a rather glassy energy landscape, whereas a small \bar{n} rather describes a single-funnel system. The Si₁₆ cluster for instance looks more like a structure-seeker with the Lenosky force field and more like a glass-former with the Tersoff force field.

Table 2.1: Average values in 100 MHM runs for each method. \bar{n} is the number of minima visited before finding the putative ground state configuration.

Method	\bar{n}
EDIP	85
Lenosky	10
Reparametrized Lenosky	8
Tersoff	116
Stillinger-Weber	31
Lenosky tight-binding	42
DFT	32

2.2.2 Average curvatures of the PES at local minima

Another topological property of the silicon energy landscape was investigated by studying curvatures of the potential around local minima.

First, we closely examined particular local geometry relaxation pathways. During DFT geometry relaxations of the Si₁₆ one can encounter cases where the cluster is distorted

considerably even though the energy decreases only slightly. Within these flat regions of the PES the norm of the force is small but may increase slightly while the monotonous downhill progress in energy is preserved. Many steps are necessary in the steepest descent DFT geometry relaxation to overcome these flat plateau regions. This behavior is discussed in the following for the DFT relaxation of a local minimum found with the Lenosky potential. Figure 2.2 explicitly shows the variation of the energy with changes in geometry during the relaxation in the various potentials. Only the Lenosky tight-binding scheme provides an accurate energy trend when following the DFT relaxation pathway. All classical potentials fail to even describe the monotonical decrease of the configurational energy along the pathway. With the exception of the Lenosky and the reparametrized Lenosky force fields they give an oscillating energy surface instead of a flat one. This is a first indication that the classical potentials give a too rough PES. Although the SW potential is smoother compared to EDIP and Tersoff it has a very large unphysical excursion in energy at both endpoints which is not the case for any of the other studied potentials. Similar performance of the various force fields was observed by Lenosky and coworkers (see Figure 6 of Ref. [48]). The MEAM ansatz of the Lenosky force field seems to give a smoother PES than the other classical potentials. Furthermore, the average number of interacting atoms were calculated for each potential along the relaxation path, but none of the potentials show a significant fluctuation from the average values. As expected, the number of interacting atoms is largest for the Lenosky tight-binding due to its large cutoff range, followed by both Lenosky and reparametrized Lenosky potentials. EDIP, SW and Tersoff show a similarly low number of interacting neighbors.

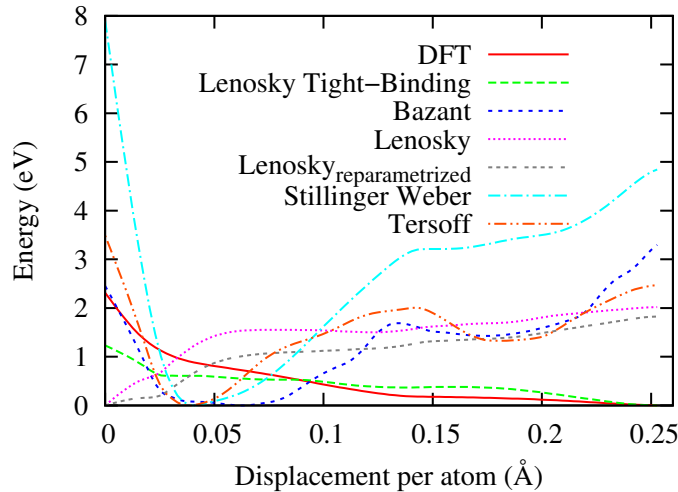


Figure 2.2: Energies of all potentials along a relaxation path in a DFT calculation plotted against the integrated atomic displacement per atom. The starting configuration is a Lenosky force field local minimum. The energies are shifted such that the minimum values are set to 0. For this calculation a tight tolerance, $0.002 \text{ eV}/\text{\AA}$, for the maximum force component on atoms was necessary. $\text{Lenosky}_{\text{reparametrized}}$ is an unpublished reparametrized Lenosky MEAM in which a single FFCD is stable.

Next, the eigenvalues of the Hessian matrix were used as further quantities to describe the differences of the PES among the potentials. Since the smooth topography of the DFT Born-Oppenheimer surface should be a property fairly independent of the cluster size, similar results as above can also be expected for Si_{30} isomers. Therefore, 120 random Si_{30} configurations were relaxed using the different potentials and the largest and smallest eigenvalues of the Hessian matrix were calculated when the local minimum closest to the initial structure was reached. The results are listed in Table 2.2. Two observations indicate that the smoothness of the DFT energy landscape is not reproduced by force fields. First, the classical potentials tend to overestimate the average of the largest eigenvalues (first row in Table 2.2) compared to DFT, indicating a rougher PES with high frequency eigenmodes. The EDIP potential for example has a two times higher average of the largest eigenvalue compared to DFT. Secondly, the eigenvalues of the classical potentials show a higher scatter (second row in Table 2.2), leading to eigenvalues much larger than the average. This is another indication for a rough PES. The Tersoff potential for example overestimates the range of the largest eigenvalues by a factor of 13 compared to DFT. The SW potential provides the most accurate results among the force fields with respect to DFT. This is in agreement with its accurate overall description of low-lying structures. The Lenosky tight-binding scheme gives very accurate values for the second derivative of the energy landscape, almost identical to DFT results.

Table 2.2: Statistical data related to the Hessian matrix around local minima of up to 120 random configurations of a Si_{30} cluster. The corresponding average of the largest and smallest eigenvalues of the Hessian matrices are listed (in $\text{eV}/\text{\AA}^2$). The range of the largest eigenvalues are listed in the second line. The last line contains the average condition number κ of the corresponding Hessian matrices.

	EDIP	Lenosky	SW	Tersoff	LTB	DFT
$\langle E_{large} \rangle$	61.0	43.0	38.0	58.0	23.0	27.0
$E_{large}^{\max} - E_{large}^{\min}$	83.0	65.0	12.0	106.0	7.0	8.0
$\langle E_{small} \rangle$	0.23	0.44	0.31	0.72	0.18	0.2
$\langle \kappa \rangle$	476.0	132.0	175.0	93.0	239.0	197.0

2.2.3 Configurational density of states in bulk silicon

Finally, the MHM was used to explore the low energy region on the PES of bulk silicon. Starting with crystalline cubic diamond structure consisting of 216 Si atoms, 200000 local minima were found successively for each classical potential during the simulation. For the Lenosky tight-binding scheme only 25000 structures could be found due to limited computer time. Periodic boundary conditions were used to provide the appropriate bulk conditions. To speed up the calculation, the simulation cell was fixed to be a cube at the equilibrium volume of the ground state structure. The ten energetically lowest configurations of each potential were then used as input configurations for geometry relaxations in DFT. Table 2.3 summarizes results for the DFT-relaxed geometries.

The correct ground state geometry, the well-known diamond structure, is predicted with all the potentials. However, the structures of the first excited state of different force fields do not coincide. For all potentials, except the Lenosky force field, it is a single four fold coordinate defect [52] (FFCD). The Lenosky potential on the other hand predicts a pair of two four fold coordinated defects in different regions of the cell as the lowest energy defect structure. The double FFCD is 3.99 eV higher in energy compared to the diamond structure.

The majority of the eight other low energy geometries in the EDIP potential are structures containing single displaced atoms which are either four or five fold coordinated. Similar structures can be found with the Tersoff potential. All of these excited configurations are unstable in DFT calculations. The Tersoff potential additionally has minima at a variety of slightly distorted FFCDs which are unstable in DFT.

Table 2.3: The results of ten configurations of each potential relaxed with DFT. The second column shows the number of stable structures. The following columns show the number of structures which relax to the bulk crystal, to a single FFCD or two FFCD which are either neighboring (n-FFCD) or distant (d-FFCD).

Method	Stable	Bulk	FFCD	n-FFCD	d-FFCD
EDIP	2	6	4	0	0
Lenosky	10	1	0	2	7
SW	7	1	4	5	0
Tersoff	2	4	6	0	0
LTB	10	1	1	4	4

In contrast to the other three force fields, the Lenosky force field always predicts pairs of FFCDs as low-lying energy configurations. They are either neighboring and share a common atom or are distant, i.e., located in different regions of the cell. Even though the single FFCD, which must be the first excited state, is not predicted by the Lenosky force field (the reparametrized Lenosky MEAM does stabilize the single FFCD), all other low-lying energy configurations from the second to ninth excited states are stable in DFT geometry optimization. Nonetheless, the sequence with respect to the energy does not coincide with the sequence in DFT energies. The Stillinger-Weber force field behaves very similarly. Only three structures were found to be unstable, the other five excited states all contain two interacting FFCDs.

The best accuracy can be found with the Lenosky tight-binding scheme. All structures exist on the DFT Born-Oppenheimer surface and the energy sequence is correctly described with the exception of the 9th and 10th excited states. They are exchanged in sequence and show an energy difference of 0.02 eV with the Lenosky tight-binding scheme and 0.04 eV when calculated with DFT.

To describe the overall characteristics of the PES the configurational density of states (C-DOS) can be used which gives the number of configurations per energy interval. The

inherent structure approach [53, 54, 55] shows that the C-DOS influences the free energy and hence all thermodynamic quantities. The C-DOS, together with other quantities, was recently used to quantify energy landscapes of solids by Oganov and Valle [56]. The correct C-DOS is reproduced by a force field if the energetic ordering is quantitatively correct and if there is a one-to-one mapping between the local minima of the approximate and exact energy landscape. If either condition is not satisfied it is very unlikely that the C-DOS is correctly reproduced.

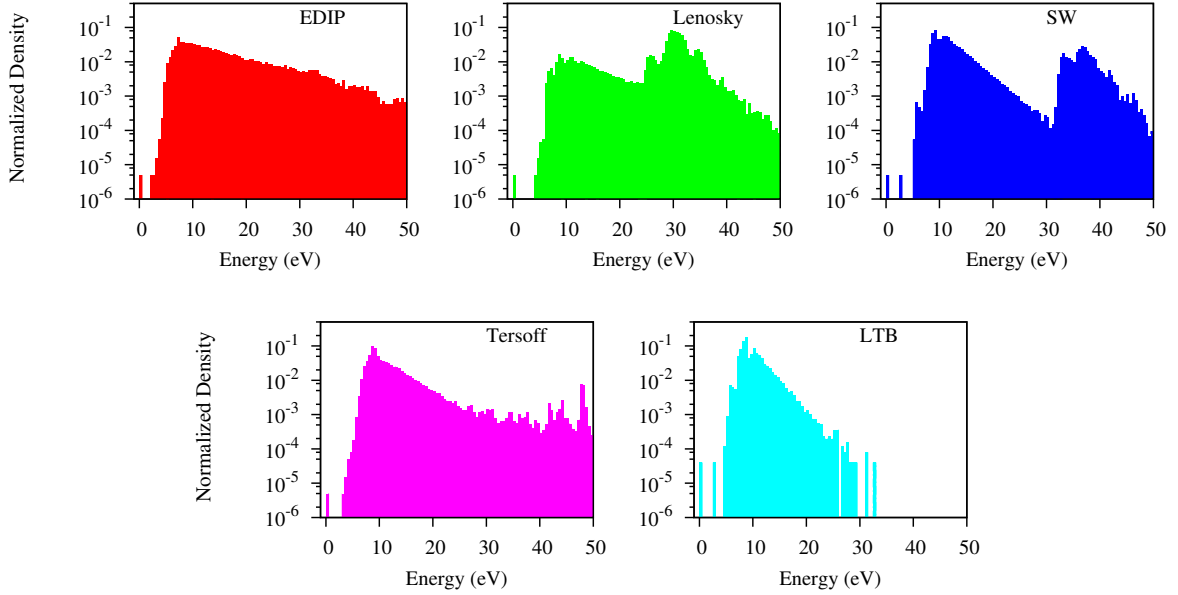


Figure 2.3: The normalized MH-DOS as represented by a histogram consisting of 100 bins on a logarithmic scale. While 200000 values were used for the classical potentials only 25000 could be calculated with the Lenosky tight-binding scheme. The energy is shifted such that the ground state has energy 0.

We approximate this C-DOS by the minima hopping density of states (MH-DOS) which is obtained simply by sampling the low energy region with the MHM and counting the number of distinct minima found in an energy interval. It has to be stressed that a more or less complete sampling of all minima can only be achieved in a very small interval around the putative global minimum. Only in this small interval of several eV we observe in the MH-DOS the expected exponential growth of the number of local minima with respect to the energy of the C-DOS. In our plots we show however a much larger energy interval where the number of states is the true number of states multiplied by the probability that a configuration in this energy range will be visited. Since this probability decreases with increasing energy the MH-DOS tends to zero for large energies in all our plots whereas the C-DOS would be orders of magnitude larger. Since the MHM maps out higher energy configurations when the minima hopping run is allowed to continue longer, we can not only expect a better mapping of the low energy region but also an extended mapping of higher energies with increasing duration of the simulation. The MH-DOS and C-DOS

agree only within the first few bins of the exponential growth region. The lowest energy minima correspond to point defects. The onset of the exponential growth region is due to a growing number of defects (mainly of the FFCD type) which lead continuously to amorphous structures. Some of the potentials also show a second peak at higher energies. This peak is due to amorphous configurations which are related to a sheared crystalline structure. Since we do not relax the simulation cell, sheared structures cannot relax.

The reason why we show the MH-DOS over an energy interval which is much larger than the interval within which we can obtain a reliable C-DOS is the following. If there were good agreement between the C-DOS obtained from different force fields the MH-DOS would also agree. As seen from Figure 2.3 the MH-DOS obtained from different force fields are drastically different and one can therefore conclude that the C-DOS are also drastically different. Stillinger-Weber and the Lenosky tight-binding show similar features in the low energy region, e.g., the energy gap between the single FFCD and higher excited states and the spike between 7 and 8 eV. While the EDIP and Tersoff potential show only a single major peak around 10 eV, both Lenosky and Stillinger-Weber have a second peak located at about 35 eV which corresponds, as discussed above, to sheared structures. This is due to the fact that for these two potentials the C-DOS of unsheared amorphous structures is much lower than for the other potentials and the MHM starts therefore sampling higher energy regions corresponding to sheared structures. The differences in the C-DOS are responsible for the different speeds with which the putative global minimum is found (see Table 2.1).

2.2.4 Summary

In conclusion, the above results show clearly that force fields, which are widely used for dynamical simulations in large silicon systems, not always accurately describe the PES. In addition, they nearly fail in all cases to describe the energy landscape of silicon clusters. With the exception of the MEAM based Lenosky force field, all force fields give rise to PES' that are too rough. In an extended crystalline environment most force fields greatly overestimate the configurational density of states because they give rise to many spurious defect structures which do not exist in more accurate schemes. Non-periodic systems such as clusters present particular problems for classical models, due to the miscoordinated atoms. For structure prediction methods these results imply that a large amount of spurious minima will be found in classical potentials which do not exist at the more accurate DFT level. Therefore, it can be advantageous to directly explore the DFT energy surface instead of using a force field to pre-screen an approximate energy potential landscape containing a large amount of unphysical structures, thus significantly reducing the search space.

STRUCTURE PREDICTION

For a periodic system of N atoms, the number of degrees of freedom is given by $3N$ for the atomic coordinates and additionally 9 degrees of freedom for translational vectors of the crystal defining the periodic cell. Taking into account the translational invariance of the crystal and the rotational invariance of the cell the remaining degrees of freedom define a $3N + 3$ dimensional PES. Possible arrangements of atoms in the cell increases exponentially with system size, such that mapping out all of them is not feasible. Unconstrained structure prediction based solely on the chemical composition is thus considered a NP-hard problem (non-deterministic polynomial-time hard) in computer science.

In crystal structure prediction one is primarily interested in the energetic ordering of dynamically stable local minima on the PES. The stable configuration with lowest energy then corresponds to the ground state structure and is the most likely state at equilibrium. Most structure prediction schemes attack the problem on two levels: (a) relaxations to find local minima on the PES and reduce its dimensionality and (b) global optimization by driving the system towards the ground state. Algorithms for local relaxations are discussed in section 3.1, whereas global optimization schemes are briefly presented in section 3.2. Finally, section 3.3 introduces the MHM and its generalization for crystal structure prediction.

3.1 Local geometry optimization

Essentially all crystal structure prediction methods need to perform local geometry relaxations at some stage of the algorithm, thus the employed relaxation scheme has a significant influence on their efficiency and stability. This section covers such schemes and comparatively evaluates their efficiencies in optimizing crystal lattices.

Finding the local extrema of the energy landscape is equivalent to finding the sets of coordinates for which the gradients with respect to all degrees of freedom vanish. For crystals these are the $3N$ atomic cartesian coordinates \mathbf{r}_i , $i = 1, \dots, N$ and the 3 cell vectors $\mathbf{a}, \mathbf{b}, \mathbf{c}$, which are combined in a matrix $h = \{\mathbf{a}, \mathbf{b}, \mathbf{c}\}$:

$$\frac{\partial E}{\partial \mathbf{r}_i^\gamma} = 0, \quad \frac{\partial E}{\partial h_{\alpha\beta}} = 0 \quad (3.1)$$

where $\gamma \in \{x, y, z\}$.

The Hessian matrix A is given by the second order partial derivatives of the energy with respect to the degrees of freedom:

$$A_{i,j}^{\alpha,\beta} = \frac{\partial^2 E}{\partial \mathbf{x}_i^\alpha \partial \mathbf{x}_j^\beta} \quad (3.2)$$

where Greek characters represent the cartesian components of \mathbf{x} representing every atomic or cell vector i and j . A is symmetric and positive definite at any local energy minimum. Due to translational invariance of the energy within periodic boundary conditions and the rotational invariance of the cell, 6 eigenvalues of the Hessian will vanish. For free boundary conditions the same amount of eigenvalues will vanish, 3 for translational and another 3 for rotational energy invariance of the molecule.

If an external pressure P is applied, the energy E is replaced by the enthalpy given by $H = E + P\Omega$, where Ω is the unit cell volume. Correspondingly, the minima on the enthalpy surface are obtained by

$$\frac{\partial H}{\partial \mathbf{r}_i^\gamma} = \frac{\partial E}{\partial \mathbf{r}_i^\gamma} = 0 \quad (3.3)$$

$$\frac{\partial H}{\partial h_{\alpha\beta}} = \frac{\partial E}{\partial h_{\alpha\beta}} + P \frac{\partial \Omega}{\partial h_{\alpha\beta}} = 0 \quad (3.4)$$

Since the energy is equivalent to the enthalpy in the limit of $P \rightarrow 0$ all discussions below will refer to both quantities simultaneously.

Several methods exist to perform such local relaxations. Starting from an initial state \mathbf{x}_0 , the system is iteratively updated according to an optimization algorithm and driven towards lower energies. A separable function $f(\mathbf{x}) = f(x_1, x_2, \dots, x_n)$ can be minimized by optimizing each variable x_i individually in $f(\tilde{x}_1, \tilde{x}_2, \dots, \tilde{x}_{i-1}, x_i, \tilde{x}_{i+1}, \dots, \tilde{x}_n)$, where the remaining variables $\tilde{x}_1, \tilde{x}_2, \dots, \tilde{x}_{i-1}, \tilde{x}_{i+1}, \dots, \tilde{x}_n$ can be chosen arbitrarily. Consequently one could relax f by performing n individual optimizations in one dimension. The potential energy however is (in general) a non-separable function and must be therefore optimized in all dimensions simultaneously. Therefore, the efficiency of any relaxation method decreases with increasing number of degrees of freedom. The condition number $\kappa = \frac{d_{\max}}{d_{\min}}$, where d_{\max} and d_{\min} are the largest and smallest eigenvalues of the Hessian,

respectively, determines the speed of convergence: the larger the conditioning number κ , the more iterations are needed to relax the structure, and κ typically increases strongly with system size. The steepest descent algorithm for example converges proportionally to κ , whereas more sophisticated schemes behave proportionally to $\sqrt{\kappa}$. Furthermore, for crystal structures the degrees of freedom are additionally coupled, since the atomic coordinates change whenever the cell variables are modified. This poses further challenges in structure optimization. Employing reduced coordinates can somewhat circumvent this problem, but will in general lead to worse condition numbers.

3.1.1 Steepest descent

The most simple optimization scheme is the steepest descent method. Although not very efficient, it is the most stable method available. A function $f(\mathbf{x})$ is minimized by taking small steps along the negative gradient given at the current coordinate \mathbf{x}_t . An initial approximate solution \mathbf{x}_0 is guessed, and the following scheme is then used to iteratively converge towards a close-by minimum:

$$\mathbf{x}_{t+1} = \mathbf{x}_t - \alpha_t \nabla f(\mathbf{x}_t) \quad (3.5)$$

The scalar step size α_t should be small enough to guarantee a monotonic decrease of $f(\mathbf{x}_t)$ in every step t . However, a too small value will result in a very slow convergence. Therefore, a feedback on α_t can be employed. Whenever a step $t + 1$ leads to an increase in $f(\mathbf{x}_{t+1})$ compared to the previous value $f(\mathbf{x}_t)$, the step size α_{t+1} should be decreased (for example by a factor of $1/2$), and in all other cases α_{t+1} can be slightly increased (for example by 5%). The big advantage of the steepest descent method is that convergence is guaranteed to occur if the function under consideration is continuous and the step-size is sufficiently small. In Figure 3.1 a simple model of a 2D energy function is plotted together with the steepest descent directions of 3 initial guesses.

Two major problems arise when employing steepest descent minimization on crystal structures. First, the forces on the atomic coordinates are given in units of $\frac{\text{energy}}{\text{length}}$, whereas stresses are usually given in a pressure unit, which is equivalent to $\frac{\text{energy}}{\text{volume}}$. Furthermore, several choices are available for the steepest descent direction of the cell variables which have been proposed in literature. The 3×3 Cauchy stress tensor σ is defined as the negative volume-normalized strain derivatives of the energy $\sigma_{\alpha\beta} = -\frac{1}{\Omega} \frac{\partial E}{\partial \epsilon_{\alpha\beta}}$. Most implementations use the quantity $\sigma_{\text{SD1}} = -(\sigma + P\mathbb{I})$ as the steepest descent direction. However, a more appropriate choice would be to employ the “true” stress tensor, which is the energy derivative with respect to the cell parameters $f_{\alpha\beta}^h = \frac{\partial E}{\partial h_{\alpha\beta}}$, which can be used to express the enthalpy gradient as $\frac{\partial H}{\partial h_{\alpha\beta}} = f_{\alpha\beta}^h + P \frac{\partial \Omega}{\partial h_{\alpha\beta}}$. With $\Omega = \det(h)$ and the Jacobi’s formula $\frac{\partial \det(h)}{\partial h_{\alpha\beta}} = \det(h) h_{\beta\alpha}^{-1} = \Omega h_{\beta\alpha}^{-1}$ we obtain the “true” steepest descent direction $\sigma_{\text{SD2}} = -(f^h + P\mathbb{I}\Omega(h^{-1})^T) = -\Omega(\sigma + P\mathbb{I})(h^{-1})^T$. Yet another definition was recently

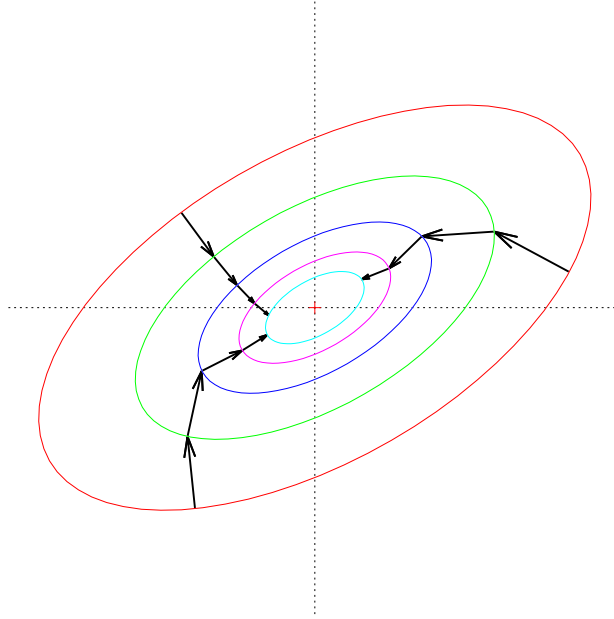


Figure 3.1: Several steepest descent directions on a 2D energy landscape

proposed by Sheppard *et al.* [57]. To obtain a steepest-descent direction which is invariant to the choice of the cell they use $\sigma_{\text{SD3}} = -h(\sigma + P\mathbb{I})$. Obviously, all three definitions equivalently minimize the stress, however the efficiency is expected to vary.

Second, the atomic coordinates and cell variables depend on each other. Therefore, the atomic and cell variables cannot be updated simultaneously. One can thus operate on the reduced atomic coordinates $\mathbf{s}_i = h^{-1}\mathbf{r}_i$, which are independent of the cell vectors, or employ the following procedure to simultaneously update the atomic and cell variables. At every steepest descent iteration, first move the atomic coordinates \mathbf{r}_i along the negative energy gradient to obtain $\mathbf{r}'_i = \mathbf{r}_i - \alpha_{\text{at}} \frac{\partial H}{\partial \mathbf{r}_i}$. Then, the cell h is modified to $h' = h - \alpha_{\text{lat}} \frac{\partial H}{\partial h}$. To preserve the fractional coordinates \mathbf{s}_i , a transformation matrix $b = h'h^{-1}$ is used to finally rescale all atomic coordinates to $\mathbf{r}''_i = b\mathbf{r}'_i$, which are then used in the following iteration.

3.1.2 BFGS

The Newton algorithm is an iterative scheme where the Hessian matrix A is used to determine the step-size and descent direction instead of using a constant scalar α as in the steepest descent method. This approach converges within one single step for any initial configuration \mathbf{x}_t if the potential is harmonic.

The Newton method is derived from a local Taylor expansion of $f(\mathbf{x})$ around \mathbf{x}_t to the

second order

$$f(\mathbf{x}) \approx f(\mathbf{x}_t) + (\mathbf{x} - \mathbf{x}_t)\nabla f(\mathbf{x}_t) + \frac{1}{2}(\mathbf{x} - \mathbf{x}_t)^T A(\mathbf{x} - \mathbf{x}_t) \quad (3.6)$$

One requires that

$$\nabla f(\mathbf{x}) = \nabla f(\mathbf{x}_t) + A(\mathbf{x} - \mathbf{x}_t) \quad (3.7)$$

vanishes, which leads to the Newton iteration

$$\mathbf{x} = \mathbf{x}_t - A^{-1}\nabla f(\mathbf{x}_t) \quad (3.8)$$

However, determining A is computationally extremely expensive (especially if its analytical form is not known) and requires many energy and/or force evaluations when obtained numerically. Furthermore, if the initial guess is not close to the minimum, a full Newton step can be too large and overshoot the minimum. Therefore, a line search is usually performed along the Newton direction.

The Broyden-Fletcher-Goldfarb-Shanno (BFGS) method [58, 59] is a quasi-Newton algorithm which employs an approximate Hessian, which is gradually improved as the minimization progresses. The sequence of approximated inverse Hessian matrices C_t should therefore converge towards the true inverse Hessian A^{-1} at the minimum. Importantly, since the true Hessian at the minimum must be symmetric and positive definite, the update mechanism should ensure that the approximate Hessian also preserve these properties. If we substitute \mathbf{x} in (3.7) with \mathbf{x}_{t+1} we obtain the following relation

$$\mathbf{x}_{t+1} - \mathbf{x}_t = A^{-1}(\nabla f(\mathbf{x}_{t+1}) - \nabla f(\mathbf{x}_t)) \quad (3.9)$$

which must be satisfied by the approximate inverse Hessian $C_{t+1} = A^{-1}$. Furthermore, the update mechanism of the approximate Hessian should satisfy $C_{t+1} = C_t + \Delta_t$, where Δ_t corresponds to a small correction. It can be shown that the following scheme fulfills above constraints and gives rise to the BFGS formalism:

$$C_{t+1} = C_t + \left(\mathbb{I} + \frac{\delta \mathbf{g}_t^T C_t \delta \mathbf{g}_t}{\delta \mathbf{g}_t^T \delta \mathbf{x}_t} \right) \frac{\delta \mathbf{x}_t \delta \mathbf{x}_t^T}{\delta \mathbf{x}_t^T \delta \mathbf{g}_t} - \frac{C_t \delta \mathbf{g}_t \delta \mathbf{x}_t^T + (C_t \delta \mathbf{g}_t \delta \mathbf{x}_t^T)^T}{\delta \mathbf{g}_t^T \delta \mathbf{x}_t} \quad (3.10)$$

where $\delta \mathbf{x}_t = \mathbf{x}_{t+1} - \mathbf{x}_t$ and $\delta \mathbf{g}_t = \nabla f(\mathbf{x}_{t+1}) - \nabla f(\mathbf{x}_t)$.

The BFGS algorithm reads:

- compute the search direction $\mathbf{d}_t = -C_t \nabla f(\mathbf{x}_t)$
- perform a line search to obtain α which minimizes $f(\mathbf{x}_t + \alpha \mathbf{d}_t)$
- set $\mathbf{x}_{t+1} = \mathbf{x}_t + \alpha \mathbf{d}_t$
- check for convergence of $\nabla f(\mathbf{x}_{t+1})$

- compute $\delta\mathbf{x}_t = \alpha\mathbf{d}_t$ and $\delta\mathbf{g}_t = \nabla f(\mathbf{x}_{t+1}) - \nabla f(\mathbf{x}_t)$
- update $C_t \rightarrow C_{t+1}$ according to equation (3.10) and cycle

In the first iteration C_0 can be initialized as the unit matrix \mathbb{I} .

For optimizing the energy with respect to the the crystal structure, the $3N$ reduced atomic coordinates \mathbf{s}_i , $i = 1, \dots, N$ of the N atoms and the cell vectors h are combined to a vector $\mathbf{X} = \{\mathbf{s}_1, \mathbf{s}_1, \dots, \mathbf{s}_N, h\}$. The line search can be carried out by the following approximative method: from the current coordinates \mathbf{X}_t , at which the gradient is $\mathbf{k}_t = \nabla H(\mathbf{X}_t)$, a reasonable α'_t (for example $\alpha'_t = 1$) is used to perform a trial step along $\mathbf{d}_t = -C_t \nabla H(\mathbf{X}_t)$, where the gradient $\mathbf{k}'_t = \nabla H(\mathbf{X}_t + \alpha'_t \mathbf{d}_t)$ is evaluated. Projections of \mathbf{k}_t and \mathbf{k}'_t onto the subspace of \mathbf{d}_t are then used to obtain a linear interpolation, which has to vanish at the correct step-size α_t .

Although the BFGS method is very efficient, it was found to be somewhat unstable under certain conditions. Especially the line search was found to be very sensitive to discontinuities in the energies or forces, as they might arise in DFT calculations.

3.1.3 FIRE

FIRE is the abbreviation for the fast inertia relaxation engine [60] which belongs to the class of optimization schemes based on damped dynamics [61]. In such schemes the Newtonian equation of motion is iteratively integrated, however including a damping factor to reduce the velocity along the trajectory as the potential energy decreases. In this way the system will eventually relax to a close-by local minimum. A careful tuning of parameters such as the time steps and damping factor is required to obtain a good efficiency: over-damping will result in slow convergence, and under-damping will lead to oscillations in the coordinates, and in the worst case also in the energies. However, damped molecular dynamics are generally faster than steepest descent while similarly stable and are therefore widely used for structural optimization.

The FIRE algorithm to optimize the energy E of N atoms in a molecule is described by the following equation of motion for a particle i :

$$\dot{\mathbf{v}}_i(t) = \frac{\mathbf{F}_i}{m_i} - \gamma(t)|\mathbf{v}_i(t)|(\hat{\mathbf{v}}_i(t) - \hat{\mathbf{F}}_i(t)) \quad (3.11)$$

where $\mathbf{v}_i(t) = \dot{\mathbf{x}}_i(t)$ are the velocities, $\mathbf{F}_i = -(\nabla E)_i$ are the forces and m_i are the atomic masses. Unit vectors are denoted with a hat. The second term in equation (3.11) introduces an acceleration towards the gradient direction, which is controlled by the scalar factor $\gamma(t)$. Uphill motions are prohibited by a simple feedback mechanism on the power $P = \mathbf{F} \cdot \mathbf{v}$, such that the velocities are reset to 0 as soon as P becomes negative.

To apply the FIRE method for optimizing crystal structures one can start from any variable cell shape molecular dynamics method, such as the Parrinello-Rahman method [62] (see section 3.3.3 for details). However, the velocities for updating the N reduced atomic coordinates \mathbf{s}_i , $i \in 1, \dots, N$ and cell variables h are modified in every molecular dynamics step. Again, let \mathbf{X} be the combined vector of reduced atomic and cell variables, and \mathbf{V} its velocity. Then:

- if the first step: initialize parameters and variables: $\Delta t = \Delta t_0$, $\alpha = \alpha_{\text{start}}$, and the velocities $\mathbf{V} = 0$
- use molecular dynamics to obtain the reduced atomic coordinates and cell vectors \mathbf{X} , and the corresponding generalized forces \mathbf{F} . Stop if the atomic forces and stresses are converged
- compute the power $P = \mathbf{F} \cdot \mathbf{V}$, which tells us if the trajectory at the current point is along a downhill ($P > 0$) or uphill ($P < 0$) direction
- modify the velocities according to $\mathbf{V} \rightarrow (1 - \alpha)\mathbf{V} + \alpha\hat{\mathbf{F}}|\mathbf{V}|$
- if $P > 0$ in at least N_{min} consecutive steps, then the time-step Δt is increased $\Delta t \rightarrow \min(\Delta t f_{\text{inc}}, \Delta t_{\text{max}})$, where $f_{\text{inc}} > 1$, and the mixing factor α is decreased $\alpha \rightarrow \alpha f_{\alpha}$, where $f_{\alpha} < 1$. It is important not to accelerate the dynamics initially (for the first N_{min} steps) to get a stable relaxation
- if $P \leq 0$, then $\Delta t \rightarrow \Delta t f_{\text{dec}}$, where $f_{\text{dec}} < 1$, and $\mathbf{V} \rightarrow 0$ and $\alpha \rightarrow \alpha_{\text{start}}$, leading to a restart with zero velocities
- return to MD and cycle

The original parameters suggested by Bitzek *et al.* turned out to result in a fast convergence, and are given by $N_{\text{min}} = 5$, $f_{\text{inc}} = 1.1$, $f_{\text{dec}} = 0.5$, $\alpha_{\text{start}} = 0.3$, $f_{\alpha} = 0.99$, and Δt_{max} should be roughly one order of magnitude larger than the usual molecular dynamics time-step. Still, a careful tuning of the atomic masses and the fictitious cell mass is required. FIRE represents a good compromise between efficiency and stability. Since the velocities contain information on previous iteration and carry a momentum, small discontinuities in the energies or forces as they might arise from DFT calculations don't affect the stability. However, in most cases FIRE is inferior to BFGS in terms of efficiency.

3.1.4 Comparison of geometry optimization methods

A comparative test was carried out on the efficiency of the various geometry optimization methods discussed above. A binary Lennard-Jones mixture was used as a model system, where energies and forces were evaluated in a truncated functional form (provided in

equation (4.1)) with the following parameters: $\sigma_{AA} = 1.50$, $\sigma_{AB} = 2.25$, $\sigma_{BB} = 3.00$ and $\epsilon_{AA} = 1.00$, $\epsilon_{AB} = 1.25$, $\epsilon_{BB} = 1.00$, and a cutoff radius of $r_{\alpha\beta}^{cut} = 2.5\sigma_{\alpha\beta}$. A mixture with 16 type A and 8 type B components was used to relax 300 random structures at 0 GPa. The BFGS and FIRE method were implemented as discussed above, and three different flavors of steepest descent were used:

- SD1** Two independent step-sizes for the atomic coordinates α_{at} and the lattice parameters α_{lat} were used and initially optimized to give a good efficiency. An energy feedback was employed on the atomic degrees of freedom, since its dimensionality is much higher compared to the cell degrees of freedom. The Cauchy stress $\sigma_{SD1} = -(\sigma + P\mathbb{I})$ was used for the steepest descent directions of the cell.
- SD2** Same as SD1, however using the stress $\sigma_{SD2} = -\Omega(\sigma + P\mathbb{I})(h^{-1})^T$ as the steepest descent direction for the cell.
- SD3** Same as SD1, however using the stress $\sigma_{SD3} = -h(\sigma + P\mathbb{I})$ as the steepest descent direction for the cell.
- SD4** Same as SD3, together with the following Jacobian J according to Ref. [57] to fix the coupling between atomic and cell forces: $J = \Omega^{1/3}N^{1/6}$. This leads to the collective steepest descent direction $\mathbf{F} = \left(\frac{\partial H}{\partial \mathbf{r}_1}, \dots, \frac{\partial H}{\partial \mathbf{r}_N}, \frac{\sigma_{SD3}}{J}\right)$. An energy feedback was employed for the combined step-size $\alpha_{at,lat}$

The results are presented in table 3.1. Clearly, all steepest descent approaches are significantly less efficient compared to FIRE or BFGS. The best results among the steepest descent methods were obtained by following the direction given by σ_{SD3} with a variable step-size for the atomic degrees of freedom. The same approach, but using the Jacobian suggested by Sheppard *et al.*, resulted in a decrease in efficiency. The most efficient algorithm is the BFGS method, roughly 30% faster than FIRE. However, it becomes unstable

Table 3.1: Different local relaxation algorithms are compared with respect to their efficiencies. 300 structure relaxations were performed with each approach, and the mean number of force evaluations \bar{N} to reach a specific (very tight) convergence criterion are listed, together with their standard deviations σ_N (not to be confused with the stress tensor).

Algorithm	\bar{N}	σ_N
SD1	1058	648
SD2	1016	712
SD3	614	594
SD4	1005	680
FIRE	204	63
BFGS	158	32

when used together with *ab initio* methods, where the energies and forces as a function of the atomic and cell parameters may be discontinuous and is therefore not practicable. In conclusion, the FIRE method turned out to give a good compromise between efficiency and reliability.

3.2 Global structural optimization methods

In the previous section we discussed various methods to find *local* minima on the potential energy landscape. The task of *global* optimization methods is then to find the lowest among all local minima. Unfortunately, the number of such local minima on the high dimensional PES increases exponentially with system size, which makes it impossible to identify the global minimum even for moderately sized systems with simple exhaustive search methods. Limited computational time restricts all global optimization algorithms to perform a search on a (small) fraction of the total number of local minima based on assumptions on the characteristics of the PES. The lowest energy structure throughout the search is then determined as the putative ground state, however there is no way to prove that it truly represents the global minimum.

Overall, global optimization methods can be divided into two main groups and are either based on thermodynamics or rely on non-thermodynamic approaches. Simulated annealing, metadynamics and basin hopping are based on thermodynamical principles, whereas genetic algorithm and particle swarm optimization belong to the class of evolutionary methods. Random search, database searching and data mining schemes rely primarily on chemical intuition and structure-chemistry correlation models.

Algorithms based on thermodynamics are guaranteed to arrive at the ground state structure in thermodynamic equilibrium. However, since crossing high barriers connecting two funnels is a rare event due to the presence of the Boltzmann factor and the given computational time is limited, thermodynamic equilibrium will essentially never be reached and such methods are therefore not always successful. Although there exist several approaches to circumvent this problem, the choice of the initial configuration highly influences the success rate and efficiency of such simulations. The success of non-thermodynamic methods is based on educated assumptions on the energy landscape. The validity of such assumptions may vary strongly depending on the material under investigation. Nevertheless, non-thermodynamic methods have been found to be very efficient in a wide range of structure prediction applications. The most common global optimization methods are briefly described in the following sections.

3.2.1 Database searching and data mining

The most simple, but frequently applied approach in crystal structure prediction is based on exploiting informations available on known materials. Educated guesses of the structure in a novel compound are made from knowledge of structures from previous experiments of similar materials. Chemically similar compounds tend to exhibit similar crystal structures. Simply examining neighboring elements in the periodic tables can hint towards the ground state structure. Other physical properties like similar electronegativity, atomic radii, number of valence electrons, valence electron energy or electron configuration have been used to characterize structural similarities. Goldschmidt's rules of substitution [63] describes for example simple recipes to exchange atomic species in ionic crystals, and the phenomenological Pettifor chemical scale χ can be used to generate two dimensional structure maps of binary compounds [64, 65], which show clear structural separations within the whole periodic table.

Data mining [66] has been used to analyze large datasets and, based on the information retrieved, to extrapolate and predict properties of elements not contained in the database. Since usually a large database is analyzed, an automatic and machine-based extraction of the essential properties is essential. In data mining crystal structure prediction methods (online-) databases of known compounds can be used to extract such informations. Hofmann *et al.* [67] used the crystallographic Cambridge Structure Database [68] to derive an energy function with predictive power, avoiding the use of any expensive *ab initio* calculations. The following data mining approach was employed: in an initial screening process the database is analyzed to remove poor quality data, which is done by identifying structures containing atypical intermolecular distances, incomplete symmetry descriptions and insufficient accuracy of the structural resolution from XRD measurements. Next, descriptors are defined to represent a crystal structure. Intermolecular contact descriptors are used to generate a structure vector, which is based on inter-atomic distances, bond types and atom types present in the structure. Then, decoy structures are generated for every structure in the database by slightly and randomly distorting the experimental structures to generate the fitting database for the final energy potential. Finally, a model potential as a function of the descriptors is trained such that it can correctly order the real and the decoy structures. The resulting inter-atomic pair potential can then be used to predict crystal structures of unknown alloys.

Ceder *et al.* have developed several approaches based on data mining combined with *ab initio* calculations to predict the ground state structures of novel alloys [4, 5, 6, 7]. One such approach is the data mining of quantum calculations (DMQC), where a set of library structures from experimental observations are used as a basis for quantum mechanical predictions of crystal structures in binary compounds. It was shown that the energy differences in different structures strongly correlate between alloys with different chemistry. For this purpose, the energy vectors \mathbf{E}_i for each alloy i in the database were obtained from first principles calculations, where the components correspond to one of

the $n = \dim(\mathbf{E}_i)$ possible crystal structures. A principal component analysis was carried out to demonstrate that the dimensionality d of the structural energies can be reduced to a value much smaller than n . Therefore, a prediction of the ground state structure of an unknown alloy can be made without scanning the whole structural variety. Starting from only a few explicitly evaluated structural *ab initio* energies of the constituent elements, the convex hull of the composition for a new alloy is predicted. Then, the *ab initio* energy of the most promising candidate is evaluated and included in the database. By iterating the above process and thus gradually feeding new information into the database the ground state structures can be found efficiently.

Similarly, the Data Mining Structure Predictor (DMSP) scheme [7] uses structural databases to map out the most probable ground state structures for a new alloy at different compositions. The idea is that there exist a strong structure-structure correlation among different compositions in alloys due to underlying physical properties. Therefore, it is possible to obtain a probability distribution of crystal structures of an unknown composition given already known crystal structures at other compositions of the alloy.

The methods discussed above are powerful in the sense that the search space of the available crystal structures does not have to be explored exhaustively, thus significantly reducing the computational cost. Data mining is particularly powerful and is thus often employed in materials design [69, 70, 71]. However, they are limited for crystal structure prediction by the fact that only structures in the underlying database are available. Applicability to high-pressure or high-temperature phases for example are difficult due to limited available data from theory and experiments. Furthermore, some compounds may unexpectedly adopt a ground state structure related to a completely different material, which poses a formidable challenge for such methods. In fact, predictions of completely new and unknown crystal structures is simply impossible.

3.2.2 Simulated annealing

The approach in simulated annealing [72, 73, 74, 75, 76, 77, 78] is based on the procedure applied in experimental physics to reduce defects and obtain larger single crystals. A sample is heated to high temperatures and then slowly cooled down. Through the heating, the average kinetic energy of the atoms is increased, thus allowing them to diffuse easily. The system can cross over high energy barriers towards preferably lower energy structures. The controlled cooling process allows the atoms to rearrange and recrystallize in its ground state structure.

Simulated annealing is a thermodynamic approach to global optimization and mimics this process. Starting from an initial configuration, the atoms are usually equilibrated at a high constant temperature through molecular dynamics or with a Monte Carlo method where periodic local quenching is performed. Then, by gradually reducing the temperature, the system moves towards lower energy structures. According to the Boltzmann

distribution, the system finally crystallizes at the ground state if thermodynamic equilibrium is preserved throughout the cooling process. However, in practice this method is only applicable for simple energy landscapes, since the system gets easily trapped in a local minimum or a wrong funnel, especially if they are surrounded by high energy barriers.

As with all methods employing walkers to explore the PES, the efficiency of the simulated annealing method strongly depends on the moves performed to propagate the system. In basic simulated annealing, molecular dynamics or random displacements are used for atoms or atom groups and the cell variables. However, many other move classes have been proposed and can be used depending on the system under investigation, such as atom mutations or exchanges of complete atom groups. Furthermore, the efficiency can be improved by employing different temperature schedules. Most commonly, the temperature is reduced linearly or exponentially with increasing number of time steps [79]. Other temperature schedules include temperature cycling [80, 81], where the temperature periodically oscillates in a given range, or adaptive schedules [82, 83], for example by using a feedback mechanism on the acceptance/rejection ratio to adjust the temperature. Furthermore, different variations have also been introduced for the acceptance criterion. Besides the most common Metropolis distribution, the Tsallis distribution [84, 85] and simple thresholding have been proposed [86].

3.2.3 Metadynamics

Variable cell shape molecular dynamics was proposed by Parrinello and Rahman in 1980 [62] and has been widely applied to investigate solids. However, structural transitions in crystals are rare events in variable cell constant pressure molecular dynamics simulations since they are generally associated with crossing (possibly very high) energy barriers. To overcome this timescale gap issue, metadynamics [87, 88, 89, 90, 91] was designed to model phase transition processes in an accelerated manner. The main idea of this approach is to split the set of variables into two groups: a fast and a slow group. The fast variables are those which can be equilibrated in a reasonable simulation time, whereas the slow ones can require exceeding computational costs. While the fast variables are sampled by classical molecular dynamics, a small number of collective variables are defined for the slow ones and treated with metadynamics.

Since lattice vibrations often correspond to low frequency modes, the cell parameters are usually used as collective variables in crystalline systems. In the configurational space of these collective variables, Gaussian functions are added to the portion of the energy landscape being currently explored to generate a bias potential. In this way, the current energy well is gradually filled which facilitates the crossing of the surrounding barriers. Between every metadynamics step, the averaged stress tensor is evaluated employing a NVT molecular dynamics simulation during which the fast variables are allowed to

equilibrate. Finally, the system will be driven out of the well towards unexplored regions of the PES by preferably crossing over the lowest barrier. Thus, the complete potential energy landscape of the collective variables will be eventually explored and filled with Gaussians.

The choice of the width and amplitude of the Gaussians is essential to tune the accuracy and computational cost of metadynamics simulations. Filling energy wells too quickly with large Gaussians may lead to wrong phase transitions, or completely undermine specific structures. However, choosing too small Gaussians will require a large amount of expensive metadynamics steps. Furthermore, metadynamics simulations require relatively large simulation cells in order to correctly describe nucleation processes during phase transitions.

3.2.4 Basin hopping

The basin hopping method [92, 93, 94, 30] is a thermodynamical method. However, a modified PES is sampled which is transformed into a stepwise constant staircase function representing the energies of the local minima of the corresponding basins of attraction, $E(\mathbf{X}) \rightarrow \bar{E}(\mathbf{X}) = \min\{E(\mathbf{X})\}$, where \mathbf{X} is the combined set of atomic coordinates and cell vectors. A Monte Carlo sampling at constant temperature of this modified PES is then performed, on which the transition barriers between the minima have now been eliminated such that the system can move between the minima much easier compared to the standard Monte Carlo methods.

Usually, the system is moved starting from a local minimum with energy E_{init} by performing random displacements of the coordinates from a uniform distribution in the range of $\max_d[-1, 1]$, where \max_d represents the maximal stepsize. A local geometry relaxation is then performed to a local minimum with energy E_{trial} . In the Metropolis step the trial structure is always accepted if $E_{\text{trial}} < E_{\text{init}}$, and only if a random number drawn from a uniform distribution in $[0, 1]$ is less than the Boltzmann factor $\exp\left(\frac{E_{\text{init}} - E_{\text{trial}}}{k_B T}\right)$. If accepted, the current configuration and energy is updated, else a new trial step is performed from the previous configuration. To ensure that the system will not get stuck in a local minimum the step-size \max_d is dynamically adjusted such that half of the new configurations are accepted in the Metropolis step.

The basin hopping method is closely related to the ‘‘Monte Carlo plus energy minimization’’ procedure of Li *et al.* [95]. Within this method, the configuration is always reset after an unsuccessful trial step, which is not necessarily the case for basin hopping. Furthermore, other moves on the PES have been proposed in literature. Basin hopping can also be used within a simulated annealing scheme if the simulation is performed with gradually decreasing temperature.

3.2.5 Genetic algorithm

Genetic algorithms [96, 97, 98, 99, 100, 101, 102, 103, 104, 105, 106, 107, 108, 109] are a class of evolutionary algorithms and are inspired by Darwin’s natural evolutionary theory, where in a population the “fittest” individuals are most likely to survive. Genetic algorithms have been successfully used for a wide range of global optimization problems. Solutions to an optimization problem are usually encoded in binary form, representing the genome of an individual. Initially, a set of individuals is randomly spawned to populate a first generation of solutions, and each individual is evaluated according to its fitness. By variation operations such as random mutation or elimination of an individual, or by recombination of two individuals based in their fitness, a new generation of solutions is created. By iterating this algorithm the overall fitness of each generation is improved, thus leading towards the optimal solution of the problem.

When employing genetic algorithms within structure prediction, the fitness of the individual solutions is usually given by the (free) energy or enthalpy of the structures. However, structures can be also optimized with respect to other quantities, such as hardness of a material [110]. It is more problematic to find an appropriate genetic representation for the structures and useful variation schemes. Binary representations are not well suited, since physically meaningless structures can be obtained during a mating or mutation process. First approaches in adopting genetic algorithms for structure predictions were reported in 1995 [100, 98] with rather limited success rates. Further progress on genetic algorithms in crystal structure prediction have been made there-since by adopting improved representation schemes. Implementations of such methods are available in software packages like GASP [111] or USPEX [107]. The evolutionary algorithm USPEX (Universal Structure Predictor: Evolutionary Xtallography), developed by A.Oganov in 2006, is one of the most successful methods within crystal structure prediction and will be discussed in detail below.

In USPEX, structures are represented by real numbers to describe the lattice and atomic coordinates. Local geometry optimizations are employed on all structures within all generations to reduce the dimensionality of the search space. Initially, a population of candidate structures is generated randomly, taking into account physical properties such as atomic radii and cell volumes to give reasonable input guesses. For larger systems, initial structures are generated from sub-units containing predefined molecules or based on chemical intuition and bonding properties to improve the overall fitness of the initial population. After performing local geometry optimizations on all structures, identical structures are eliminated. Then, parent structures are selected based on the energy ranking within the current generation, which are then used to obtain the individuals (children) in the next generation. The following variation operations are used:

Heredity Planar slabs from two (or more) parent structures are used to spawn a child.

For large systems, a fingerprint function [112, 56] can be used to select similar parents in order to produce offsprings with improved fitness.

Lattice mutation A single parent structure is deformed by shearing the lattice vectors.

Permutation Atoms of different species are exchanged within a single parent structure.

Special coordinate mutations Displacements of atoms of a single parent structure based on chemical intuition (preserving molecular subunits and their orientations) and on local order. The concept of local order [113] states that structures with high order (and thus higher symmetry) are overall energetically favorable. The local order evaluates the quasi-stability of a specific atomic position by evaluating the symmetry of its near environment. Atoms with a high local order (i.e. within a highly symmetric environment) are less probably mutated to retain favorable structural motifs, while atoms with low local order are generally close to crystal defects and thus more violently displaced.

Above variation operations are constrained by avoiding unphysical structures, such as extremely small bond-lengths or unit cell volumes. The so obtained structures in the new generation are then locally relaxed. It can be expected that the new generation contains structures with an overall improved fitness compared to the previous generation. Child structures with low fitness are eliminated from a generation to further increase the average fitness of following generations. However, instead of monotonically converging towards the fitter generations by preserving previously generated good solutions, a diverse gene pool must be preserved by directly transferring some of the candidate structure of previous generations, or by generating new random structures. Keeping a high diversity is important for a thorough search, since it is equivalent to scanning a wide range of the energy landscape spanning over multiple funnels.

In contrast to methods based on thermodynamics, which in principle guarantee that the ground state can be found (eventually), no prediction regarding the success rate of genetic algorithms can be made. Usually, genetic algorithms are iterated until the fitness of the consecutive generations is saturated or achieves a predefined target value. Schönborn *et al.* [114] have shown that genetic algorithms can even fail for very complex energy landscapes of molecules. Furthermore, the variation operations need to be carefully tuned to avoid highly unphysical child structures. Nevertheless, USPEX has been successfully used to predict the crystal structures in a large amount of different compounds [115, 116, 117, 118, 119, 120, 121, 122, 123]. In fact, in the first blind test of inorganic crystal structure prediction, USPEX outperformed both random sampling and simulated annealing.

3.2.6 Particle swarm optimization

Particle swarm optimization [124, 125] was initially designed to study social behavior. It was recently adopted for structure prediction schemes in an evolutionary approach.

The search algorithm is inspired by bird swarms in their collective motions, which can be interpreted as an approach of performing a multidimensional search. Similar to genetic algorithms, a population (called swarm) of configurations (called particles) evolves during the simulation while gradually improving the quality of the structures. An implementation of this approach in crystal structure prediction method is available in the CALYPSO (Crystal structure AnaLYsis by Particle Swarm Optimization) software package [126].

Within CALYPSO, the initial swarm is populated by randomly generating input structure based on space group symmetry. One of the 230 crystallographic space groups is first selected with equal probability and a cell is assigned in accordance to the corresponding Bravais lattice. The cell is then randomly filled with atoms taking into account the space group symmetry operations (further discussion on symmetrized input structures can be found in section 3.3.5). Local structure relaxations are then performed for all members of the initial swarm, and identical or high energy structures are eliminated.

The algorithm to produce the next generation of the swarm is based on fictitious velocities of the swarm and their particles and is characterized by vectors in the high dimensional search space. However, since there is no physical correspondence to such velocities, its definition is somewhat arbitrary. In CALYPSO, the positions \mathbf{X}_i of a particle i is updated according to:

$$\mathbf{X}_i^{t+1} = \mathbf{X}_i^t + \mathbf{V}_i^{t+1} dt \quad (3.12)$$

where dt is a fictitious constant time-step. The particle velocities are updated based on the following equation:

$$\mathbf{V}_i^{t+1} = w\mathbf{V}_i^t + c_1 r_1 (\mathbf{P}_{\text{best},i}^t - \mathbf{X}_i^t) + c_2 r_2 (\mathbf{G}_{\text{best},i}^t - \mathbf{X}_i^t) \quad (3.13)$$

where $w \in [0.4, 0.9]$ is the inertia weight to control the momentum of the particle which can be dynamically adjusted, \mathbf{V}_i^t is the current velocity, $c_1 = c_2$ are adjustable parameters and fixed to 2 based on experience, $\mathbf{P}_{\text{best},i}^t$ is the coordinate with the lowest enthalpy which particle i has already visited (personal best coordinate), \mathbf{X}_i^t is the current coordinate, and $\mathbf{G}_{\text{best},i}^t$ is the coordinate of the particle with the overall lowest enthalpy. r_1 and r_2 are random variables uniformly distributed between 0 and 1, to ensure a non-deterministic exploration of the search space without being trapped in an energy funnel. The velocities are initialized randomly and are scaled in every generation such that their magnitudes do not exceed a certain threshold to avoid violent moves of the particles. To preserve a structural diversity within the swarm, high energy structures are replaced by new randomly generated structure in every generation.

In contrast to genetic algorithms, no variation operations need to be defined, such that the efficiency can be tuned easily by changing a small set of parameters defining the direction and velocity of the swarm. Through the use of symmetry operations, the search space is drastically reduced and accelerates the prediction scheme. However, parameters such as dt and w need to be carefully tuned, and since the velocities are fictitious, unphysical structures can be generated during the update procedure. CALYPSO has been used to predict high pressure phases of several materials: [127, 128, 129, 128, 130, 131, 132]

3.2.7 Random search

Random search methods [133, 134, 135, 136, 137, 138, 139, 140, 141] have now been around for over fifty years and found applications in various optimization problems. It has recently been successfully applied in crystal structure prediction and for molecular systems. The recipe of random search is straight forward: randomly generate a trial structure, locally relax this structure, and repeat the first two steps until the search is converged. The main advantage of this method is its simplicity which makes it easy to implement. However, random searches are not very efficient and do not guarantee that the ground state will ever be found. Nevertheless, random search has been found to correctly and reliably predict structures with low energies for small systems with a rather moderate number of degrees of freedom, whereas larger systems tend to have more complex energy landscapes which are difficult to be dealt with using random search algorithms. Its success is based on the assumption that the energies of local minima correlate strongly with the size of their catchment basins, i.e. low-lying minima are surrounded by a large basin of attraction. The probability of finding such a low-lying structure when starting a local geometry optimization from a random configuration is therefore higher. This can be seen from Figure 3.2. A one-dimensional energy landscape with equally spaced minima are approximated by parabola with fixed curvatures. For minima which are considerably lower in energy than neighboring minima the area of its catchment basin is larger as one can see for the global minimum in this example. Although this principle holds for energy landscapes with well defined global minima it does not hold for glassy systems where a large amount of local minima are very close in energy.

It is very important to provide a sophisticated guess for the trial structure to reduce the search space. Nonphysical trial structures should be identified and eliminated since they

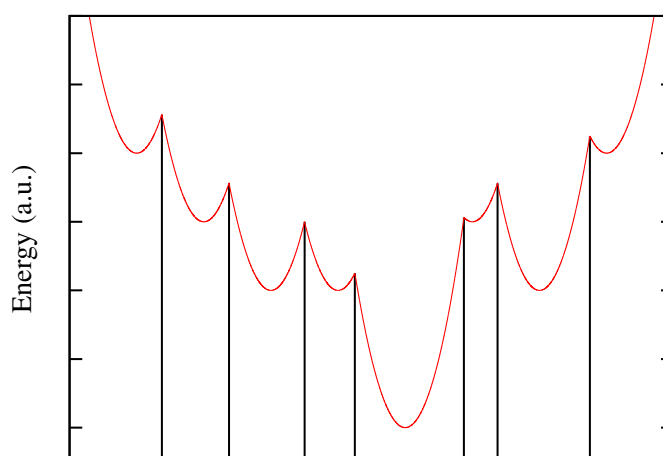


Figure 3.2: A simple one-dimensional energy landscape approximated by parabola. The vertical lines indicate the spacing between the catchment basins of each local minimum.

will, on average, lead to high energy structures even after relaxation. Constraints on the cell volume and inter-atomic distances are used to eliminate bad trial structures. Input guesses are therefore usually created by first generating a simulation cell with random cell lengths and angles to give a volume close to some target value. Then, atoms are randomly placed in the cell, taking into account bond preferences, molecular subunits and atomic radii. This process requires a-priori knowledge of the chemical bond properties and atomic arrangements.

Pickard *et al.* [141] have implemented several other techniques to enhance the quality of trial structures. Even for non-molecular crystals chemical properties of the constituent atoms can be exploited to form sub-units. For example, if in a binary compound the formula unit is given by A_nB_m , it is often desirable to use exactly these units as building blocks of the crystal. In this way, one can obtain more uniformly distributed trial structures. Furthermore, coordination numbers depend highly on atomic species and chemical bonds and can be therefore used to bias the search. Symmetries can also be exploited to generate good trial structures. Since, statistically, high symmetry structures are observed more frequently in nature as the ground state than such with low or no symmetry at all, constraints can be applied to bias the structure towards higher symmetry. If the target number of formula units per cell is given by $N_{f.u.}$, a space group is randomly chosen such that $N_{f.u.}$ is a multiple of its number of symmetry operations N_s . Then, the random cell is partially occupied by $N_{f.u.}/N_s$ formula units, and the remaining atomic positions are obtained by applying the N_s symmetry operations (for detailed discussion see also section 3.3.5).

Other techniques include post processing of the locally relaxed structures. “Shaking” is based on the assumption that low energy structures are close to even lower energy structures nearby in the configurational space. Random atomic and cell displacements are used to escape from the current catchment basin and to find new structures through a subsequent local relaxation. Furthermore, phonon spectrum analysis can be carried out to identify low frequency modes or modes associated to imaginary phonons of a minimized structure. Following such eigenmodes in super-cells will lead to even lower energy structures. However, phonon calculations are computationally expensive and can only be carried out for a small selection of good candidate structures.

3.3 Minima hopping method

The minima hopping method [8] is an efficient algorithm to find the global minimum configuration by minimizing the potential energy of a complex system. This method is not based on thermodynamic principles like some standard algorithms but on the fact that by exploring the low energy part of the PES as fast as possible the global minimum will be revealed at some point. In order to strive through the low energy configurations many local minima separated by potential barriers have to be visited.

The minima hopping simulation will start with an arbitrary configuration in a certain funnel on the PES. Due to high barriers surrounding the funnel the system will be trapped in it although the lowest minima within the funnel can be found quickly. The idea of the MHM is to avoid revisiting already explored minima and to overcome the high barriers surrounding the funnel in such a way that new, energetically lower funnels can be visited and explored efficiently.

3.3.1 The algorithm

The MHM uses a walker to explore the PES by consecutively visiting local minima. This is done by “hopping” from one minimum to the next using molecular dynamics based escape moves and local geometry relaxations. The algorithm of the MHM is divided into two parts: while the *inner part* is responsible for the jumps into a neighboring local minimum the *outer part* is used to accept or reject this minimum.

After the inner part has performed a move into a new local minimum M it is accepted by the outer part if its energy $E(M)$ is less than the sum of the energy $E(M_{\text{cur}})$ of the previous minimum M_{cur} and a positive energy parameter E_{diff} . During the simulation, E_{diff} is adjusted such that half of the new minima are accepted and half are rejected by the outer part. This outer mechanism ensures that the accepted minima have a preference for decreasing energies. E_{diff} will increase by a factor of $\alpha_2 > 1$ if a move into a minimum with higher energy than $E(M_{\text{cur}}) + E_{\text{diff}}$ is proposed by the inner part, and it will be decreased by a factor $\alpha_1 < 1$ if the energy is lower. In this way the parameter E_{diff} is adjusted throughout the simulation such that in average half of the proposed minima are rejected and half are accepted. It can be shown that this condition is obtained if $\alpha_2 = \frac{1}{\alpha_1}$ (see appendix C). Hence, if the inner loop exclusively proposes high energy structures these moves will eventually be accepted as well.

The escape moves performed by the inner part is implemented by a molecular dynamics (MD) simulation, during which the system has a random Boltzmann velocity distribution with a kinetic energy E_{kin} . In order to escape from the current minimum M_{cur} into a new basin of attraction, E_{kin} has to be larger than the height of the potential barrier between neighboring minima. The MD simulation is stopped as soon as md_{min} potential energy maxima have been crossed and the md_{min} -th minimum has been reached along the MD trajectory. Then, a local geometry relaxation is performed to the new minimum M . The relaxed structure is either the same as the initial configuration before the MD simulation or a configuration that was already visited before, or it is a new one that has not been discovered in previous steps.

Although a high kinetic energy will result in a higher possibility of finding new minima in each escape move it is not desirable to cross high barriers. In chemistry, the Bell-Evans-Polanyi [77] principle states that strongly exothermic reactions have a low activation

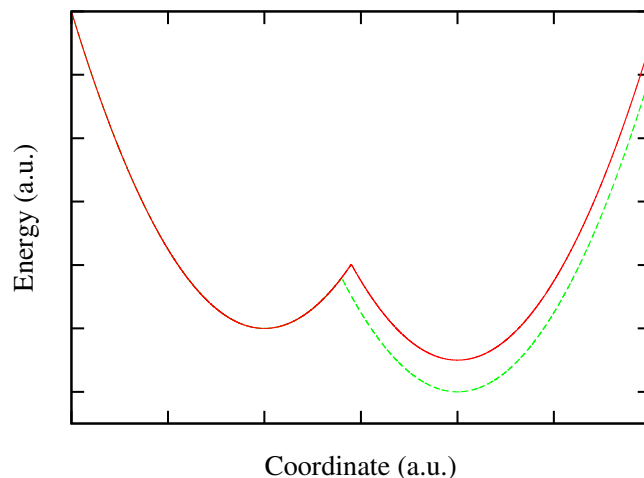


Figure 3.3: Illustration of the Bell-Evans-Polanyi principle.

energy. Reactant and product are in fact neighboring local minima on the PES and the chemical reaction is a transition of an energy barrier connecting the two minima. Hence, the Bell-Evans-Polanyi principle can be generalized to any transitions between local minima on the PES during MD simulations. Recently, Roy *et al.* have shown that, on average, crossing low energy barriers along MD trajectories will lead into the basin of attraction of lower energy local minima than crossing high energy barriers [142]. The BEP is illustrated for a simple model in Figure 3.3. A one dimensional energy landscape is approximately represented by two red parabola. The energy barrier connecting the two minima is lowered as the energy of the product is reduced (shown in green). Therefore, a high kinetic energy will result in visiting a lot of undesirable local minima. On the other hand choosing E_{kin} too small will demand many MD simulations until an escape path is found. Therefore, E_{kin} is continuously adjusted: it is decreased by a factor β_3 if the escape trial is successful, and increased by a factor of β_1 and β_2 if the escape trial was unsuccessful or if the structure has been visited before, respectively. The latter feedback mechanism requires that local minima are reliably distinguished, which can be achieved for example by their energies. Therefore, the energies of all visited configurations are kept in a history list. A flowchart of the algorithm is shown in Figure 3.4.

3.3.2 Minima hopping method vs. other methods

The MHM is not based on thermodynamic principles, thus allowing to overcome high energy barriers more quickly. There are some similarities to basin hopping in the sense that also a walker is used to explore the PES. However, molecular dynamics is applied when performing moves on the PES, which has several advantages over random displacements as applied in basin hopping. First of all, highly unphysical high energy structures are

avoided when performing moves on the PES: during escape trials the kinetic energy at the start of the molecular dynamics trajectory is finite, hence the Newton's equations can be integrated with sufficient accuracy. Secondly, molecular dynamics can overcome several barriers within a few number of time-step. This is favorable over single barrier transitions, as demonstrated by Sicher *et al.* [143]. At last, using molecular dynamics as escape trials statistically leads to low energy structures, as illustrated by the Arrhenius equation (which states that low energy barriers can be more easily overcome) together with the Bell-Evans-Polanyi principle [77] (which states that low activation barriers will lead to strongly exothermic reactions).

Comparative studies have been carried out recently to determine the difference in efficiency between genetic algorithms and the MHM [114, 144]. Lennard-Jones, silicon and gold clusters were investigated by Schönborn *et al.* [114] who concluded that genetic algorithms are well suited if the ground state structures are highly symmetric, but they are less efficient for very complex energy landscapes. Ji *et al.* [144] investigated Al_xSc_{1-x}

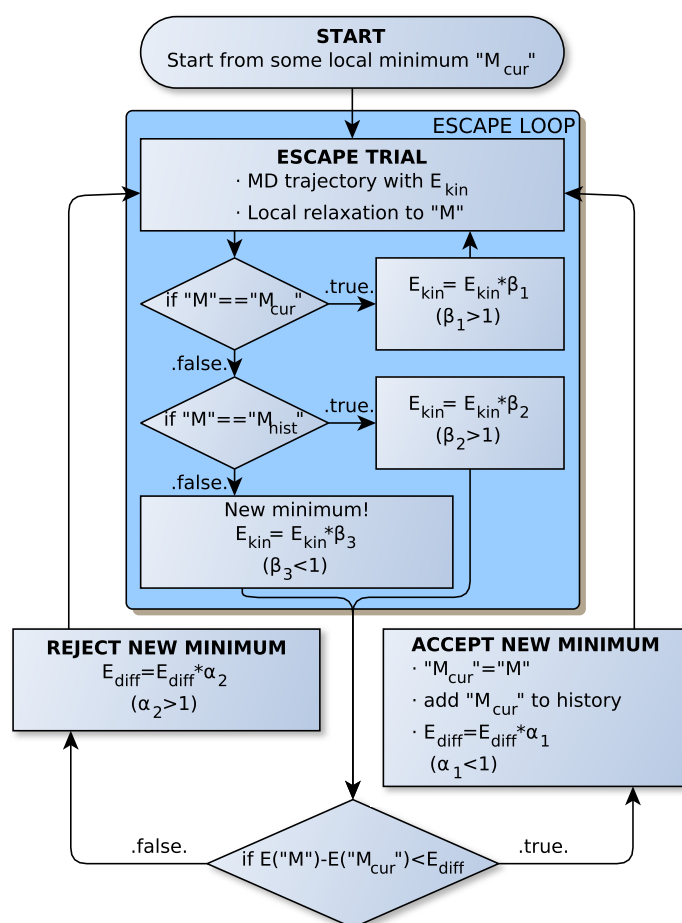


Figure 3.4: The minima hopping algorithm flowchart.

and boron crystals of various system sizes, and the genetic algorithm was found to be more efficient in terms of the number of scanned minima for larger cells. However, since unphysical configurations can be obtained during the mating operations within the genetic algorithm, local relaxations were found to be more expensive computationally than within the MHM.

3.3.3 Generalization to periodic systems

The initial implementation of the MHM method was capable of performing a search for low-lying minima on the $3N$ -dimensional PES $E = E(\{\mathbf{r}_i\})$, $i = 1, \dots, N$, of an isolated molecule or a periodic system in a rigid box with N atoms. However, it is essential for the purpose of structure prediction in periodic systems that not only the atomic positions are allowed to be optimized, but also the cell shape, especially when external constraints are imposed. Furthermore, using a variable cell shape reduces the enthalpy barriers for phase transitions. Hence, to generalize the MHM method for periodic systems with variable cell shape, the degrees of freedom are augmented by the three variable cell vectors \mathbf{a} , \mathbf{b} and \mathbf{c} in $h = \{\mathbf{a}, \mathbf{b}, \mathbf{c}\}$, as discussed in section 3.1. Again, the atomic positions can be expressed by vectors in lattice coordinates \mathbf{s}_i according to $\mathbf{r}_i = h\mathbf{s}_i$, and the potential energy is replaced by the configurational enthalpy $H = E(\{\mathbf{s}_i\}, h) + P\Omega(h)$ when an external pressure P is imposed. Periodic boundary conditions are applied for the evaluation of H .

Fully unconstrained local geometry relaxations must be carried out by optimizing the atomic and cell vectors to identify stable structures (see section 3.1 for details). Similarly, for the escape step, the MD needs to be performed taking into account the additional cell parameters. Hence, both the atomic positions in lattice coordinates $\mathbf{s}_i(t)$ and the lattice vectors $h(t)$ are time-dependent. A Lagrangian to perform variable cell shape MD at constant pressure P was proposed by Parrinello and Rahman in 1980 [62] and has been widely applied:

$$\mathcal{L} = \sum_{i=1}^N \frac{m_i}{2} \dot{\mathbf{s}}_i^T g \dot{\mathbf{s}}_i - E + \frac{W}{2} \text{Tr}(\dot{h}^T \dot{h}) - P\Omega \quad (3.14)$$

where $g = h^T h$ is the metric tensor, W is the fictitious mass of the simulation cell and m_i is the mass of atom i . The first two terms in equation (3.14) correspond to the kinetic and potential energy of the atoms, respectively. The third and the fourth term correspond to the kinetic and potential energy of the simulation cell, respectively. The sum of the terms two and four is simply the negative enthalpy of the system. In fact, $E = E(\{\mathbf{s}_i\}, h)$ can be readily computed for any many-body potential which are expressed by atomic positions, such as DFT calculations.

The symmetrized dynamical stress tensor Π can be written as

$$\Pi = \frac{1}{\Omega} \left(\sum_{i=1}^N m_i \mathbf{v}_i \mathbf{v}_i^T - f^h h^T \right) \quad (3.15)$$

where we use the cell gradients of the potential energy $f_{\alpha\beta}^h = \frac{\partial E(\{\mathbf{s}_i\}, h)}{\partial h_{\alpha,\beta}}$ and define $\mathbf{v}_i = h\dot{\mathbf{s}}_i$. The second term in equation (3.15) is related to the Cauchy stress tensor $\sigma_{\alpha\beta} = -\frac{1}{\Omega} \frac{\partial E}{\partial \epsilon_{\alpha\beta}}$ (the stress tensor for the static case) by $f^h h^T = -\Omega\sigma$, where ϵ is the strain tensor (see appendix A or Ref. [145])

Using the Lagrange's equation, the equations of motion for the atomic positions in lattice coordinates and the cell vectors are then given by

$$\ddot{\mathbf{s}}_i = -\frac{g^{-1}}{m_i} \frac{\partial E}{\partial \mathbf{s}_i} - g^{-1} \dot{g} \dot{\mathbf{s}}_i \quad (3.16)$$

$$\ddot{h} = \frac{1}{W} (\Pi - P) \eta \quad (3.17)$$

where

$$\eta = \{\mathbf{b} \times \mathbf{c}, \mathbf{c} \times \mathbf{a}, \mathbf{a} \times \mathbf{b}\} \quad (3.18)$$

A detailed derivation of above equations is given in appendix B. The cartesian Hellman-Feynman forces from DFT calculations can be directly employed if we use the identity $\frac{\partial E(\{h\mathbf{s}_i\})}{\partial \mathbf{s}_i} = h^T \frac{\partial E(\{\mathbf{r}_i\})}{\partial \mathbf{r}_i}$ in equation (3.16):

$$\ddot{\mathbf{s}}_i = -\frac{h^{-1}}{m_i} \frac{\partial E}{\partial \mathbf{r}_i} - g^{-1} \dot{g} \dot{\mathbf{s}}_i \quad (3.19)$$

The tensor in the second term of equation (3.16) and (3.19) can be expanded to

$$g^{-1} \dot{g} = (h^T h)^{-1} (\dot{h}^T h + h^T \dot{h}) \quad (3.20)$$

Since the forces are velocity-dependent, the time integration should be performed by an advanced integration scheme to correctly find the numerical solution of the equations of motion (3.16) and (3.17) (for example the symplectic Runge-Kutta method or a predictor-corrector scheme). However, we are only interested in escaping the local minimum and we only perform short MD runs with few oscillations in the potential energy. Therefore, the long-time conservation of the total energy is not an issue and we can simply use finite differences to discretize the equations of motion, equivalent to the Verlet algorithm.

If we define the following generalized forces

$$\mathbf{f}_i := -g^{-1} \frac{\partial E}{\partial \mathbf{s}_i} \quad (3.21)$$

$$F := (\Pi - P) \eta \quad (3.22)$$

and use finite difference formulae for $\ddot{\mathbf{s}}_i$, $\dot{\mathbf{s}}_i$ and \ddot{h} , the time evolution of the atomic positions and the cell vectors can be computed iteratively according to

$$\mathbf{s}_i(t + \Delta t) = \mathbf{s}_i(t) + \Delta t \dot{\mathbf{s}}_i(t) + \Delta t^2 \left(\frac{1}{m_i} \mathbf{f}_i(t) - g^{-1}(t) \dot{g}(t) \dot{\mathbf{s}}_i(t) \right) \quad (3.23)$$

$$h(t + \Delta t) = h(t) + \Delta t \dot{h}(t) + \Delta t^2 \frac{1}{W} F(t) \quad (3.24)$$

where we use $\dot{\mathbf{s}}_i(t) = \frac{\mathbf{s}_i(t) - \mathbf{s}_i(t - \Delta t)}{\Delta t}$ and $\dot{h}(t) = \frac{h(t) - h(t - \Delta t)}{\Delta t}$, which can be considered as velocities of the corresponding variables.

3.3.4 Softening and optimizing cell parameters

Softening, a method of biasing the initial velocities for the MD simulation of the escape step, is used to increase the efficiency of the MHM [114]. For the crystal structure prediction MHM the velocity vector consists not only of atomic velocities, but also of the cell velocities. First, a random velocity direction with Gaussian distributed magnitudes is chosen. The initial velocity amplitude is chosen that the kinetic energy is small, allowing only low barriers to be crossed during the MD escape, based on the assumption that the BEP is applicable on average. Furthermore, low energy barriers are generally connected to low frequency eigenmodes of local minima [143]. These two properties can be readily extended to the enthalpy. Therefore, the probability of finding low enthalpy configurations can be expected to increase when the direction of the initial velocity vector of a MD run points toward a direction with low curvature. Hence, in a second step, the velocity vector from the first step is rotated such that it is oriented along soft mode directions of the current minimum. The rotation procedure is performed by iteratively minimizing the energy along the escape direction at a constant distance from the local minimum [114]. However, over-biasing the velocities is not favorable since the random and therefore ergodic character of the escape step should be retained in order not to arrive at a deterministic process. In fact, *softening* is mainly applied to eliminate components of the velocity on hard modes.

For molecular crystals the *softening* procedure is especially useful to preserve molecular subunits during MD escape trials. Intermolecular interaction are usually soft and mediated by ionic or weak Van der Waals forces, whereas atoms within the molecules have stronger covalent bonds which cannot be easily broken. By eliminating velocities along high curvature directions the global motion of the molecules can be enhanced and intramolecular vibrations can be avoided, which could lead to undesired breaking of atomic bonds.

If a quasi-Newton method (like the BFGS method) is used to perform local geometry optimization within the MHM an alternative *softening* procedure is possible. In a quasi-Newton method an approximate Hessian matrix is continuously updated during a geometry relaxation. Before performing the MD escape step the approximate Hessian matrix from the previous relaxation step is diagonalized and a small number of low frequency eigenvectors are extracted. A randomized superposition of these eigenvectors are then used to provide the initial, soft velocity vector for the following MD trajectory. If feasible, the Hessian matrix can also be computed analytically to evaluate the soft mode directions.

Softening has been successfully used in previous applications of the MHM [114, 13, 14]. In Table 3.2 the performance of the MHM with and without *softening* is compared for a benchmark system, a BLJ mixture with type A and B atoms in a small cell, A_8B_4 . It can be clearly seen that the curvature of the enthalpy along the velocity direction is reduced by roughly one order of magnitude when *softening* is used. The significant increase in the efficiency when *softening* is applied can also be ascribed to improving the cell velocities, since the impact of cell parameters on the structure can be larger than the atomic coordinates. For cells with a small number of atoms this can be illustrated by a simple example. Consider a simulation cell containing one single atom at the origin. The lattice vectors are given by $\mathbf{a} = \frac{a}{2}(\hat{y} + \hat{z} - \hat{x})$, $\mathbf{b} = \frac{a}{2}(\hat{z} + \hat{x} - \hat{y})$ and $\mathbf{c} = \frac{a}{2}(\hat{x} + \hat{y} - \hat{z})$ (where the hats denote the unit vectors and a is the lattice constant), which define a body-centered lattice. Assume the atomic coordinates \mathbf{s} were fixed. Transforming the cell to $\mathbf{a}^* = \frac{a}{2}(\hat{y} + \hat{z})$, $\mathbf{b}^* = \frac{a}{2}(\hat{z} + \hat{x})$ and $\mathbf{c}^* = \frac{a}{2}(\hat{x} + \hat{y})$ will result in a face-centered cubic lattice, a totally different structure. However, when the cell parameters \mathbf{a} , \mathbf{b} and \mathbf{c} are fixed, there is no possibility to transform the atomic coordinates \mathbf{s} to a system where a face-centered cubic lattice is obtained. Obviously, the impact of the cell parameters decreases with increasing number of atoms, which is equivalent to the limit where an infinitely large cell is used. Similarly, this principle is also used in metadynamics simulations where the cell parameters are chosen as the collective variables (see section 3.2.3 for details). The effect of *softening* on the efficiency of the MHM is in general larger for small periodic cells with a low number of atoms than for isolated molecules of similar size.

The fictitious cell mass W is another adjustable parameter. Choosing a too large ratio for cell and atomic mass will result in a very stiff cell which will not adjust itself smoothly

Table 3.2: The impact of *softening* on various quantities of the MHM is shown. Starting from 100 different random input configurations all runs were continued until the ground state structure was found, resulting in a success rate of 100%. The first column shows the different degrees of freedom (DOF) that are taken into account during *softening*. The second and third column show the median value of the curvature of the enthalpy $\tilde{\kappa}$ along the initial MD velocity direction before ($\tilde{\kappa}_b$) and after ($\tilde{\kappa}_a$) *softening*, respectively. The fourth column contains the median value of the number of visited minima \tilde{n}_{\min} before reaching the global minimum. A BLJ mixture with A_8B_4 atoms was used described by the modified Lennard-Jones potential as discussed in section 4.1. The parameters were set to $\sigma_{AA} = 1.50$, $\sigma_{AB} = 2.25$, $\sigma_{BB} = 3.00$ and $\epsilon_{AA} = 1.00$, $\epsilon_{AB} = 1.25$, $\epsilon_{BB} = 1.00$, and a cutoff radius of $r_{\alpha\beta}^{cut} = 2.5\sigma_{\alpha\beta}$ was used.

[§]The number of *softening* iterations was doubled.

[†]Initial atomic velocities were set to zero before *softening*.

<i>Softening</i> DOF	$\tilde{\kappa}_b$ ($\epsilon_{AA}/\sigma_{AA}^2$)	$\tilde{\kappa}_a$ ($\epsilon_{AA}/\sigma_{AA}^2$)	\tilde{n}_{\min}
None	806.22	806.22	21.0
Atoms	809.55	105.35	16.0
Atoms & Cell	813.62	74.18	11.5
Atoms & Cell [§]	829.77	52.33	11.0
Atoms & Cell [†]	111.32	64.47	10.5
Atoms & Cell ^{†§}	112.62	50.73	8.0

during the simulation. However, when this ratio is too small the cell can fluctuate violently resulting in a strong deformation of the cell within one step of the simulation. We have found that choosing the cell mass similar to the atomic masses is a reasonable choice.

During a MHM simulation it can happen that the cell shape gets heavily distorted leading to small angles between the three lattice vectors, and thus resulting in a very flat cell. This behaviour is not desired since it makes it difficult to identify equivalent structures in different cells. Therefore, whenever necessary, a transformation of the cell vectors is performed to obtain shorter cell vectors (for details see Ref. [146]).

3.3.5 Seeding initial structures

The initial structure determines the funnel of the PES which is first explored in a MHM simulation. Optimally, this initial funnel contains the global minimum in which case it can be found rapidly within a few minima hopping steps. The efficiency in finding the global minimum structure in simple single-funnel systems is therefore independent of the initial structure. However, in a general multi-funnel system there is no a priori knowledge about the energy landscape, in particular one cannot predict which funnel contains the global minimum and which initial structure belongs to which funnel. Therefore, the efficiency of a MHM simulation can depend significantly on the initial structure. Similar to the task of preserving a diverse genetic pool in evolutionary algorithms, the most promising approach is to start several MHM runs simultaneously with a set of different initial structures. Random structures constrained through simulation cell volume and minimal inter-atomic distances are commonly used and give a reasonable initial sampling of the energy landscape. More sophisticated algorithms can contain chemical information such as bond-angles and molecular subunits.

Symmetries play an important role for classifying structures in crystallography. They are defined by combinations of 32 point group elements, which include reflection, rotation, rotinversion, glide planes and screw axis, together with the 14 Bravais lattices in 3 dimensions. In total there exist 230 crystallographic space groups, which are documented and assigned a space group index (SGI) in the “International Tables of Crystallography A” [147]. Although the indexing is arbitrary the overall symmetry increases with the SGI (for example SGI = 1 is described by a triclinic cell and the identity operator \mathbb{I} , SGI = 2 additionally contains an inversion center, etc.). Symmetry operations can be represented by a 3×3 matrix M and a translational vector \mathbf{d} , which are used to operate on an arbitrary point in space \mathbf{r} according to $\mathbf{r}' = M\mathbf{r} + \mathbf{d}$. For convenience, M and \mathbf{d} can be combined in a 4×4 matrix \mathbb{M} to operate on an extended vector $\mathbf{R} = (\mathbf{r}, 1)$ in \mathbb{R}^4 :

$$\mathbb{M} = \begin{pmatrix} M & \mathbf{d} \\ 0 & 1 \end{pmatrix} = \begin{pmatrix} M_{1,1} & M_{1,2} & M_{1,3} & d_1 \\ M_{2,1} & M_{2,2} & M_{2,3} & d_2 \\ M_{3,1} & M_{3,2} & M_{3,3} & d_3 \\ 0 & 0 & 0 & 1 \end{pmatrix}, \quad \mathbf{R} = \begin{pmatrix} r_1 \\ r_2 \\ r_3 \\ 1 \end{pmatrix} \quad (3.25)$$

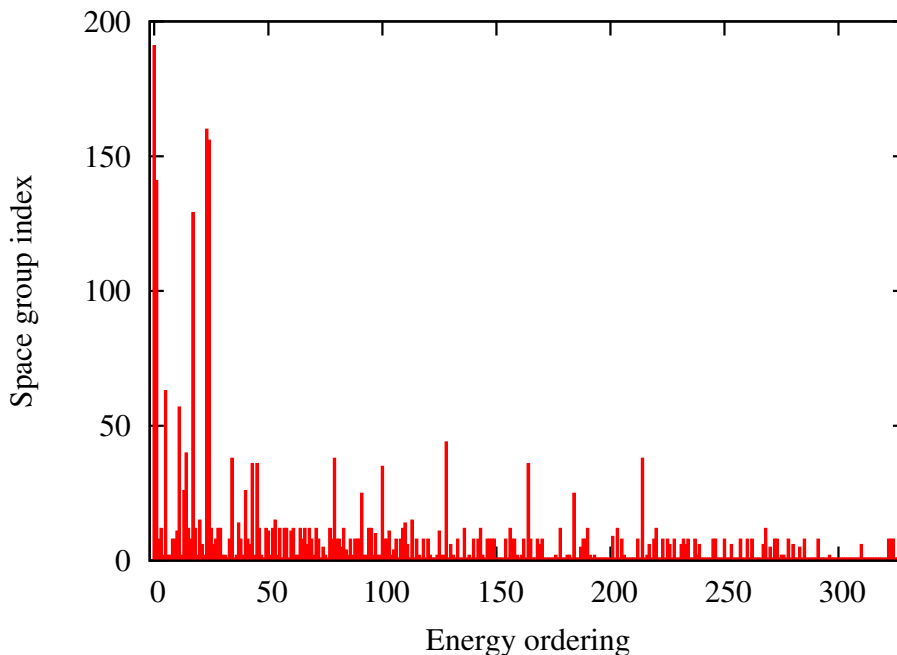


Figure 3.5: Random input structures were used to seed 10 MHM runs of binary Lennard-Jones mixtures with A_8B_4 atoms described by the modified Lennard-Jones potential as discussed in section 4.1. The parameters were set to $\sigma_{AA} = 1.50$, $\sigma_{AB} = 2.25$, $\sigma_{BB} = 3.00$ and $\epsilon_{AA} = 1.00$, $\epsilon_{AB} = 1.25$, $\epsilon_{BB} = 1.00$, and a cutoff radius of $r_{\alpha\beta}^{cut} = 2.5\sigma_{\alpha\beta}$ was used. The simulations were terminated after finding 50 distinct local minima for each run. These structures were then sorted according to their energies and analyzed with respect to their symmetries, giving totally more than 300 distinct minima. The space group indexes of the minima are shown with respect to their energy ordering.

Depending on the symmetry elements of a given space group, all points in a crystal are characterized as so-called general or special Wyckoff positions. Special Wyckoff positions are invariant under at least one symmetry operation of a given space group, whereas general Wyckoff positions are points without high symmetry.

An analysis of structural databases shows that frequencies with which structures are observed in nature are not uniformly distributed among the space groups [148]. Several statistical evaluations are available in the world wide web which list analysis of space group frequencies ¹. We analyzed all structures in the Crystallography Open Database ² with respect to the reported SGI. Only 0.76% of the structure have no symmetry at all (except identity, SGI = 1). Therefore, we conclude that symmetric structures are more likely to be found in ground state crystal structures predicted with the MHM. The most frequent SGI of the statistical evaluation are shown in table 3.3.

Furthermore, a symmetry analysis of structures found in MHM simulations of all systems

¹<http://pd.chem.ucl.ac.uk/pdnn/symm3/sgpfreq.htm> and
http://www.bmsc.washington.edu/CrystalLinks/space_group_freq.html

²<http://www.crystallography.net>

we have investigated so far clearly shows that high symmetry structures appear more often at lower energies. This behavior is illustrated for a model system in Figure 3.5. Structures found in ten different MHM simulations on a Lennard-Jones mixture are ordered according to their energies and the corresponding space group indexes are plotted along the y -axis. The corrected Spearman’s rank correlation coefficient is $\rho_S = -0.52$, which indicates that the space group index ordering is fairly anti-correlated with the energy ordering (a perfect anti-correlation would result in $\rho_S = -1.0$ and no correlation in $\rho_S = 0.0$, see Ref. [58] and references therein for details). Therefore, seeding MHM simulations with high symmetry structures should statistically increase the probability of starting from structures close to the global minimum.

Another important benefit from using symmetrized input structures to improve the efficiency of the MHM is related to the unconstrained search algorithm underlying in the MHM. In general, MHM simulations are performed without any constraints on atomic or cell degrees of freedom which is perfectly desirable when an extensive exploration of the PES is performed. Symmetric structures are however more easily broken than created within a single MHM step. This can be demonstrated if we look at the ground state structure of silicon for example. Consider a perfect diamond silicon supercell with N atoms, where N is an even number. The energetically most accessible and stable single point defect is the fourfold coordinated site defect [52], which can be created by a single Wooten-Winer-Weaire displacement of two close-by atoms [149]. The number of possibilities for creating a single FFCD and thus destroying the symmetry is proportional to the number of atomic sites N . On the other hand, there is only one way to regain the perfect diamond crystal containing a single FFCD by displacing the two affected atoms. In the MHM this imbalance is counteracted to some extent by using the *softening* procedure and

Table 3.3: Space group analysis of 191902 structures from the Crystallography Open Database. The first two columns contain the data obtained from the whole database, whereas the columns 3 and 4 contain the SGI and their frequencies published in “American Mineralogist”

All structures (191902)		American Mineralogist (4955)	
SGI	%	SGI	%
14	32.6	227	13.6
2	22.0	12	9.7
15	8.6	15	9.4
19	5.2	62	8.4
4	4.2	14	7.7
61	2.9	225	6.7
62	1.8	2	6.0
33	1.3	230	3.3
12	1.2	148	2.3
227	1.0	11	2.0

Table 3.4: The impact of seeding the MHM simulations with symmetrized input structure is shown for a $A_{16}B_8$ Lennard-Jones mixture with the same parametrization as above. 100 MHM runs from different input structures were carried out with each method. The first column describes the method used to generate the input structures, whereas column 2 contains the average number of visited minima \bar{n}_{\min} before reaching the global minimum. Since some of the input structures relaxed within the first MHM step to the global minimum, we eliminated such runs for a corrected statistical evaluation in the next three columns. The corrected average $\bar{n}_{\min}^{\text{corr.}}$ is shown in column 3, and columns 4, 5, and 6 contain the first, second and third quartile (Q_1 , Q_2 , Q_3).

Input seed	\bar{n}_{\min}	$\bar{n}_{\min}^{\text{corr.}}$	Q_1	Q_2	Q_3
Random	1291.34	1304.38	249.0	851.0	2193.0
Symmetric, 1 cell	614.42	787.47	20.0	221.5	1142.0
Symmetric, 2 cells	300.99	411.94	14.0	37.0	373.0
Symmetric, 4 cells	422.75	570.94	16.0	89.0	774.0
Symmetric, 8 cells	107.52	305.34	2.0	3.0	220.0

MD as the escape step, exploiting the fact that the barrier height of creating a defect is larger than to obtain the perfect crystal. However, starting (or periodically re-seeding) a MHM simulation with a highly ordered structure can significantly improve its efficiency.

We implemented a structure generator to investigate the influence of symmetrized input structures on the MHM efficiency. First, a SGI is chosen at random and the corresponding symmetry operations are identified. Then, trial particles are placed into the appropriate cell and all symmetry operations are applied. Wyckoff positions with high symmetry are treated with special care and are specifically included into the trial structures. Structures and space groups where the correct stoichiometry cannot be obtained or where the atomic distances are too short given a target cell volume are rejected. Sub-cells can be defined to create a crystal made from smaller primitive building blocks.

A statistical analysis on a $A_{16}B_8$ Lennard-Jones mixture was carried out with different seeding techniques. Besides generating structures with the full number of atoms per cell, smaller cells containing $1/2$, $1/4$ and $1/8$ of the total number of atoms were generated and used to span a super-cell with the correct composition. Table 3.4 contains the average number of local geometry optimizations before reaching the global minimum, which belongs to the $P6/mmm$ space group with three atoms A_2B_1 per cell. Employing symmetrized input structures clearly enhances the efficiency of the MHM, and utilizing sub-cell constructions introduces a further improvement of the method.

3.3.6 Parallelization and lattice vector prediction

Another benchmark system was investigated with the MHM, a silicon supercell with 64 atoms at zero pressure. Since the number of local minima increases exponentially with respect to the number of atoms in a system, finding the global minimum of a cell

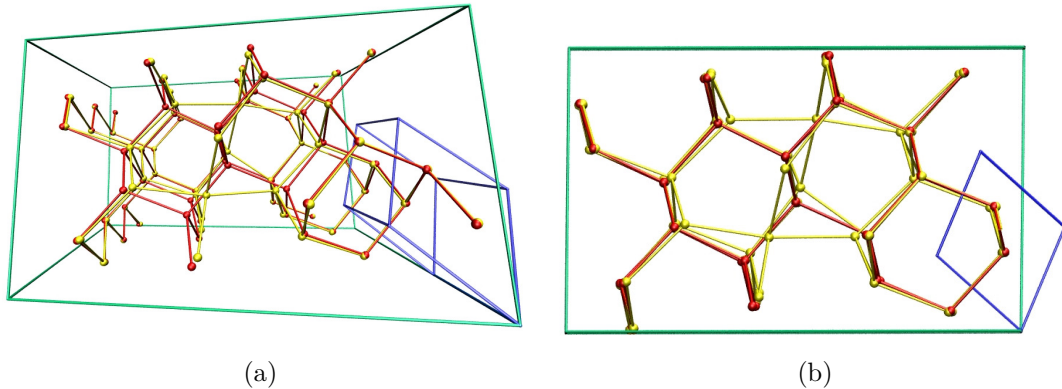


Figure 3.6: The LVPS is illustrated for a Si_{64} supercell in a perspective (a) and a orthographic (b) view. The yellow (light) and red (dark) spheres denote the positions of the atoms before and after applying LVPS, respectively. The resulting supercell consists of 66 atoms. The primitive cell found by the LVPS is shown in the right bottom corner by a blue parallelepiped.

with this many atoms is a challenging task. Furthermore, the silicon supercell with 64 atoms is a system with both crystalline and a large amount of amorphous structures and therefore presents an additional challenge for global optimization. For a silicon supercell with 64 atoms in a rigid box [8] the difficulty of finding the ground state has already been demonstrated. Several million minima had to be visited before finding the ground state, the well-known cubic diamond structure. To demonstrate the advantage of the variable cell shape MHM, we revisit the same problem set. Using the EDIP potential for silicon [45, 46, 47] statistical data were collected for a set of 100 serial MHM runs at zero pressure. Each run started with a highly random configuration (no symmetry) in a distorted cell and was stopped as soon as a structure with ground state energy was found or 8000 distinct minima were accepted, a small number for such a large system. Since some of the local minima are visited several times and only half of the new structures are accepted the search length corresponds to visiting at most some 50 000 minima. The success rate was found to be 45%. Each successful run visited an average of some 13 000 local minima till finding a structure with ground state energy, an improvement in performance by two orders of magnitude compared to the earlier results in [8]. However, since the EDIP potential has only first neighbor interaction, the cubic diamond structure and its polytypes (for example the hexagonal diamond Lonsdaleite structure) all give the same ground state energy. Therefore, only 12 out of the 45 successful runs arrived at the cubic diamond structure. It needs to be emphasized that this is not a shortcoming of the MHM, but an effect of the short range character of the EDIP potential. Increasing the number of distinct and accepted minima to be found will lead to an increase in the success rate. So, when increasing the search length by a factor of 6 the success rate is almost doubled to 80%.

Another approach to increase the success rate of the MHM is by parallelizing the MHM

runs. As discussed above, the success rate of a serial MHM simulation can depend heavily on the initial guess of the structure. Therefore, it is advantageous to start multiple parallel simulations starting from different initial structures. We performed a simple statistical analysis to estimate the computational cost necessary if, instead of performing multiple serial runs with index i , a parallel run is started with m processes of which each requires l_i MHM steps to find the ground state. In the parallel version all processes would be stopped as soon as one of the processes finds the ground state structure. The necessary number of minima to be visited is given by $n_{\min}^m = m \cdot \min\{l_i\}$ where $i = 1, \dots, m$. An average value \bar{n}_{\min}^m should be computed from runs with different initial structures. Then, the optimal number of processes for the particular problem is $m = m_0$ resulting in the minimal value of \bar{n}_{\min}^m . Applied to the Si₆₄ system the computational cost can be reduced to half for $m_0 = 6$, $\bar{n}_{\min}^6 \approx 6200$

For non-periodic systems the identification of structures based on their energies is sufficiently accurate in most cases, but the enthalpy degeneracy of the polytypes within short-ranged potentials requires some additional method to distinguish different structures. Since the most natural characteristic of a structure is its geometry we use a fingerprint function F related to experimental diffraction patterns proposed by Valle *et al.* [112, 56]. A continuous one-dimensional function is defined by summing up weighted Gaussian functions centered at all relative atomic distances. The fingerprint function for a single component system is given in equation (3.26), where r_{ij} are the interatomic distances, $\delta(r - r_{ij})$ are Gaussian-smearred delta functions, N is the number of atoms in the unit cell and V is the unit cell volume. To reduce numerical errors the fingerprint function is discretized into m bins of width Δ , leading to a vector of size m uniquely related to the structure. A cutoff distance larger than the maximal diagonal of the unit cell is applied. Index i runs over all atoms in the simulation cell, and j runs over all atoms within the cutoff range with respect to atom i . By using the angle between two fingerprint vectors a cosine distance is defined which then can be used to determine the similarities between structures.

$$F(r) = \sum_{i \in \text{cell}} \sum_j \frac{\delta(r - r_{ij})}{4\pi r_{ij}^2 \frac{N^2}{V} \Delta} - 1 \quad (3.26)$$

Frequently, when a global optimization run does not reach the global minimum for a long time, the simulation is stuck in an energy funnel with barriers hard to overcome. In most cases of our simulation of Si₆₄ these funnels are determined by lattice vectors which can fit a cubic diamond structure with 62 or 66 silicon atoms, but not exactly the given 64 atoms. In these cases, a diamond structure (or one of its polytypes) fits into the cell perfectly with exception of some defective subregions where 2 Si atoms are either missing or are redundant. For these cases we developed a lattice vector prediction scheme (LVPS) to modify the simulation cell by adding or removing atoms such that a perfect crystalline structure is recreated. We define a scalar field $f(\mathbf{r})$ by summing up Gaussian functions with a width σ on each atomic position \mathbf{r}_i

$$f(\mathbf{r}) = \sum_{i=1}^N \frac{1}{(2\pi\sigma^2)^{(3/2)}} \exp\left(-\frac{(\mathbf{r}_i - \mathbf{r})^\top(\mathbf{r}_i - \mathbf{r})}{2\sigma^2}\right) \quad (3.27)$$

The Gaussian width should be small enough that the overlap between neighboring atoms is vanishingly small. The autocorrelation function is defined as

$$h(\mathbf{r}) = \int_{-\infty}^{\infty} f^*(\boldsymbol{\tau})f(\mathbf{r} + \boldsymbol{\tau})d\boldsymbol{\tau} \quad (3.28)$$

In Fourier space this convolution is simply a multiplication of the individual fourier transformed functions of f^* and f , and according to the Wiener-Chinchin theorem

$$H = \mathcal{F}(h) = (\mathcal{F}(f))^* \cdot \mathcal{F}(f) = |\mathcal{F}(f)|^2 \quad (3.29)$$

where \mathcal{F} denotes the Fourier transform and $*$ denotes the complex conjugate. A transformation back to real space results in the desired autocorrelation function. The autocorrelation function is then scaled such that the peak at the origin is 1, and periodic boundary conditions are applied. The three peaks closest to the origin with an amplitude of more than 0.5 spanning a parallelepiped with a non-vanishing volume give the vectors of a primitive unit cell. Using this cell to span the whole simulation cell, the most common basis is identified and the crystalline structure is reproduced (see Figure 3.6). Using LVPS to identify ground state structures the success rate was further increased to almost 95%.

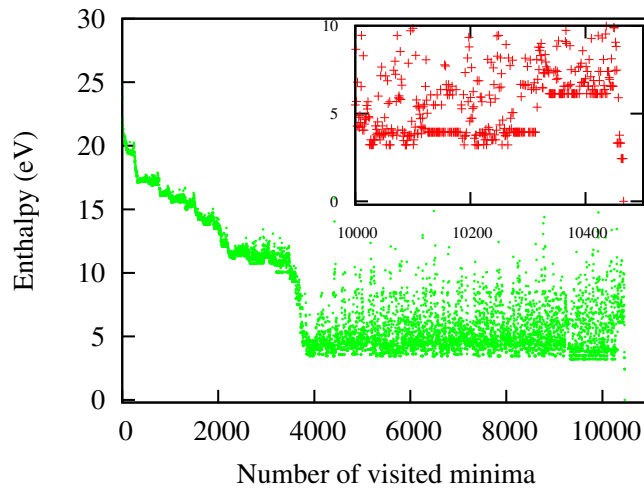


Figure 3.7: The enthalpies of the local minima visited during a MHM simulation of a Si_{64} supercell at zero pressure, starting from a random input configuration. The enthalpies were shifted such that the ground state enthalpy is zero. The inset shows clearly the crossing of the potential barrier before arriving at the ground state structure.

The LVPS can be further used to predict the correct system size when the number of atoms in the crystal basis is not known in advance.

Figure 3.7 shows a typical progress of a MHM run for a Si_{64} supercell at zero pressure. First, starting from a random structure, the enthalpy decreases as new parts of the enthalpy surface are explored. After visiting some 4000 local minima, the system is caught for some time in a deep funnel. This funnel corresponds exactly to the case discussed above and the perfect crystal could be completed applying the LVPS. However, after visiting slightly more than 10 200 minima a barrier is crossed and the system finally reaches the ground state structure.

The EDIP potential proved to be somewhat inaccurate when predicting the enthalpies of structures at a pressure of 16 GPa. Both the well-known β -tin structure [150, 151, 152] (Si-II) and the *Imma* structure [153] (Si-XI) were found to be metastable in EDIP. The simple hexagonal phase [152] (Si-VII) is not even a local minimum on the enthalpy surface and relaxes to the simple cubic structure. Instead, a structure with shifted layers of cubic elements where each atom is fourfold coordinated with a bond length $\approx 2.4 \text{ \AA}$ was predicted as the ground state with an enthalpy of -2.923 eV and a volume of 14.378 \AA^3 per atom, a structure not in the fitting database used for EDIP. Finding this unexpected crystalline ground state shows the predictive power of the MHM method for unknown structures. However, the novel structure was found to be unstable within DFT calculations. The second lowest crystalline structure was found to be the bct-5 structure [154] with an enthalpy of -2.865 eV and a volume of 15.264 \AA^3 per atom.

3.3.7 Volume constraints

Up to now external constraints were imposed in the form of isotropic pressure which is also the quantity that can be in general controlled under experimental conditions. However, in some cases one is interested in structures which exist at a specific cell volume. This is for example the case for porous phases in compounds with a dense ground state structure.

We employed the MHM on a Si_{46} supercell at zero pressure with volume constraints which was realized by introducing a harmonic energy term E_{vol} (second term in equation (3.30)) in addition to the standard EDIP potential energy:

$$E_{\text{tot}} = E_{\text{EDIP}} + k \cdot (\det(h) - \Omega_0)^2 \quad (3.30)$$

where k is a small scalar value and Ω_0 is the target volume. The additional gradient on the cell vectors is given by

$$\frac{\partial E_{\text{vol}}}{\partial h_{\alpha\beta}} = 2k \cdot (\det(h) - \Omega_0) \det(h) h_{\beta\alpha}^{-1} \quad (3.31)$$

The Si_{46} was chosen since it can form the unit cell of a type-I Si_{46} clathrate structure [156] (see Figure 3.8). Although clathrates have fourfold coordinated structures their overall

geometry differs significantly from the cubic diamond structure. Composed from polyhedral building blocks, a major part of the unit cells remains void, resulting in porous crystals. Therefore, the type-I Si_{46} clathrate within the EDIP potential has a large volume per atom ratio of 22.852 \AA^3 .

Starting from random input positions 20 MHM runs were started using the equilibrium volume of the type-I Si_{46} clathrate as the target Ω_0 and $k = 2.0 \text{ eV/\AA}^6$, each process visiting some 1.5 Mio. minima. Only one run was able to find the clathrate ground state unit cell after visiting roughly 150 000 minima. Nevertheless, finding the clathrate unit cell at all is an encouraging result since this particular system is a big challenge in global optimization for the following reasons. First, there is only one unit cell corresponding to the ground state and it consists of a huge basis of 46 atoms with a complex structure. Second, there are two main funnels that compete during the search for the ground state. On one hand, the system prefers to crystallize to the cubic diamond structure, but the void areas with the dangling bonds are energetically not favorable. On the other hand there is a tendency of forming spherical cage-structures in a porous crystal, but it is seldom possible to obtain tetrahedral bond angles. These are two fundamentally different structures and are separated by a very high potential barrier hard to overcome, hence starting from many different random input guesses is crucial for a successful run.

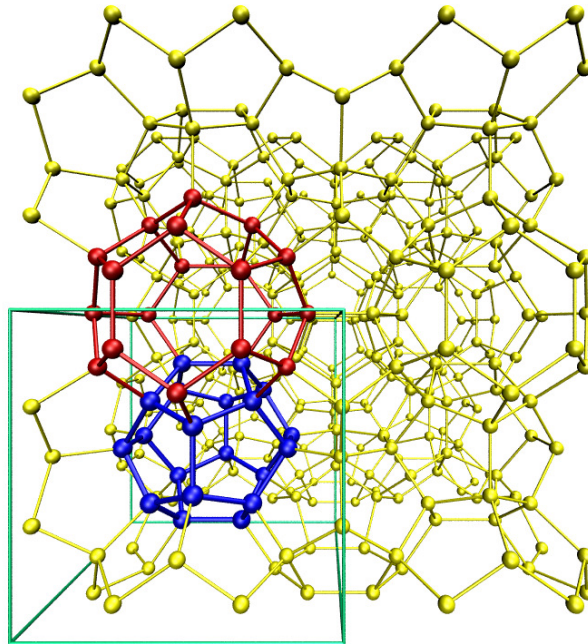


Figure 3.8: The type-I silicon clathrate is shown with the unit cell represented by the green box. Two types of cages are used to compose the structure, a small pentagonal dodecahedron (blue) and a larger hexagonal truncated trapezohedron (red)[155].

APPLICATIONS

We now present the results obtained on four different materials studied with the MHM for crystal structure prediction. This chapter is structured as follows.

First we apply the MHM to a well studied benchmark system, a Lennard-Jones potential which has been parametrized to model glassy materials. Global geometry optimization on such systems is especially challenging due to its many-funnel characteristic. The successful discovery of novel putative ground state structures presented in section 4.1 of this benchmark system clearly demonstrates the predictive power of the generalized MHM.

Next, we attack a longstanding debate on the crystal structure of high pressure carbon phases. Experimental evidences have been around for several decades which suggest the existence of a novel super-hard carbon phase. Graphite compressed at ambient conditions reveals unexpected changes in the optical transmittance, optical reflectivity, X-ray diffraction pattern and in the raman spectra in the range of 10 to 25 GPa. By performing extensive *ab initio* minima hopping simulations at high pressures we discovered two previously unreported carbon allotropes, *Z*- and *M10*-carbon. In a close collaboration with José A. Flores-Livas, who performed high pressure Raman experiments on graphite under the supervision of Alfonso San Miguel in Lyon, France, we present strong evidences for the presence of *Z*-carbon phase in samples of cold compressed graphite.

The third system under study is dedicated to hydrogen rich silicon compounds. Superconducting phases of metallic hydrogen with a high transition temperatures T_c have been predicted already in the late 1960's. Chemical pre-compression of hydrogen by incorporating heavier atoms into the crystal structure was recently proposed by Ashcroft to give similarly high T_c . We employed a recently developed silicon-hydrogen Lenosky tight-binding scheme together with the MHM to sample the enthalpy surface of disilane SiH_6 at high pressures. Thereby we identified two novel low-enthalpy phases of this compound, one of which was found to be the most stable in a wide pressure range. In a close

collaboration with José A. Flores-Livas we evaluated the electron-phonon interaction to estimate its superconducting transition temperature. Comparison with previous studies shows that the T_c of this phase is significantly lower than previous predictions, calling for a thorough unconstrained structural search in materials design.

Finally, we examine low temperature phases of LiAlH_4 . With its high hydrogen contents, it has been touted as a hydrogen storage material for applications in hydrogen fuel cells. Especially mobile vehicles call for novel materials to store hydrogen as an energy source for proton exchange membrane fuel cells, which have the advantage of clean combustion without exploiting fossil resources or producing green house gases. By performing minima hopping simulations we identified a novel class of LiAlH_4 phases which are significantly lower in energy than the previously predicted ground state structure of this compound. Synthesis of such phases would have profound implications on the stability and applicability of LiAlH_4 as a hydrogen storage material.

All structural searches were carried out by performing extensive minima hopping simulations on the energy or enthalpy surface modeled by the given approximations (Lennard-Jones potential, tight-binding and DFT). Multiple parallel minima hopping simulations (at least three) were carried out at a given stoichiometry, pressure and cell size. Their convergence were ensured by the discovery of the putative ground state by at least 66% of the simulations.

4.1 Structure of Binary Lennard-Jones Mixtures

In this section we present our results on a reinvestigation of much-studied BLJ mixtures at zero pressure which are widely accepted benchmark systems. Lately, these mixtures have been studied by Middleton *et al.* [157]. They found that ordered crystalline phases are energetically favored, contrary to earlier results indicating a preference for glassy, amorphous structures. The putative ground state structures found in this previous work are available on the Cambridge Cluster Database (CCD) [158].

4.1.1 Parametrization of the Lennard-Jones potential

We studied all supercells available on the CCD, with 60, 256 and 320 atoms consisting of 80% type A and 20% type B components. In our calculations we used a small modification of the well-known Lennard-Jones potential [159] (also used in Ref. [157]), truncated and shifted using a quadratic function such that both the energy and the first derivative are continuous at the cutoff distance [160]. The functional form of the pair potential is given in equation (4.1) where the indexes α and β denote the atom types A and B, $r_{\alpha\beta}$ is the interatomic distance, $\epsilon_{\alpha\beta}$ is the potential well depth and $\sigma_{\alpha\beta}$ corresponds to the distance

where the potential vanishes (not to be confused with the strain and stress tensors). The potential is zero when the radial distance is larger than the cutoff $r_{\alpha,\beta}^{cut}$. All parameters are identical to the ones used in Ref. [157], namely: $\sigma_{AA} = 1.00$, $\sigma_{AB} = 0.80$, $\sigma_{BB} = 0.88$, $\epsilon_{AA} = 1.00$, $\epsilon_{AB} = 1.50$, $\epsilon_{BB} = 0.50$, and a cutoff radius of $r_{\alpha,\beta}^{cut} = 2.5\sigma_{\alpha,\beta}$. All energies and enthalpies are given in units of ϵ_{AA} .

$$\phi_{\alpha\beta} = 4\epsilon_{\alpha\beta} \left\{ \left[\left(\frac{\sigma_{\alpha\beta}}{r_{\alpha\beta}} \right)^{12} - \left(\frac{\sigma_{\alpha\beta}}{r_{\alpha\beta}} \right)^6 \right] + \left[6 \left(\frac{\sigma_{\alpha\beta}}{r_{\alpha,\beta}^{cut}} \right)^{12} - 3 \left(\frac{\sigma_{\alpha\beta}}{r_{\alpha,\beta}^{cut}} \right)^6 \right] \left(\frac{r_{\alpha\beta}}{r_{\alpha,\beta}^{cut}} \right)^2 - 7 \left(\frac{\sigma_{\alpha\beta}}{r_{\alpha,\beta}^{cut}} \right)^{12} + 4 \left(\frac{\sigma_{\alpha\beta}}{r_{\alpha,\beta}^{cut}} \right)^6 \right\} \quad (4.1)$$

Finding low enthalpy structures is a challenging task for these specific mixtures due to the following reasons. First, the parametrization of these Lennard-Jones mixtures have been explicitly used to model glassy materials and are therefore known not to crystallize easily (see references in Ref. [157]). Furthermore, the simulation cells are very large (especially the cells containing 256 and 320 atoms). Therefore, starting from random configurations as initial guess has proven to be a bad approach, since random structures are very likely to form amorphous structures which take a long time to form crystalline structures even if they are lower in enthalpy.

Inspired by the methods to handle large crystal structures proposed by Lyakhov *et al.* [113] we used a modified approach of unit cell splitting to handle the 256 and 320 atoms cells. The MHM is a powerful tool not only to predict ground state structures, but also to find low lying excited configurations. To handle large cells containing many atoms we simply split the simulation cell into smaller sub-cells. Then, starting from random configurations, we run short MHM simulations on these sub-cells to sample the low enthalpy regions and obtain a set of low enthalpy structures. By spanning the large simulation cells with these sub-cells we get structures which now serve as initial guesses for several parallel MHM runs on the large cell. However, it is essential to choose sub-cells which are not too similar in structure since they might be members of the same funnel. In our investigation we used up to 20 parallel MHM runs with a search length of visiting some 100 000 minima per run.

4.1.2 Putative ground state structures

For the 60 atom cell we found several thousand structures with enthalpies lower than $-7.08 \epsilon_{AA}$ per atom, which is the lowest energy for this system in Ref. [157]. The putative ground state was found to have an enthalpy of $-7.49 \epsilon_{AA}$ per atom. In fact, this value is already lower than any other enthalpy of the larger super-cells which were investigated by Middleton *et al.* The super-cell of the ground state structure is shown in Figure 4.1 (a). It consists of two different regions similar to a phase separation. The lower section consists purely of type A atoms in a $4H$ close packed structure (ABCB stacking). The upper half of the cell consists of a mixed phase where type B atoms are embedded in cages consisting of 7 type A atoms with a C_{2v} symmetry, a monocapped trigonal prism. A detailed illustration of this behavior is shown in Figure 4.2 (a).

The 256 atom cell turned out to be the most difficult system to optimize since 80% of 256 does not yield an integer number. Hence we used a system containing 205 atoms of type A and 51 of type B, identical to the system used by Middleton *et al.* The reference enthalpy on the CCD is $-7.20 \epsilon_{AA}$ per atom. We managed to find structures as low as $-7.43 \epsilon_{AA}$ per atom, which is not as good as our results for both other cells. This can be ascribed to the fact that it is difficult to find a super-cell that can hold a crystalline structure composed of the odd numbers of atoms, 205 and 51, respectively. Similar to the 60 atom cell the type A atoms are $4H$ close packed and the type B atoms are concentrated in a region. However, three of the type B atoms are mixed seemingly randomly among the type A atoms (see Figure 4.1 (b)). Furthermore, one third of the type B atoms are centered in monocapped trigonal prisms consisting of 7 type A atoms, the rest in bicapped trigonal

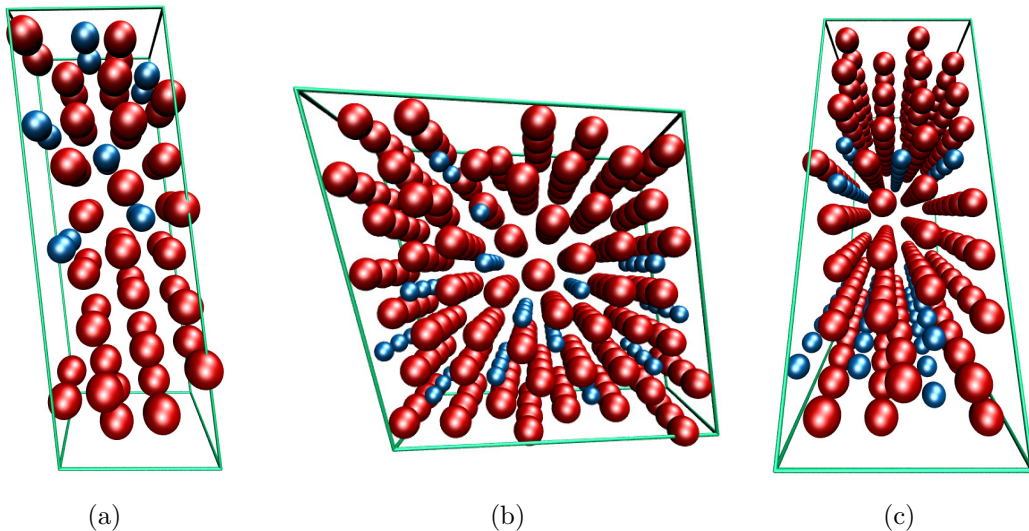


Figure 4.1: Predicted structures for the Lennard-Jones mixtures with 60 (a), 256 (b) and 320 (c) atoms. Type A atoms are denoted by red (large) spheres, type B atoms are blue (small).

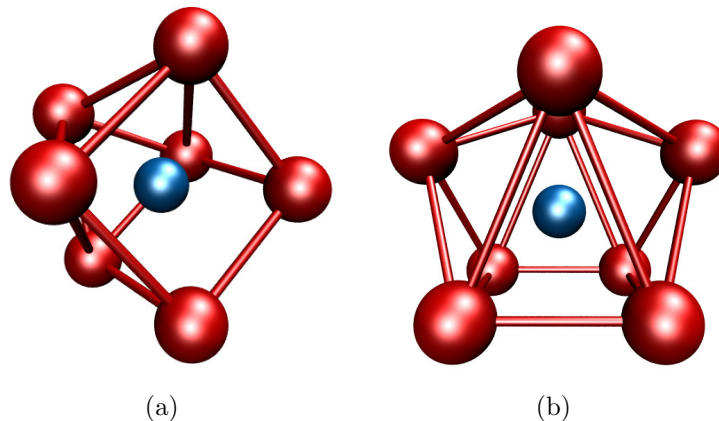


Figure 4.2: The detailed structure of the embedded type B atoms. Subfigure (a) shows 7 type A atoms which form a monocapped trigonal prism [161]. The symmetry group of this isolated molecule is C_{2v} . Subfigure (b) shows the type B atom centered in a bicapped trigonal prism made of 8 type A atoms.

prisms consisting of 8 type A atoms as illustrated in detail in Figure 4.2 (b).

For the 320 atom cell we found the ground state structure to have an enthalpy of $-7.50 \epsilon_{AA}$ per atom compared to $-7.33 \epsilon_{AA}$ per atom on the CCD. Again, the cell mainly consists of regions with type A atoms in a $4H$ close packed structure and regions containing type B atoms (Figure 4.1 (c)). The type B atoms are centered in bicapped trigonal prisms consisting of 8 type B atoms. As expected, the cell containing 320 atoms was found to have the lowest enthalpy structures among all three studied systems.

4.1.3 Summary

In summary, we were able to find new putative ground state structures for all BLJ systems available on the CCD using the MHM. We have found that for large cells containing many atoms the search for ground state structures becomes very difficult and that random input structures are not ideal to seed MHM runs. This problem has already been reported by Lyakhov *et al.* [113] when using genetic algorithms for crystal structure prediction. Using the modified cell splitting method and the predictive power of the MHM to sample structures close to the ground state the efficiency of the crystal structure prediction can be significantly increased.

4.2 Crystal Structure of Cold Compressed Graphite

Thanks to the flexibility to form sp , sp^2 and sp^3 bonds, carbon is one of the most versatile chemical elements. At ambient pressure, it is usually found as graphite (the most stable structure) or as diamond, but the richness of its phase diagram does not end there. In fact, many other structures have been proposed during the past years, especially since experimental data suggested the existence of a super hard phase of carbon. Evidences for a structural phase transition in compressed graphite to this unknown phase of carbon have been reported in numerous experiments [162, 163, 164, 165, 166, 167, 168]. In fact, in the range of 10 to 25 GPa one observes an increase of the resistivity [162] and of the optical transmittance [163, 164], a marked decrease of the optical reflectivity [165], changes in near k -edge spectra [168] and in X-ray diffraction (XRD) patterns [166, 167, 168]. Several hypothetical structures have been proposed to explain these features, such as hybrid sp^2 - sp^3 diamond-graphite structures [169], M -carbon [118], bct- C_4 -carbon [170] and W -carbon [171]. However, none of these structures is able to match all experimental data in an unambiguous and fully satisfactory manner.

4.2.1 Structural identification and formation mechanism

A common way to search for new crystal structures is to perform a systematic survey of the enthalpy surface using some sophisticated structure prediction method (for discussion on such methods see section 3.2 or Ref. [172]). Here we use the MHM for crystal structure prediction. It was coupled to the all-electron projector-augmented wave method as implemented in the ABINIT code [173, 174], and the relaxations were performed by FIRE [60]. The local density approximation was employed based on its good description of graphite. However, the enthalpy ordering was reconfirmed within the generalized gradient approximation using two different functionals (Perdew-Burke-Erzerhof (PBE) [39] and PBEsol [175]). The most promising candidate structures were then re-relaxed using norm conserving Hartwigsen-Goedecker-Hutter (HGH) pseudopotentials [176]. Carefully converged Monkhorst-Pack k -point meshes [177] were used together with a plane wave cut-off energy of 2100 eV. All calculations were performed at zero Kelvin, and we neglected the contribution of the zero-point motion of the nuclei to the enthalpy.

The MHM was employed using simulation cells with 4 and 8 carbon atoms at a constant pressure of 15 GPa. A plethora of different carbon structures were identified, a small selection of which is presented in Figure 4.3. We found, in addition to previously proposed structures of cold compressed graphite, two other low-enthalpy carbon phases that we call Z -carbon and $M10$ -carbon, respectively.

Z -carbon has $Cmmm$ symmetry (see Figure 4.4(a)) and, like diamond, is composed of sp^3 bonds. The conventional unit cell has 16 atoms with cell parameters at 0 GPa of $a = 8.668 \text{ \AA}$, $b = 4.207 \text{ \AA}$, and $c = 2.486 \text{ \AA}$, yielding a cell volume of $V_0 = 90.7 \text{ \AA}^3$. The two

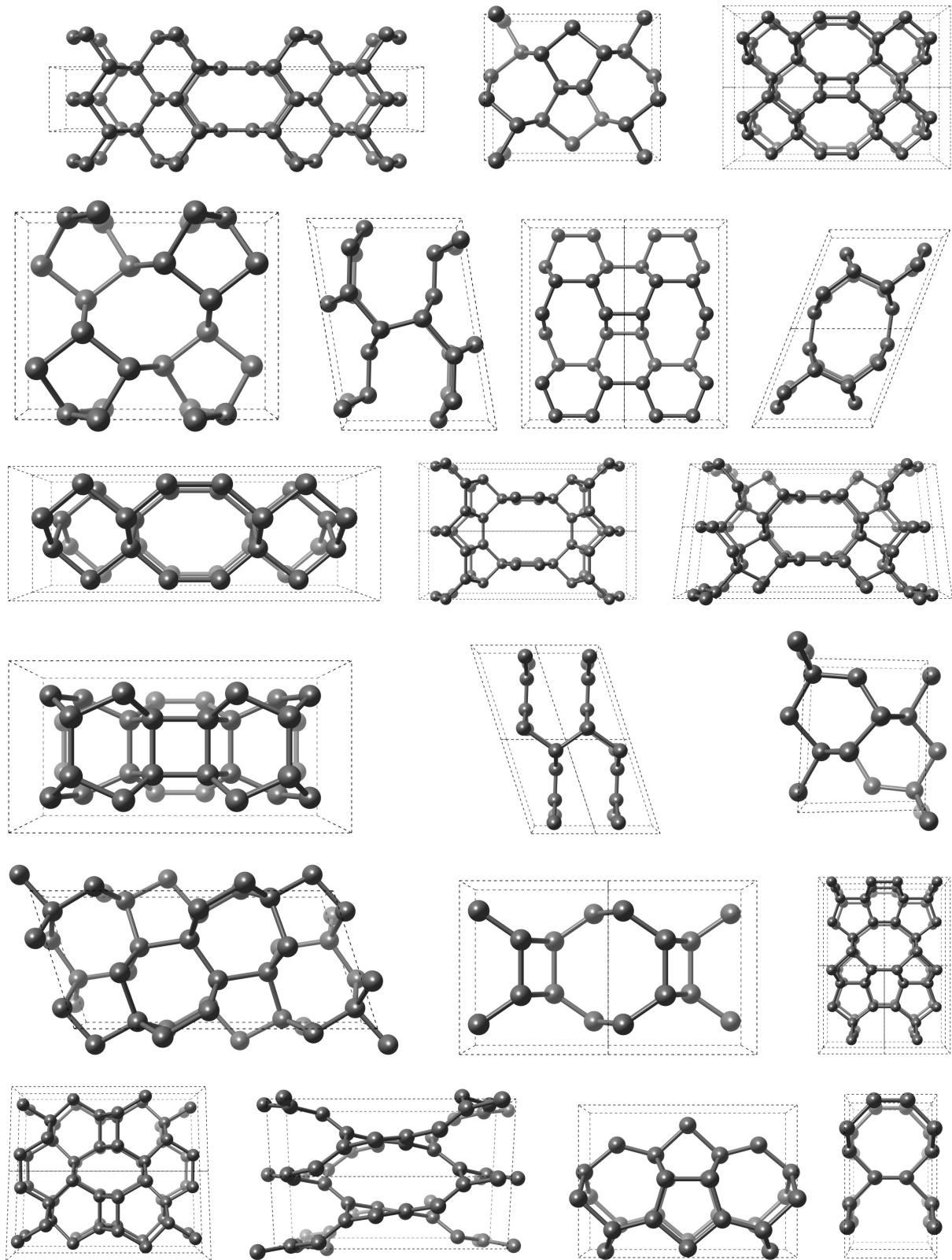


Figure 4.3: Structural variety in high pressure phases of carbon

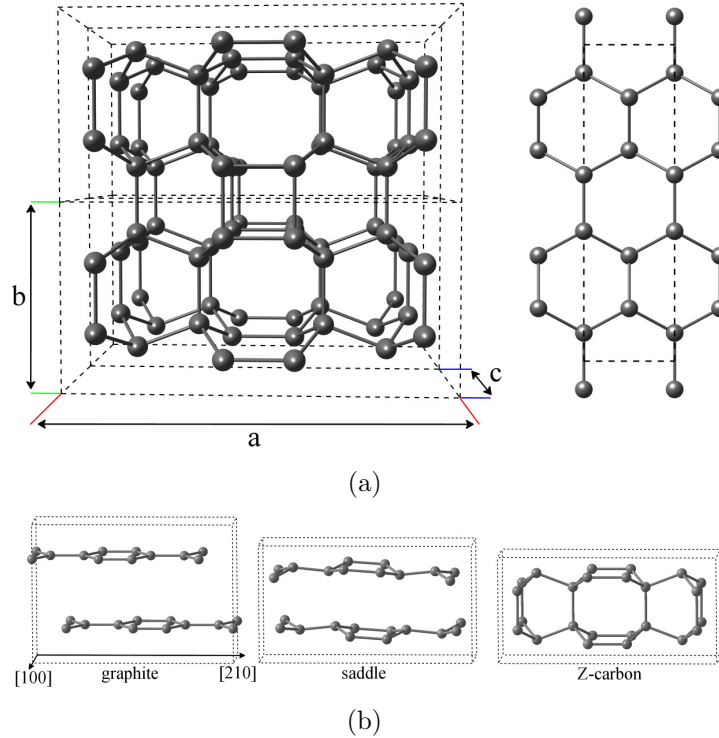


Figure 4.4: (a) Structure of *Z*-carbon viewed from two different angles revealing planar four-membered and non-planar eight-membered rings forming chains along the *b*-direction and channels in the *c*-direction. The graphene sheets are in the *a*-*c* plane. (b) Proposed transition pathway from graphite to *Z*-carbon.

inequivalent carbon atoms occupy the $8p$ and $8q$ crystallographic sites with coordinates $(\frac{1}{3}, y, 0)$ and $(0.089, y, \frac{1}{2})$, where $y = 0.315$. The structure contains four-, six- and eight-membered rings, where planar four-membered rings and non-planar eight-membered rings join together buckled graphene sheets. This structure can be interpreted as a combination of hexagonal diamond and *bct*- C_4 -carbon [178].

In contrast to other structure prediction methods like evolutionary algorithms or random search, the efficient escape moves in the MHM are based on fundamental physical processes. Therefore, minima found consecutively during a MHM simulation are usually connected through low enthalpy barriers. Since we have observed escape moves to and from *Z*-carbon to occur exclusively from and to graphite, we expect this transition to be the most probable. In Figure 4.4(b) we show a possible transition pathway from graphite to *Z*-carbon. This process is a combination of sliding and buckling of the graphene sheets. The naturally staggered, i.e. *AB* stacked, graphene sheets slide along the [210] direction to an aligned *AA* stacking while the inter-layer distance decreases, and the aligned graphene sheets deform to create an alternating armchair-zigzag buckling.

The second structure is a monoclinic phase with $P2/m$ symmetry that we call *M10*-

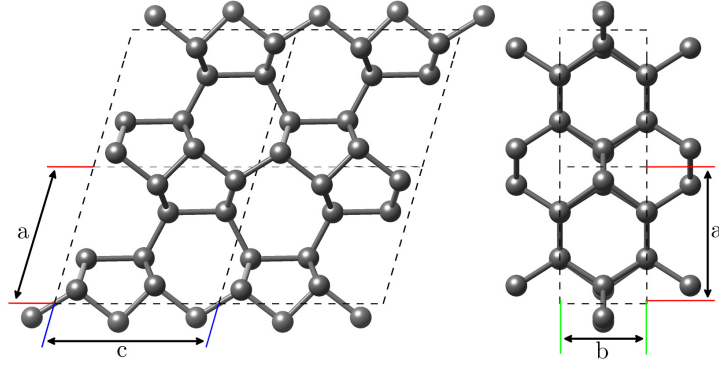


Figure 4.5: The structure of *M10*-carbon from two different angles. The left panel shows the 5- and 7-membered rings, while the right panel reveals the 6-membered rings.

carbon. It also consists solely of sp^3 bonds and contains 8 atoms per cell. At ambient pressure, the unit cell parameters are given by $a = 4.080 \text{ \AA}$, $b = 2.498 \text{ \AA}$, $c = 4.728 \text{ \AA}$, $\alpha = \gamma = 90^\circ$ and $\beta = 73.96^\circ$. Two carbon atoms each occupy the crystallographic $2n$ sites at $(-0.1, y_1, -0.113)$ and $(-0.132, y_1, 0.421)$, and the $2m$ sites at $(-1/3, y_2, -0.466)$ and $(-0.325, y_2, -0.117)$, where $y_1 = 1/2$ and $y_2 = 0$. The overall structure is closely related to *M*-carbon, also consisting of 5- and 7-membered rings along the b -axis, while 6-membered rings are formed along the c -axis. In contrast to *M*-carbon, the 5-rings share the long edge, whereas in *M10*-carbon they share the short edge. The structure is illustrated in Figure 4.5.

4.2.2 Energetic, dynamical and electronic properties

In order to investigate the relative stability of *Z*- and *M10*-carbon, the calculated enthalpy difference with respect to graphite of several allotropes are compared in Figure 4.6 as a function of pressure. *Z*-carbon has the lowest enthalpy among all proposed cold-compressed graphite phases, becoming more stable than graphite at 9.9 GPa (around 2.5 GPa below *W*-carbon). *M10*-carbon becomes enthalpically favorable over graphite above a pressure of 14.4 GPa. As expected from the structural similarities with *M*-carbon, both *M10*- and *M*-carbon are very close in enthalpy throughout the whole pressure range.

We further investigated the dynamical lattice stability of these phases by computing the phonon dispersion in the whole Brillouin zone. We used linear-response theory in the framework of density functional perturbation theory [179, 180] with the ABINIT code. A proper convergence was ensured with a $12 \times 12 \times 12$ k -point sampling, a $4 \times 4 \times 4$ q -point mesh, and a cut-off energy of 800 eV. All phonon modes were real confirming the dynamical stability of the structures. Furthermore, from a fit of the Murnaghan equation we obtained a bulk modulus of $B_0 = 441.5 \text{ GPa}$, and using the method proposed by Gao *et al.* [181] we calculated a Vicker's hardness of $H_v = 95.4 \text{ GPa}$ for *Z*-carbon. *M10*-carbon has a slightly

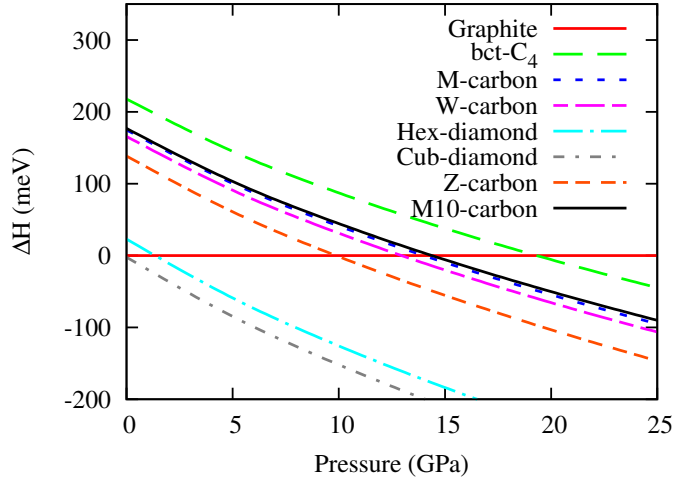


Figure 4.6: Calculated enthalpy difference per atom with respect to graphite of several carbon allotropes as a function of pressure. Graphite is the horizontal line at zero. *Z*-carbon becomes more stable than graphite at around 10 GPa, while *M10*-carbon crosses the graphite line at 14.4 GPa.

lower bulk modulus of $B_0 = 423.7$ GPa, and the Vicker's hardness is $H_v = 93.5$ GPa. Both bulk modulus and hardness of *Z*- and *M10*-carbon are extremely high and very close to the values for diamond ($B_0^{\text{diamond}} = 463.0$ GPa and $H_v^{\text{diamond}} = 97.8$ GPa), which is compatible with the observed ring cracks in diamond anvil cells [168]. In Table 4.1 we compare the structural properties of *Z*- and *M10*-carbon with other carbon allotropes.

To investigate the energy gap of *Z*-carbon we used the perturbative many-body GW technique starting from the local density approximation [182]. These calculations reveal that *Z*-carbon is an indirect band-gap material with a gap of around 4.7 eV. Therefore, this material is expected to be optically transparent in agreement with experiments [163, 164]. Similarly, *M10*-carbon was found to be a wide band-gap semiconductor with an indirect PBE gap of 4.4 eV at 0 GPa.

4.2.3 Experimental evidences

We have gathered several experimental observations supporting our interpretation that *Z*-carbon is present in cold compressed graphite samples. The first comes from the XRD experiment of Ref. [168]. In Figure 4.7 we can see that the broadening of the XRD-spectra at high pressure can be explained by the coexistence of graphite and *Z*-carbon. However, the experimental curve can also be explained to some extent by the other proposed carbon allotropes [118, 170, 171] including *M10*-carbon so that this experiment alone is not conclusive.

Other signatures for *Z*-carbon can be gathered from our measurements of Raman spec-

Table 4.1: Calculated and experimental data (where available) of the bulk moduli B_0 (in GPa), Vickers Hardness H_v (in GPa) and volumes per atom V_0 (in Å/atom) at 0 GPa for bct-C₄, M -, W -, Z -, $M10$ -carbon and diamond.

Structure	Method	B_0 (GPa)	H_v (GPa)	V_0 (Å)
bct-C ₄	this work	428.2	93.5	5.82
	LDA [171]	433.7		5.83
M -carbon	this work	428.4	93.9	5.77
	LDA [118]	431.2	83.1	5.78
W -carbon	this work	427.5	94.2	5.75
	LDA [171]	444.5		5.76
Cub-Diamond	this work	463.0	97.8	5.51
	LDA [171]	466.3		5.52
	Expt.	446 ^a	60-120 ^b	5.67 ^a
Z -carbon	LDA [20]	441.5	95.4	5.66
$M10$ -carbon	this work	423.7	93.5	5.79

^a Reference [183]

^b Reference [184]

troscopy under pressure. These experiments were carried out at 300 K using the 514.5 nm line excitation of an Ar⁺ laser, and a Jobin-Yvon HR-800 Labram spectrometer with double-notch filtering with resolution better than 2 cm⁻¹. In the high pressure Raman measurements, we used a diamond anvil cell to apply pressure on two different samples (single crystals of graphite and highly oriented pyrolytic graphite), inside a 120 micron hole drilled in an iconel gasket. Argon and paraffin were used as pressure media. The pressure was determined by the ruby luminescence of a small chip (< 30 microns). The laser was focused down to 3 microns with a power of about 20 mW on the sample.

The principal Raman active mode of graphite is the G-band at 1579 cm⁻¹ (at 0 GPa) which originates from the sp^2 carbon atoms vibrating in-plane with E_{2g} symmetry. The effect of hydrostatic pressure on the linewidth of the G-band is shown in Figure 4.9(a). The linewidth remains nearly constant until around 9–10 GPa. Above this value, the linewidth begins to broaden rapidly, in agreement with previous results of Hanfland *et al.* [164]. (A similar broadening has also been reported for turbostratic graphite-like BC₄ under pressure [185].) This behavior is a sign of a structural transformation at this pressure, and can be explained by important changes in the Raman cross section caused by interlayer coupling and the formation of sp^3 bonds. As seen in Figure 4.6, Z -carbon becomes enthalpically favored with respect to graphite at around 10 GPa, whereas all other proposed structures cross the graphite line at significantly higher pressures.

There is a further indications of the existence of Z -carbon, that can be found in the Raman spectrum of graphite under hydrostatic pressure, shown in Figure 4.9(b) for the

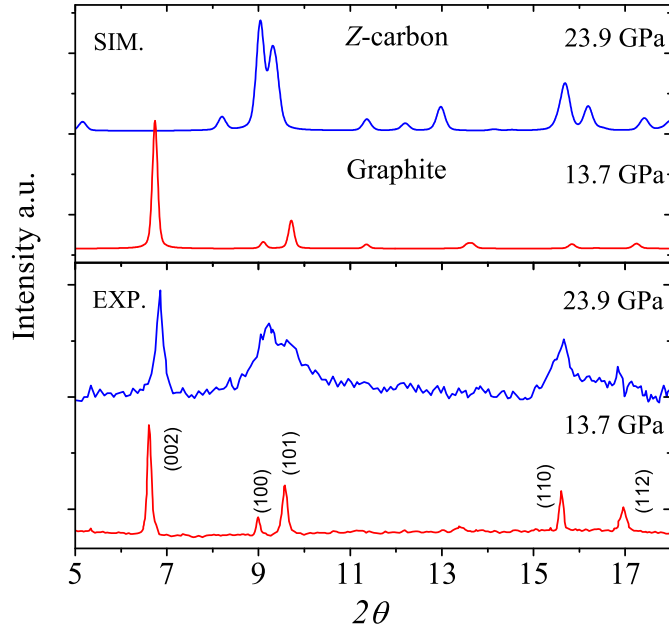


Figure 4.7: Experimental XRD for cold compressed graphite at two different pressures from Ref. [168] and simulated XRD pattern for *Z*-carbon (at 23.9 GPa) and graphite (at 13.7 GPa). The main characteristics of the proposed carbon are perfectly in agreement with the experimentally observed changes.

energy range below the 1st order Raman peak of diamond (1332 cm^{-1} at 0 GPa) [183]. Neither graphite nor cubic-diamond have Raman active peaks in the selected energy region [186], however we can observe that a clear peak appears at 1082 cm^{-1} for pressures higher than 9.8 GPa. This peak can be explained by neither bct-C4 carbon, *M*-carbon, nor by the pressure medium (argon). Experiments at ambient pressure have shown that a raman peak at 1090 cm^{-1} can be observed in samples of nanocrystalline diamond [187]. Furthermore, the presence of nanodiamond in our sample might be enthalpically possible. However, since nanodiamond synthesis has been shown to be stable in high pressure experiments [188] and the observed G-band broadening is fully reversible under pressure unload this possibility can be ruled out. Therefore, the only structures that have Raman active modes compatible with this experimental results are *Z*-carbon and *W*-carbon. For *Z*-carbon the frequencies are 1096.5 cm^{-1} at 10 GPa and 1110 cm^{-1} at 15 GPa. Incidentally, *Z*-carbon also has a Raman active A_g mode at 1348.5 cm^{-1} at 0 GPa (theoretical value). This appears as a signature of planar four-membered rings that overlaps with the so-called defect D-band of graphite at around 1345.5 cm^{-1} at 0 GPa (experimental value).

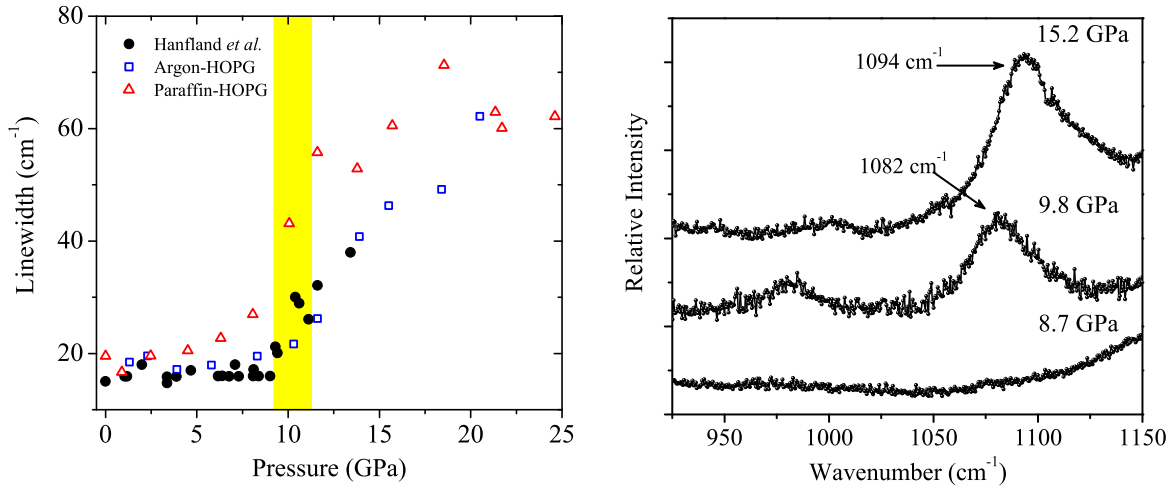


Figure 4.9: (a) Experimental linewidth of the G-band of graphite under pressure. The linewidth stays nearly constant until pressures of the order of 9 – 10 GPa, above which the linewidth begins to broaden rapidly. This is a strong evidence for a structural transition in graphite. Experiments were conducted using highly oriented pyrohillitic graphite (HOPG) and argon (squares) or paraffin oil (triangles) as pressure transmitting media. Note that the G-band broadening is fully reversible under pressure unload. The unload points are however not included for clarity. The black dots are taken from Ref. [164]. (b) Experimental Raman spectra of graphite under pressure. The peak around 1082 cm^{-1} appearing at around 10 GPa and its evolution can be explained by either *Z*-carbon, *W*-carbon or nanocrystalline diamond.

4.2.4 Summary

In conclusion, we identified two novel allotropic structure of carbon, *Z*-carbon, that becomes more stable than graphite above 10 GPa, and *M10*-carbon which has a transition pressure of 14.4 GPa. From all known carbon allotropes, only cubic and hexagonal diamond have lower enthalpy at high pressures than *Z*-carbon, which makes it the most promising candidate among previously proposed structures of cold compressed graphite. Both *Z*-carbon and *M10*-carbon phases are as hard as diamond, and transparent in the optical region. Moreover, several experimental data are consistent with the presence of *Z*-carbon in samples of cold compressed graphite: first, the features of the X-ray diffraction spectra of graphite under pressure exhibit a broadening that matches the main peaks of *Z*-carbon. Second, the principal Raman signal of graphite, the G-band mode, suffers an abrupt increase of the linewidth above 9-10 GPa — the pressure range where *Z*-carbon becomes more stable than graphite. Third, a new peak at 1082 cm^{-1} appears in the Raman spectrum of graphite at around 10 GPa, at the frequency of a Raman active mode of *Z*-carbon. However, further comparative studies on the formation barriers of all proposed candidate structures might be needed for a conclusive determination of the structure of

cold compressed graphite.

4.3 High pressure structures of disilane and their superconducting properties

Superconductivity in elemental hydrogen was predicted by Ashcroft [189] already in 1968. More recently, and with the use of novel theoretical techniques [190, 191], the calculated T_c was estimated to be as high as 240 K at pressures of around 450 GPa in molecular hydrogen [192]. Furthermore, very recent studies of atomic hydrogen found a transition temperature of 356 K at 500 GPa [193], and T_c s of above 600 K at pressures beyond 1TPa [193, 194]. However, the synthesis of metallic hydrogen has been found to be experimentally challenging, and even at extremely high pressures (below 320 GPa) metallization has not yet been observed [195]. This is in agreement with theoretical calculations, that predict the metallic transition above 400 GPa [196] — a pressure beyond the reach of current experimental capabilities.

To circumvent this problem, it was recently suggested that metallization pressures could be achieved in hydrogen rich materials where the hydrogen is chemically “pre-compressed” [197]. Several investigations of such compounds have appeared in the literature, primarily focusing on group IV-hydrides. Calculations on phases of highly compressed silane [139, 198, 199, 200, 201, 119], germane [115] and stannane [202, 121] have shown the possibility of metallic phases with high T_c at moderate pressures. From the experimental point of view, silane SiH_4 has been reported to crystallize and attain metallicity above 50–60 GPa [203, 204] with a superconducting behavior. However, more recent studies ascribe the observed metallicity to the formation of metal hydrides [205], and metallization of silane was found not to occur at least below 130 GPa [206].

Another hydrogen rich compound of the same family is disilane Si_2H_6 . This compound has attracted attention as a hydrogen rich material due to its experimental availability. Moreover, in a recent theoretical study, Jin *et al.* [207] performed random searches in order to find stable structures of disilane. They reported three different structures covering a pressure range from 50 to 400 GPa. Crystallization of disilane into a metallic phase with a $P\bar{1}$ lattice was predicted to occur at 135 GPa. The T_c of this phase was predicted to be 64.6 K at 175 GPa, and 80.1 K at 200 GPa. Beyond 275 GPa, the lowest enthalpy phase was found to be a cubic $Pm\bar{3}m$ structure that reaches the remarkable superconducting transition temperature of $T_c = 139$ K at 275 GPa, a T_c much higher than any other predicted transition temperature of group IV-hydrides. Unfortunately, these results have not been experimentally confirmed.

4.3.1 Screening high-pressure phases with Lenosky tight-binding

The disilane system under pressure was investigated by using the MHM for the prediction of low enthalpy structures. We performed simulations for cells containing 1, 2, and 3

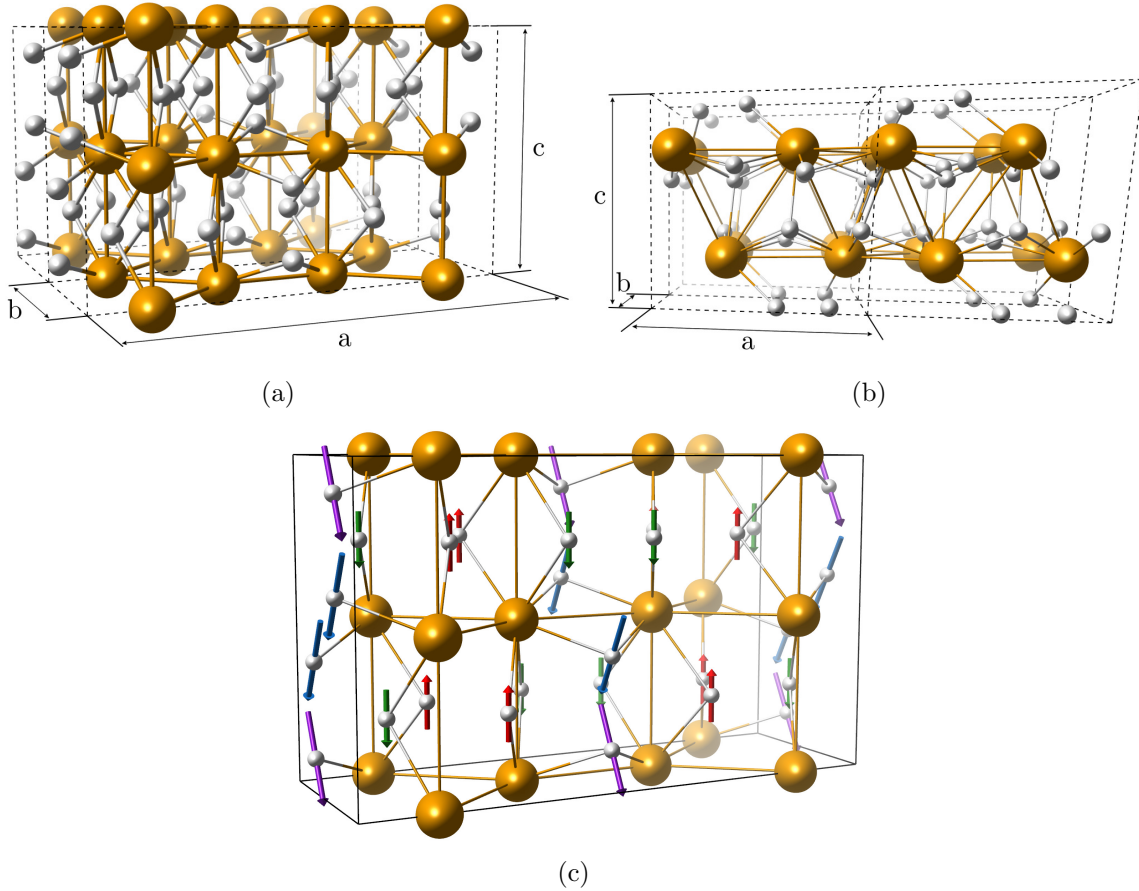


Figure 4.10: The crystal structures of (a) the $Cmc2_1$ phase at 200 GPa, and (b) the $P-1$ phase at 300 GPa. The eigendisplacements which lead from the $Cmc2_1$ structure to the $Cmc2_1$ structure are visualized by arrows in panel (c).

formula units of disilane Si_2H_6 under several different pressures between 40–400 GPa. The initial sampling of the enthalpy surface was carried out employing the MHM together with Lenosky’s tight-binding scheme [50], extended to include hydrogen. The most promising candidate structures found during the initial sampling were further studied [173, 208] at the DFT level using the PBE exchange-correlation functional [39] and norm-conserving HGH-pseudopotentials [176]. The plane-wave cut-off energy was set to 1400 eV, and Monkhorst-Pack k -point meshes [177] with grid spacing denser than $2\pi \times 0.025 \text{ \AA}$ were used, resulting in total energies convergence to better than 1 meV/atom. Finally, in order to confirm that the tight-binding scheme was able to sufficiently sample the enthalpy surfaces, we performed MHM simulations for selected pressures of 100 GPa, 200 GPa, 280 GPa, and 320 GPa at the DFT level.

In Figure 4.11 the enthalpy of the different phases found in our MHM simulations are shown with respect to decomposition towards elemental silicon and hydrogen. At pres-

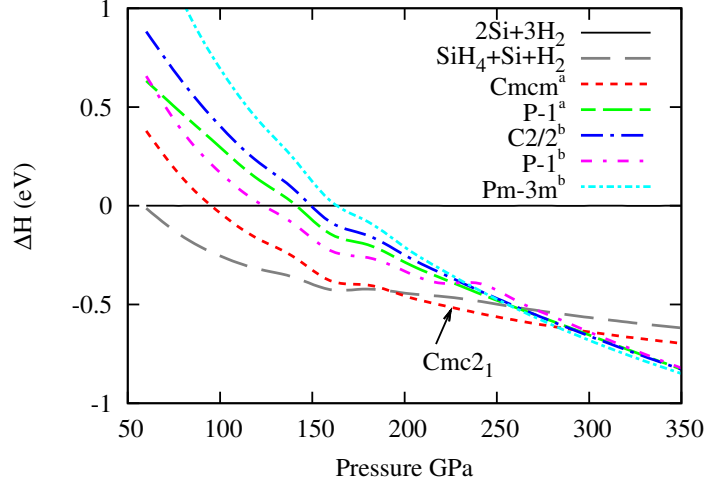


Figure 4.11: Enthalpy per formula unit of disilane as a function of pressure with respect to elements in their solid form $2\text{Si}(s) + 3\text{H}_2(s)$. The decomposition enthalpies were computed from the predicted structures of hydrogen ($P6_3/m$, $C2/c$) [209], high pressure phases of silicon ($P6/mmm$, $P6_3/mmc$, $Fm-3m$) [152, 210] and silane ($Fdd2$, $I4_1/a$, $Pbcn$) [139, 119]. The disilane structures with superscripts ^a and ^b are from this work and from Ref. [207], respectively. The dynamical instability towards the $Cmc2_1$ phase is indicated by the arrow.

ures above 280 GPa, the $Pm-3m$ phase is favored, competing with several other structures reported by Jin *et al.* [207]. In addition to the structures reported in Ref. [207] our simulations revealed another low-lying phase with $P-1$ symmetry (Figure 4.10(b)). However, all these structures lie in a very small enthalpy range which is within our numerical precision. In fact, taking into account the zero-point vibrational energies might easily change the energy ordering, and in general one can expect that at a finite temperature the competing low-enthalpy phases will be present as an admixture.

As seen also in Figure 4.11, crystalline disilane is enthalpically unstable towards decomposition to elemental silicon and hydrogen below 95 GPa. A decomposition to silane SiH_4 together with elemental silicon and hydrogen is enthalpically possible up to pressures of 190 GPa. This compositional instability could pose challenges en route to synthesis of crystalline disilane, depending on barrier heights and on the dynamics of the decomposition.

Yet another low-enthalpy metallic phase of disilane was found during our MHM simulations (see Figure 4.10(a)). It belongs to the $Cmcm$ space group, and is the lowest enthalpy structure up to 280 GPa. We would like to stress that the enthalpy difference between the $Cmcm$ phase and the previously proposed $P-1$ phase close to 200 GPa are relatively large, so that a change in the enthalpy ordering due to the zero point vibrational energy is very unlikely. At 200 GPa, its conventional cell parameters are $a = 7.965 \text{ \AA}$, $b = 2.705 \text{ \AA}$, and $c = 4.728 \text{ \AA}$, with one silicon atom occupying the $8e$ crystallographic site

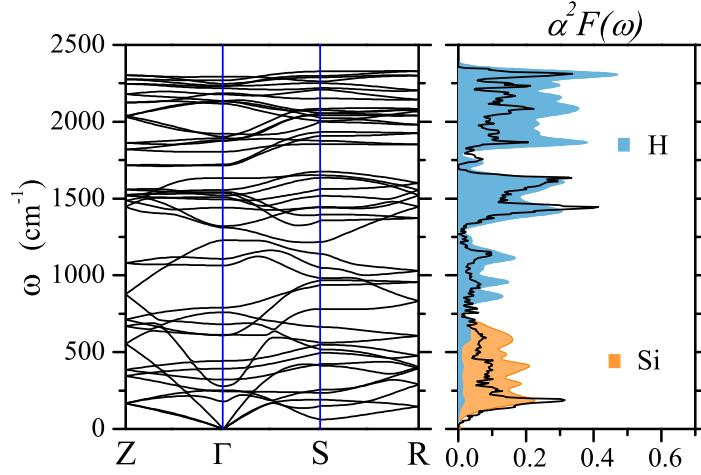


Figure 4.12: Left panel: Phonon band dispersion of the $Cmcm$ structure at 200 GPa. Right panel: Calculated Eliashberg spectral function $\alpha^2F(\omega)$ (solid line) and phonon partial density of states (Yellow: silicon, Blue: hydrogen).

at $(0.141, 0, 0)$ and three hydrogen atoms occupying $8g$, $8g$ and $8f$ sites at coordinates $(0.293, 0.173, 0.250)$, $(0.086, 0.302, 0.250)$ and $(0, 0.311, 0.895)$, respectively. The hydrogen atoms are embedded into a framework of five-fold coordinated silicon atoms. The average silicon-silicon bond length is 2.28 \AA , and each silicon atom is surrounded by six hydrogen atoms at a mean distance of 1.52 \AA .

4.3.2 Superconductivity and dynamical stability of the $Cmcm$ phase

We further characterized the $Cmcm$ structure by performing calculations of the phonon-spectrum, the electron-phonon coupling and the superconducting transition temperature T_c . The phonon spectrum and the electron-phonon matrix elements were obtained from density-functional perturbation theory [179, 180]. The spectral function $\alpha^2F(\omega)$ was integrated over the Fermi surface by applying the tetrahedron technique. Convergence of the above quantities was ensured by a $16 \times 16 \times 16$ Monkhorst-Pack k -point sampling, and a $4 \times 4 \times 4$ q -point sampling for the phonon wave-vectors. The above settings result in T_c s converged to less than 1 K. The phonon dispersion was obtained by Fourier interpolating the computed dynamical matrices.

The phonon band dispersion of the $Cmcm$ phase at 200 GPa can be seen in the left panel of Figure 4.12, while the partial phonon density of states is shown in the right panel. As expected, the low frequencies ($<700 \text{ cm}^{-1}$) are dominated by the vibrations of the silicon framework whereas the high end of the spectrum extending up to 2300 cm^{-1} is solely

Table 4.2: Superconducting properties of the $Cmcm$ phase at different pressures. The transition temperatures were calculated using Allen-Dynes modified McMillan’s formula. (see appendix D.2 for details)

Pressure	λ	Ω_{log}	T_c	
			$\mu^* = 0.1$	$\mu^* = 0.13$
100	0.84	478	24.6	20.2
140	0.68	553	17.9	13.5
160	0.66	556	16.7	12.4
200	0.68	501	16.2	12.2
220	0.76	384	16.1	12.7

due to the light hydrogen atoms. We found the structure to be dynamically stable up to 220 GPa. However, if the pressure is increased beyond 225 GPa a dynamical instability arises. The phonon band dispersion at 230 GPa can be found in the appendix D.1. It shows an imaginary (plotted as negative) frequency at the Γ -point, indicating an unstable phonon mode. Following the eigendisplacements of this mode, which are shown in Figure 4.10(c), and then performing a full relaxation of the structure leads to another unreported stable structure with $Cmc2_1$ symmetry. Compared to the $Cmcm$ phase, the silicon framework remains essentially intact while the hydrogen atoms are slightly displaced, partially breaking the symmetry. Due to the strong similarities between the $Cmcm$ and the $Cmc2_1$ structures we do not expect large differences in their phonons or superconducting properties. A similar analysis as above has been carried out following a further imaginary frequency arising at the S -point when the pressure is increased above 260 GPa. The resulting structure found by following the corresponding eigendisplacements resulted in a structure with $P1c1$ -symmetry (see appendix D.1 for details on this structure). The zone center Raman and infrared active phonons for the $Cmcm$ phase are summarized in appendix D.3

In order to investigate the superconducting properties of the $Cmcm$ phase, we use McMillan’s approximate formula for the superconducting transition temperature $T_c = \frac{\Omega_{log}}{1.2} \exp \left[-\frac{1.04(1+\lambda)}{\lambda-\mu^*(1+0.62\lambda)} \right]$ (see appendix D.2 and Ref. [211, 212] for details). McMillan’s formula requires the superconducting properties as the weighted average of the phonon frequencies Ω_{log} , λ which is an average of the electron-phonon interaction, and the dimensionless Coulomb pseudopotential μ^* . These quantities were calculated from the Eliashberg spectral function $\alpha^2F(\omega)$, which was obtained from *ab initio* calculations performed with the ABINIT code [173, 208]. In the right panel of Figure 4.12, the solid lines represent the Eliashberg spectral function of the $Cmcm$ phase at 200 GPa. It has three main features: (i) low optical modes of the silicon framework, (ii) two intense hydrogen peaks around 1500 cm^{-1} and 1600 cm^{-1} , and (iii) high frequency modes of hydrogen around 2000 cm^{-1} .

The superconducting properties of the $Cmcm$ phase at several pressures are summarized

in Table 4.2, using two typical values for the Coulomb pseudopotential $\mu^* = 0.1$ and $\mu^* = 0.13$. For a better comparison, we note that Jin *et al.* [207] set $\mu^* = 0.13$. Assuming the larger of those values, the superconducting transition temperature T_c is 20.1 K at 100 GPa and decreases to 13.0 K at 220 GPa. A decreasing T_c with respect to increasing pressure has been observed in other hydrogen rich materials [203, 213, 120]. We should emphasize that the T_c of the $Cmcm$ phase is smaller by approximately a factor of 6.5 than of the previously reported $P-1$ structure at 200 GPa, and that the $Cmcm$ phase is the lowest enthalpy phase. This raises serious doubts if high- T_c superconductivity will ever be achieved in silane materials under reasonable pressure.

Furthermore, the superconducting properties of the $Cmcm$ phase are strongly linked to its electronic structure. In Figure 4.13, the evolution of the Fermi surface is shown as a function of pressure. Three states cross the Fermi surface. The first (magenta) and the

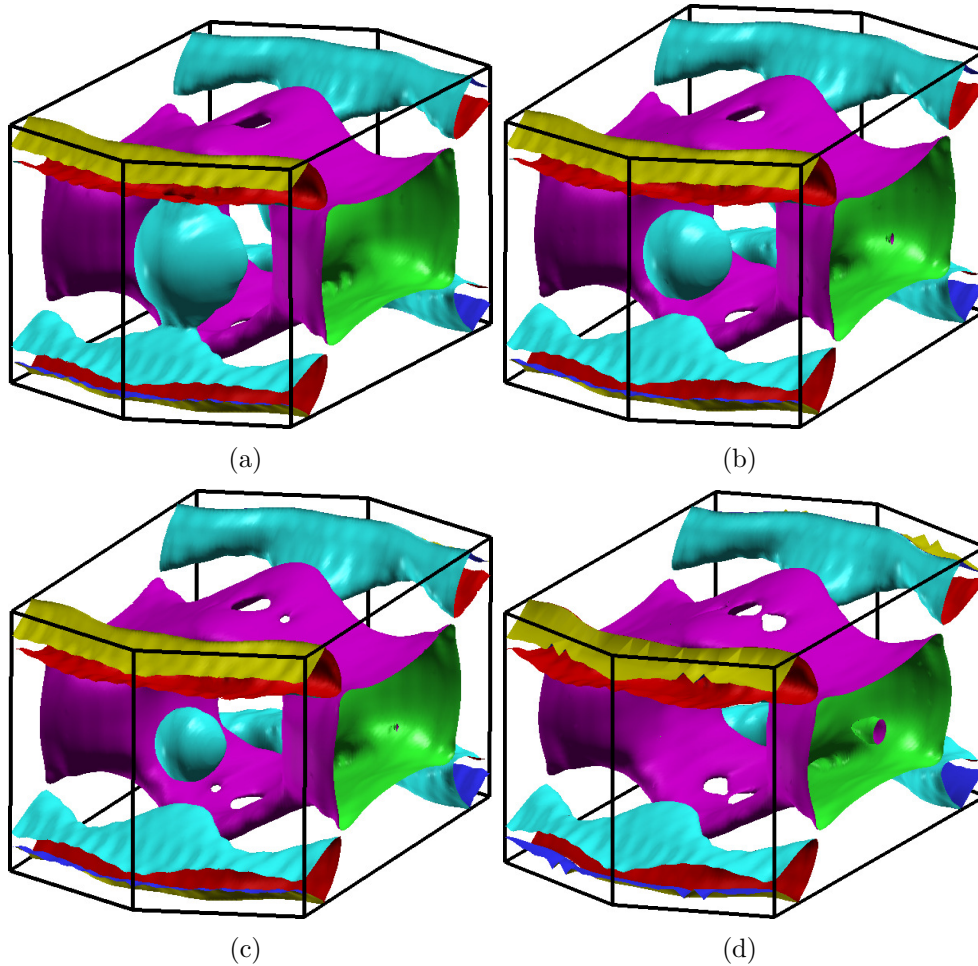


Figure 4.13: Fermi surface of the $Cmcm$ phase at several pressures: a) 100 GPa, b) 140 GPa, c) 160 GPa, and d) 220 GPa. [214]

second (yellow) states cover an important portion of the Brillouin zone that overlaps in the edge of the Brillouin zone and remain nearly unaltered as the pressure increases, whereas the third (cyan) changes substantially. The contribution of this third state to the Fermi surface consists of spherical regions near the Γ -point. This band connects two main portions of the Fermi surface. Therefore, we can expect high superconducting values for low pressures; $\lambda = 0.84$ and $\Omega_{\text{log}} = 480$ with a T_c of 20 K at 100 GPa. However, as the volume of the structure decreases with increasing pressure, this sphere-like feature of the Fermi surface is abruptly reduced. Consequently, at 160 GPa the superconducting parameter λ and T_c clearly decrease, while Ω_{log} only slightly increases; $\lambda = 0.66$, $\Omega_{\text{log}} = 556$ and $T_c = 12.4$ K.

4.3.3 Summary

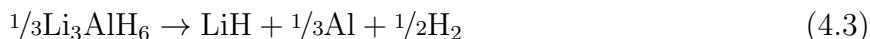
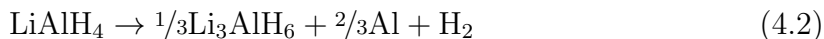
In conclusion, we performed a thorough investigation of the high pressure phases of disilane using first principles calculations. Applying our MHM to explore the PES of disilane, we found a metallic structure which is enthalpically favorable compared to the previously proposed structures of disilane. Additionally, the systematic study of the superconducting properties as a function of pressure shows that the $Cmcm$ phase possesses a moderate electron-phonon coupling, leading to a superconducting transition temperature in the 10–20 K range. This result stands in sharp contrast with the structures previously proposed of disilane under pressure. Moreover, we observed that the transition temperature of the $Cmcm$ structure has the tendency to decrease monotonically with applied pressure, which can be understood by the shrinking of a part of the Fermi surface. This decrease of the T_c is in agreement with most theoretical and experimental results of hydrogen rich materials, including silane [203, 213, 120]. Certainly, this does not imply that superconductivity in hydrogen rich materials is limited to relatively low values of T_c for reasonably high pressure, but our results do impose strong constraints on the possibility of high- T_c superconductors in silicon-hydrogen systems.

Furthermore, our work shows the necessity of performing thorough global geometry optimizations in order to predict accurately the physical properties of the ground-state of any new material. In fact, as we have shown, different meta-stable structures of disilane yield superconducting transition temperatures that can differ by nearly an order of magnitude. This conclusion is clearly general, i.e., for a given stoichiometry the actual arrangement of the atoms can affect strongly the physical properties of a material. Therefore, to obtain meaningful predictions for the ground-state of a new material, fully automated and unconstrained structure prediction schemes should be systematically employed to investigate new material properties.

4.4 Novel structural motifs in low energy phases of LiAlH_4

Limited fossil resources and the increasing amount of CO_2 emission have recently motivated intense research in hydrogen-based energy systems. Hydrogen has been touted as a promising alternative energy source due to its clean reaction with oxygen: the final product is water and heat, and no greenhouse gases are produced. Moreover, hydrogen can provide a high energy density (about three times higher than petrol), and is readily available. The key to widespread applications of hydrogen in industry and in vehicles is the development of suitable solid-state hydrogen storage materials. The goal of 6 weight percentage (wt. %) and 45 g/l of hydrogen in hydride compounds on board fuel cell vehicles has been posed by the US Department of Energy (DOE) in 2010. Further properties required when designing such materials are the need for an efficient hydrogen release mechanism, ideally close to $0.025 \text{ gs}^{-1} \text{ kW}_{\text{fuel cell}}^{-1}$ at temperatures preferably below 100°C and moderate pressures, as well as on-board refueling times less than 10 min at reasonable H_2 pressures. Besides experimental synthesis of candidate materials, *ab initio* methods have been widely applied to assist in searching for novel hydrogen storage materials to satisfy the above requirements (e.g. Ref [215]).

Complex hydrides such as alanates, which are compounds that contain aluminum, hydrogen, and a metal like sodium or lithium, have been widely discussed as promising candidates [216, 217]. In this letter, we investigate the structural diversity of LiAlH_4 , a material that has drawn attention as a hydrogen storage material, since it contains 10.6wt. % hydrogen [218, 219, 220]. The decomposition occurs in three steps with a theoretical release of 7.9 wt. % hydrogen at moderate temperatures in the first two steps [221, 220]:



Note also that complex reactions of LiAlH_4 with LiNH_2 [222, 223], NaNH_2 [224] and $\text{Mg}(\text{NH}_2)_2$ [225] have been investigated and were reported to desorb 5 wt. %, 5.2 wt. % and 8.5 wt. % of hydrogen, respectively. Nevertheless, challenges in reversible dehydrogenation still remain [226].

Recently, the crystal structure of LiAlH_4 was accurately resolved by powder XRD and neutron diffraction experiments [227], which was followed by a detailed theoretical study of the structural, electronic, and thermodynamic properties of this phase [228]. This ternary hydride was found to crystallize in the α - LiAlH_4 phase which has a $P2_1/c$ symmetry. It is an ionic crystal that consists of complex AlH_4^- -anions together with Li^+ -cations [227, 228]. Unfortunately, the phase-diagram of this compound remains relatively unexplored, and several problems still exist in determining its possible polymorphs at various temperatures and pressures. In fact, although LiAlH_4 has been known since 1947 [218] there is still controversy regarding its thermodynamic stability. Spontaneous decomposition of

LiAlH₄ towards Li₃AlH₆ was observed with a half-life of approximately 20 years at room temperature [229], and the first dehydrogenation step was reported to be exothermic [221]. The stability however seems to correlate strongly with impurities in the sample [230], and indeed several theoretical studies predict pure LiAlH₄ to be stable against such decomposition [231, 228], although opposite claims have also been made [232, 233]. Clearly, this is a particularly important problem in view of the use of this compound as a hydrogen storage material, and it could be resolved by enhancing the stability of LiAlH₄.

4.4.1 Structural search

To address this issue we investigated possible low-energy structures of LiAlH₄ using the MHM. Several MHM simulations were performed with cells containing 2 and 4 f.u. of LiAlH₄ starting from different input configurations. During the search process the energies and Hellman-Feynman forces were evaluated within the projector augmented wave formalism as implemented in ABINIT [173, 208]. The PBE [39] exchange-correlation functional was used, which has been found to give reasonable results in earlier studies on lithium analantes [232, 233]. The results were refined using norm-conserving HGH pseudopotentials [176] with a plane-wave cut-off energy of 2700 eV and well converged Monkhorst-Pack [177] *k*-point meshes, resulting in an accuracy of the total energy better than 1 meV per atom. The atomic and cell degrees of freedom were fully relaxed, such that the maximum force components were less than 0.05 eV/Å and stress components less than 0.003 GPa.

During our structural search we discovered a whole class of novel structures with low

Table 4.3: Several low-lying structures are listed with the corresponding space groups (SPG). The energy differences per formula unit of LiAlH₄ with respect to the previously reported α -LiAlH₄ structure are given in the third column, and the contributions of the vibrational zero-point energy (ZPE) are added in the fourth column. All these structures can be found in appendix E.1.

Symmetry	SPG	ΔE (meV)	$\Delta E + \Delta ZPE$ (meV)
<i>P2</i> ₁ / <i>c</i> (deuterium)	14	-111.1	-74.9
<i>P2</i> ₁ / <i>c</i>	14	-111.1	-63.7
<i>P2</i> ₁	4	-82.6	-34.2
<i>Pnc2</i>	30	-81.9	-30.9
<i>P2</i> ₁ / <i>m</i>	11	-81.2	-32.4
<i>Cmmm</i>	65	-66.3	-15.4
<i>P</i> -1	2	-65.2	-12.2
<i>P2</i> ₁ / <i>c</i>	14	-64.4	-15.8
<i>P1</i>	1	-56.8	-4.2
<i>P2</i> / <i>c</i>	13	-54.1	-0.7
<i>P</i> -42 ₁ <i>m</i>	113	-49.5	-1.9

energies. These structures consist of negatively charged polymeric networks of H and Al atoms surrounded by Li^+ ions. These AlH_4 polymers have structures similar to polymeric alane [225] and form both wires and 2D planes within the material. Surprisingly, a large number of such structures was found to be energetically more stable than the experimentally observed $\alpha\text{-LiAlH}_4$ phase. In Table 4.3 we show a selection of these structures, together with the corresponding space group and total energy, taking also into account the zero-point energy (ZPE) correction within the harmonic approximation [234]. The most stable structure found in our simulations belongs to the $P2_1/c$ space group. We will hereon refer to this novel, polymeric structure as $p\text{-}P2_1/c$ and continue to refer to the experimentally observed structure as $\alpha\text{-LiAlH}_4$. The $p\text{-}P2_1/c$ phase is energetically favored over the $\alpha\text{-LiAlH}_4$ phase by $\Delta E = -111.1$ meV/f.u. and $\Delta E + \Delta\text{ZPE} = -63.7$ meV/f.u.. To reconfirm the energetic ordering, calculations with the local density approximation (LDA) [182] and the HSE06 hybrid functional [235, 236, 237] (as implemented in the VASP code [238]) were carried out, resulting in the following relative energies: $\Delta E_{\text{LDA}} = -257.7$ meV/f.u., $\Delta E_{\text{LDA}} + \Delta\text{ZPE}_{\text{LDA}} = -208.5$ meV/f.u., and $\Delta E_{\text{HSE06}} = -506.7$ meV/f.u.

4.4.2 Characterization of the $p\text{-}P2_1/c$ phase

The unit cell of the $p\text{-}P2_1/c$ phase is shown in Figure 4.14. At ambient pressure, the cell parameters are given by $a = 5.162$ Å, $b = 4.279$ Å, $c = 5.084$ Å, $\alpha = \gamma = 90^\circ$ and $\beta = 66.831^\circ$. One Li atom occupies the crystallographic $2b$ site at $(1/2, 0, 0)$, the Al atom occupies the $2c$ site at $(0, 0, 1/2)$, and the H atoms are at the $4e$ sites with coordinates $(0.131, 0.723, 0.680)$ and $(0.316, 0.175, 0.374)$. The Li atoms as well as the Al atoms are arranged in alternating parallel planes, where the Al atoms are interlinked with half the H atoms in the cell with an Al–H distance of 1.77 Å. The rest of the H atoms are single-bonded to the Al atoms, oriented out of plane at a bond-length of 1.68 Å.

We simulated the XRD and neutron diffraction patterns of the $p\text{-}P2_1/c$ structure and compared them with the experimentally observed structure ($\alpha\text{-LiAlH}_4$) of Ref. [227]. A comparison of the XRD spectrum is shown in Figure 4.14(c) (the neutron diffraction pattern can be found in appendix E.2). As expected, the XRD (and neutron) spectra of $p\text{-}P2_1/c$ and $\alpha\text{-LiAlH}_4$ are quite different, proving that these are two distinct phases.

To investigate the electronic structure of the $p\text{-}P2_1/c$ phase we used the perturbative many-body GW technique [182]. To converge the band-structure to better than 0.1 eV we used a $6 \times 6 \times 6$ k -point grid (112 points in the irreducible wedge of the Brillouin zone) and 35 empty bands. These calculations (see Figure 4.15(b)) reveal that the $p\text{-}P2_1/c$ structure is an indirect band-gap semiconductor with a photoemission gap of 5.0 eV and a direct gap at Z of 5.3 eV. The top valance bands are essentially composed of states of d -character provided by the Al atoms and a small portion of p -states of Li, while the bottom of the conduction band is formed by s -states of Al and p -states of Li. The charge transfer among the constituent atoms was analyzed using the Bader charge analysis method as

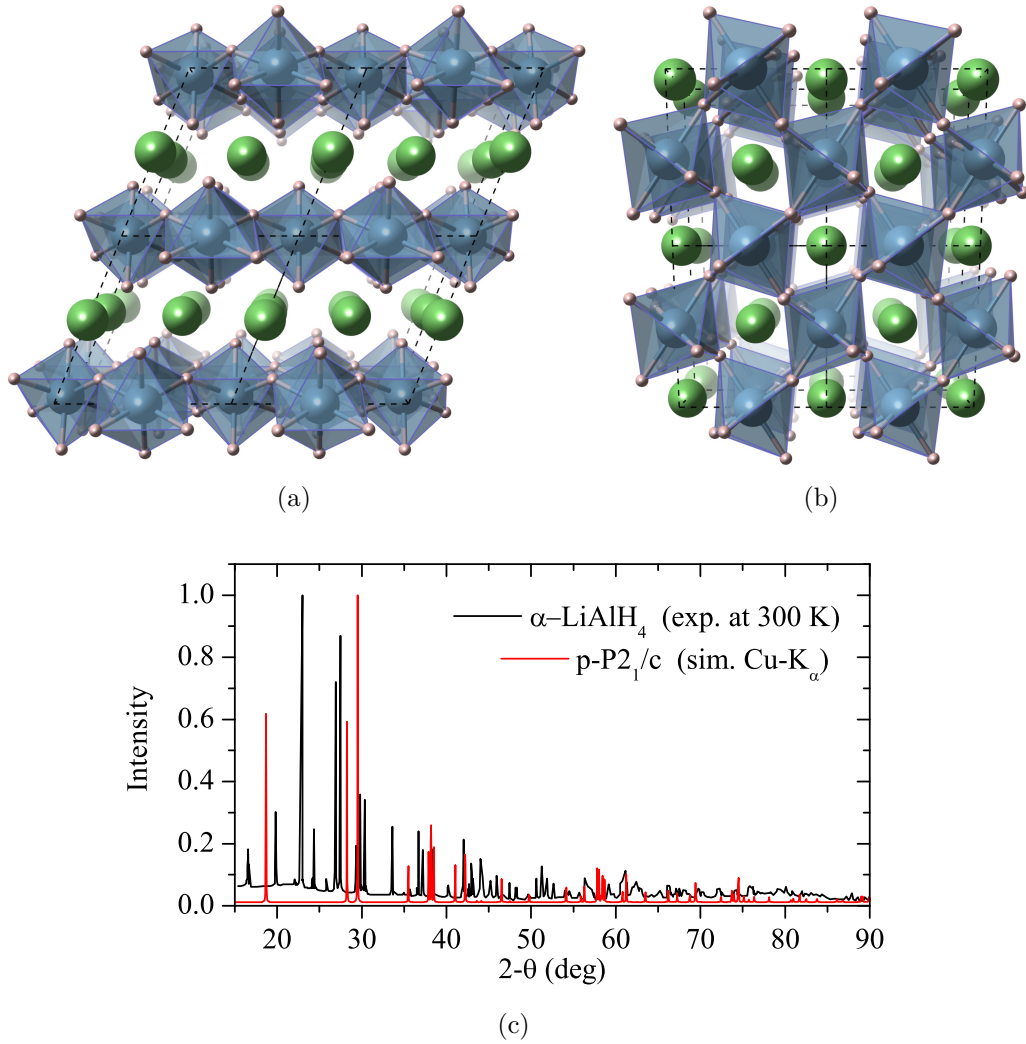


Figure 4.14: (a) The crystal structure of the $p\text{-}P2_1/c$ phase shown from the side and (b) from the top. The hydrogen atoms (small white spheres) form the corners of AlH_4^- polyhedra containing aluminum atoms (in blue). The large (green) spheres represent the Li^+ ions. The arrangement of the polyhedra shows the polymeric structure of Al atoms interlinked by H atoms. In panel (c) the simulated XRD pattern of the $p\text{-}P2_1/c$ phase is compared with the experimental spectrum taken from Ref. [227]

implemented in the ABINIT package [239]. A charge of approximately $-0.87q_e$ /atom is stripped off the Li atoms and transferred to the AlH_4^- substructure, leading to a layered ionic crystal. The electronic charge density within the $p\text{-}P2_1/c$ structure is illustrated in panel (a) of Figure 4.15, clearly showing the layered ionic character of the phase.

We further investigated the dynamical stability of the $p\text{-}P2_1/c$ structure by performing calculations of the phonon dispersion. The phonon spectrum was obtained from density-functional perturbation theory [180] as implemented in ABINIT. Convergence was ensured by a $6 \times 6 \times 6$ Monkhorst-Pack k -point sampling, and a $3 \times 3 \times 3$ q -point sampling

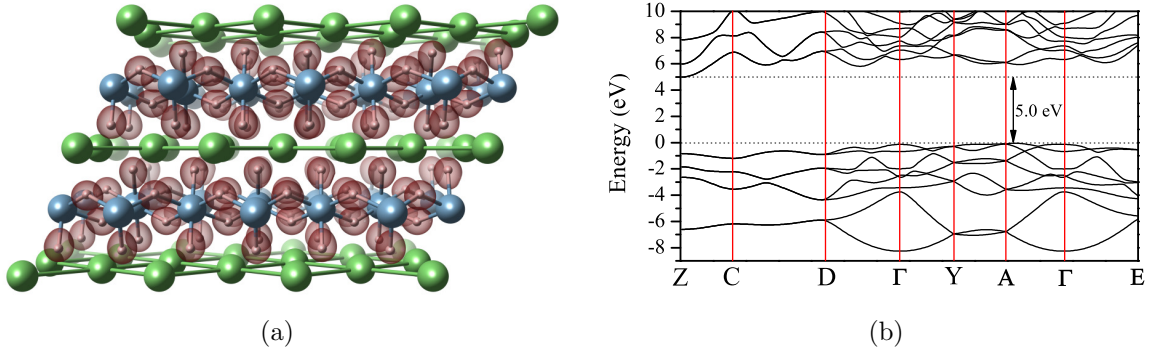


Figure 4.15: Panel (a) shows the layered character of the ionic planes in the $p\text{-}P2_1/c$ phase and the isosurface of the charge density at the value of $0.06q_e$. The GW electronic band-structure calculated for the $p\text{-}P2_1/c$ phase is illustrated in panel (b). The energy was shifted such that the top of the valence band has energy 0.

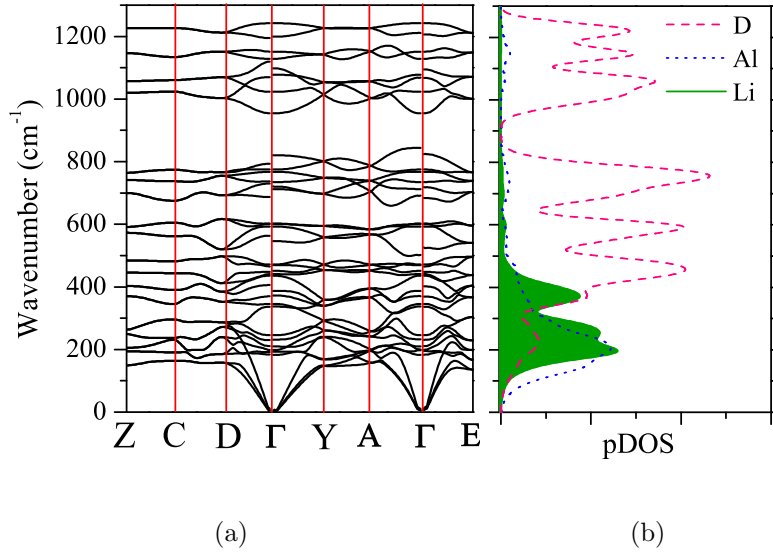


Figure 4.16: (a) The LiAD_4 phonon band dispersion is shown, revealing the dynamical stability of the $p\text{-}P2_1/c$ structure. (b) The partial phonon density of states of LiAD_4 illustrating the contribution of the three atomic species.

for the phonon wave-vectors. The longitudinal optical/transverse optical (LO-TO) zone splittings were taken into account. However, the effect of the LO-TO zone splittings was found to be small, as previously reported for other hydride materials [240, 241].

Panel (a) of Figure 4.16 shows the phonon dispersion calculated for LiAlD_4 . No imaginary phonon frequencies appear within the whole Brillouin zone, ensuring the dynamical

stability of the structure. Replacing deuterium by hydrogen shifts up the characteristic frequencies due to the difference in the atomic masses. Panel (b) of Figure 4.16 represents the partial phonon density of states. As expected, low frequency modes are mostly dominated by vibrations of the Al atoms, together with a smaller contributions from the Li atoms. The high energy range is predominated by the vibrations of deuterium (with frequencies around 1260 cm⁻¹) or hydrogen (around 1750 cm⁻¹).

4.4.3 Low temperature synthesis of polymeric LiAlH₄

Finally, we discuss why the experimentally observed phase is the α -LiAlH₄ and not the energetically lower p - $P2_1/c$ structure. An important hint comes from the observation that these structures contain very light atoms with high vibrational frequencies. One can therefore expect that the phonon contribution to the (free-) energy is large. We computed the ZPE correction within the harmonic approximation [234] for all low-lying structures listed in Table 4.3. The correction is significant, being larger for phases containing AlH₄ polymers, since stronger covalent bonds are present compared to the softer ionic bonds of the α -LiAlH₄ phase. From Table 4.3 we see that the ordering of the phases changes, but that the p - $P2_1/c$ is still the lowest by 30 meV (and lower than the α -LiAlH₄ phase by 64 meV). Moreover, replacing hydrogen by deuterium further stabilizes the structure by around 10 meV.

The situation changes however at finite temperature. The temperature dependence of the free-energy for the four phases with lowest energy are shown in Figure 4.17 relatively to

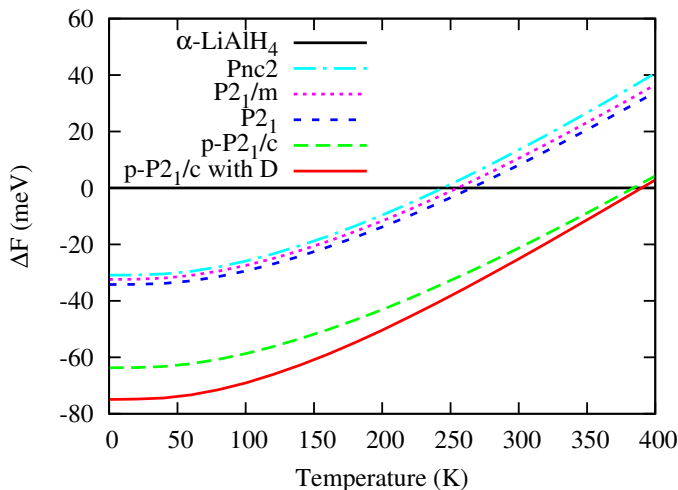


Figure 4.17: The free-energy differences per formula unit of the four lowest phases are plotted with respect to α -LiAlH₄. The lowest curve represents the p - $P2_1/c$ structure where hydrogen was replaced by deuterium (with respect to α -LiAlD₄).

the α -LiAlH₄ structure. Within our approximation, the thermal expansion effects as well as the volume dependence of the ZPE are neglected since thermodynamic quantities have been reported to be fairly insensitive to these corrections [233]. Anharmonic contributions from possible molecular librations are also ignored. We can see that the p- $P2_1/c$ phase has the lowest free-energy up to roughly 380 K, after which it crosses the α -LiAlH₄ phase. This shows that LiAlH₄, like many other similar layered (binary and ternary) amide-hydride systems [242], can have different polymorphs at different temperatures and pressures. These polymorphs are usually linked with the existence of cation vacancies, crystal defects and the mechanism of the dehydrogenation/rehydrogenation process [243]. Furthermore, a direct comparison with the free energy calculations in Ref. [232] and Ref. [233] shows that the p- $P2_1/c$ phase would lead to an endothermic behaviour of reaction (4.2) at least for low temperatures. Note that one can expect a systematic error in the transition temperature due to the approximations employed in the DFT and free energy calculations.

Possible reasons for the fact that the p- $P2_1/c$ phase has not been observed yet might lie within the conventional methods to synthesize crystalline LiAlH₄. Originally it was prepared from LiH and AlCl₃ in boiling diethyl ether [218], leading to temperatures of at least 307.8 K. In fact, temperatures might have been considerably higher and in a range where p- $P2_1/c$ becomes unstable or has a too high formation barrier. Industrial synthesis is performed through a metathesis reaction of NaAlH₄ with LiCl [244]. Since NaAlH₄ already contains complex AlH₄⁻ anions, its reformation and polymerization is unlikely, especially when considering the strong Coulomb repulsive forces. Using AlH₃ as a reactant and a low temperature synthesis might be a possible pathway en route to the synthesis of the novel p- $P2_1/c$ phase. We propose the following reaction:



The reaction was studied with respect to its thermodynamic properties, using the α -AlH₃ phase [245] with $R\bar{3}c$ symmetry, the $Fm\bar{3}m$ LiH phase [246] and the novel p- $P2_1/c$ phase of LiAlH₄. Our calculations reveal that reaction (4.4) is exothermic by $\Delta E = 138.4$ meV/f.u. Taking into account the vibrational free energy the reaction heat increases to $\Delta F_{0\text{K}} = 203.1$ meV/f.u. at a temperature of 0 K and $\Delta F_{298\text{K}} = 140.8$ meV/f.u. at a temperature of 298 K. Although these results do not guarantee the success of the above pathway, they show that it is thermodynamically accessible.

4.4.4 Summary

In conclusion, we performed a systematic structural search for LiAlH₄ and identified a class of novel structures. In contrast to other alاناتes and previous predictions, AlH₄ does not form complex anions but appears rather as a polymeric network. The most stable structure, p- $P2_1/c$, exhibits a layered ionic configuration and is favored at ambient pressure for temperatures up to roughly 380 K. This phase is a polar semiconductor with

an indirect band-gap of 5.0 eV, and by replacing hydrogen with deuterium the material can be further stabilized with respect to α -LiAlD₄. Moreover, it can probably be produced by using a low-temperature synthesis, and by using precursors not containing complex AlH₄⁻ anions. As this phase is energetically more stable than α -LiAlH₄ there are good chances that it solves the stability problems of the latter. Furthermore, the existence of these new phases can have profound implications for the dehydrogenation/rehydrogenation process and for understanding and developing novel materials for hydrogen storage.

CONCLUSIONS AND OUTLOOK

In this thesis we present our results for *ab initio* predictions of crystal structures by employing a global geometry optimization scheme. We first developed a crystal structure prediction method by generalizing the MHM to periodic systems. Then, it was used to predict the structures of novel phases in several materials. Below we briefly summarize the method development and the results of our work.

In chapter 2 we characterized the PES of silicon systems by comparing fast, but less accurate force fields to more accurate but computationally expensive *ab initio* methods. We found clear evidences that all force fields are considerably less accurate than the Lenosky tight-binding scheme, which however is almost as accurate as DFT calculations. The configurational density of states was evaluated by sampling low energy structures with the MHM. Both for isolated and crystalline systems we found that force fields overestimate the number of local minima on the PES, giving an overall very rough energy landscape. We conclude that directly exploring the energy landscape at the tight-binding or DFT level is preferable over pre-screening the low energy phases with empirical force fields which might slow down a meaningful structural search through the vast amount of spurious minima.

We then developed a new crystal structure prediction scheme by generalizing the MHM to periodic systems in chapter 3. A thorough structural search is ensured by employing the variable cell shape Parrinello-Rahman molecular dynamics for the escape trials. A simple discretization scheme is derived to integrate the corresponding equations of motion. Different unconstrained local geometry optimization schemes of cell and atomic coordinates were implemented and compared to each other, of which the FIRE method was identified to be a good compromise of stability and efficiency in DFT calculations.

Several approaches to optimize the performance of the structural search were evaluated as well:

- *Softening* is used to align the initial MD velocities preferably along soft-mode directions to exploit the Bell-Evans-Polanyi principle and efficiently cross over low-energy barriers. For a model Lennard-Jones system we demonstrated that *softening* increases the efficiency by almost a factor of 3.
- An analysis of structural databases showed a non-uniform distribution of the 230 space groups in nature, with a preference for high-symmetry structures for most inorganic compounds. Based on this empirical observation, we discussed the impact of symmetrized input structures on the minima hopping efficiency and showed that, with an appropriate choice of the space group symmetry and unit cell size, the performance can be improved by more than one order of magnitude for a Lennard-Jones mixture.
- The MHM was parallelized for investigating silicon crystals within the EDIP force field. With the appropriate number of parallel MHM runs the efficiency could be improved by a factor of 2.
- For silicon systems, MHM runs might get trapped in funnels of the PES which are described by simulation cells unsuited to represent the ground state crystal with the given number of atoms. The Lattice Vector Prediction Scheme was designed to circumvent this problem by adding or subtracting 2 atoms at the appropriate location. By employing the LVPS the success rate could be increased from 80% to 95%.

In chapter 4 we present several application of the MHM for *ab initio* crystal structure prediction:

Two novel carbon allotropes were identified as candidates for cold compressed graphite, *Z*- and *M10*-carbon. They become more stable than graphite at a pressure slightly below 10 GPa and 14.4 GPa, respectively. Our simulations revealed that both phases could explain the changes in the XRD pattern measured in cold compressed graphite [166, 167, 168]. Furthermore, evidences for the existence of *Z*-carbon were gathered from Raman spectroscopy experiments conducted by José A. Flores-Livas in Lyon, France. We observed that the G-band mode of graphite suffers an abrupt broadening above 9-10 GPa, and a new peak at 1082 cm^{-1} appears in the Raman spectrum in the same pressure range. These observations can be well explained by the existence of *Z*-carbon in samples of cold compressed graphite.

Superconducting phases of disilane at high pressure were investigated in section 4.3. A novel metallic structure with *Cmcm* symmetry was identified to be the most stable in a wide pressure range up to 280 GPa. Due to its moderate electron-phonon coupling

we predict a superconducting transition temperature of 12 K at 200 GPa, which is in sharp contrast to earlier predictions reported by Jin *et al.* [207] of $T_c = 80.1$ K in a $P-1$ structure at the same pressure. This striking difference in the transition temperature shows the essential need for a thorough structural search to obtain meaningful predictions of a physical property in a compound

Finally, we report on novel structural motifs in the hydrogen storage material LiAlH_4 . Our simulations predict a large number of low energy structures in which AlH_4 form polymeric substructures instead of complex molecular anions. We predict a novel $p-P2_1/c$ phase, a layered ionic crystal, to be the ground state structure of LiAlH_4 at low temperatures. However, it becomes unstable with respect to the experimentally observed $\alpha\text{-LiAlH}_4$ structure at higher temperatures due to vibrational entropy effects. A successful synthesis of the $p-P2_1/c$ phase, which should be possible at low temperatures, would probably enhance the stability of this compound and thus improve its applicability for hydrogen storage on board fuel cell vehicles.

Overall, the MHM has been shown to be well suited for crystal structure prediction. In contrast to other methods the efficiency of the MHM is based on physical principles. It is applicable to any periodic system for which the total energy, the atomic forces and the stresses can be evaluated (such as in density functional theory) thus rendering it a highly versatile method. Since the moves on the PES are based on the Newtonian equation of motion it allows to some extent an insight into dynamical effects as well, such as approximative barrier heights and kinetics of phase transitions. The MHM can be readily restricted to surface-periodic and wire-periodic boundary conditions allowing the study of nano-structures, surface reconstructions, grain boundaries or diffusion effects. The main limitations are imposed solely by available computational resources which currently allow the study of realistic systems of at most few dozen atoms per simulation cell at the DFT level.

Appendix A

Stress and strain

The strain is defined as a deformation of a material. Thereby, any point \mathbf{r} in space is displaced towards \mathbf{r}' , which can be described by the second-order strain tensor $\epsilon_{\alpha,\beta}$:

$$\mathbf{r}'_{\alpha} = \sum_{\beta} (\delta_{\alpha\beta} + \epsilon_{\alpha\beta}) \mathbf{r}_{\beta} \quad (\text{A.1})$$

The Cauchy stress tensor σ is defined as the negative strain derivatives of the energy per unit volume

$$\sigma_{\alpha\beta} = -\frac{1}{\Omega} \frac{\partial E}{\partial \epsilon_{\alpha\beta}} \quad (\text{A.2})$$

For any vector \mathbf{r} the strain derivative is given by

$$\frac{\partial \mathbf{r}_{\alpha}}{\partial \epsilon_{\kappa\lambda}} = \delta_{\alpha\kappa} \mathbf{r}_{\lambda} \quad (\text{A.3})$$

Equation (A.3) readily applies for the 3 cell vectors $\mathbf{a}, \mathbf{b}, \mathbf{c}$, which are combined in a 3×3 matrix $h = \{\mathbf{a}, \mathbf{b}, \mathbf{c}\}$. Therefore, the derivative of the cell vectors h with respect to strain is given by

$$\frac{\partial h_{\alpha\beta}}{\partial \epsilon_{\kappa\lambda}} = \delta_{\alpha\kappa} h_{\lambda\beta} \quad (\text{A.4})$$

The Cauchy stress tensor can thus be written as

$$\sigma_{\alpha\beta} = -\frac{1}{\Omega} \frac{\partial E}{\partial \epsilon_{\alpha\beta}} = -\frac{1}{\Omega} \sum_{\kappa} \sum_{\lambda} \frac{\partial E}{\partial h_{\kappa\lambda}} \frac{\partial h_{\kappa\lambda}}{\partial \epsilon_{\alpha\beta}} = -\frac{1}{\Omega} \sum_{\lambda} \frac{\partial E}{\partial h_{\alpha\lambda}} h_{\beta\lambda} \quad (\text{A.5})$$

If we define the cell gradients of the potential energy

$$f_{\alpha,\beta}^h = \frac{\partial E(\{\mathbf{s}_i\}, h)}{\partial h_{\alpha,\beta}} \quad (\text{A.6})$$

we can express the Cauchy stress tensor as

$$\sigma = -\frac{1}{\Omega} f^h h^T \tag{A.7}$$

Appendix B

Derivation of the Parrinello-Rahman equation's of motion

Here we will derive the equations of motion for the Parrinello-Rahman dynamics.

The Lagrangian is given by

$$\mathcal{L} = \sum_{i=1}^N \frac{m_i}{2} \dot{\mathbf{s}}_i^T g \dot{\mathbf{s}}_i - E(\{\mathbf{s}_j\}, h) + \frac{W}{2} \text{Tr}(\dot{h}^T \dot{h}) - P\Omega(h) \quad (\text{B.1})$$

and the equations of motion need to be found applying the Lagrange's equation

$$\frac{d}{dt} \frac{\partial \mathcal{L}}{\partial \dot{q}_i} = \frac{\partial \mathcal{L}}{\partial q_i} \quad (\text{B.2})$$

where q_i are any of the atomic or cell coordinates.

We will first consider the reduced atomic coordinates \mathbf{s}_i . We have

$$\frac{\partial \mathcal{L}}{\partial \mathbf{s}_i} = - \frac{\partial E(\{\mathbf{s}_j\}, h)}{\mathbf{s}_i} \quad (\text{B.3})$$

$$\frac{\partial \mathcal{L}}{\partial \dot{\mathbf{s}}_i} = \frac{m_i}{2} 2g \dot{\mathbf{s}}_i = m_i g \dot{\mathbf{s}}_i \quad (\text{B.4})$$

$$\frac{d}{dt} \frac{\partial \mathcal{L}}{\partial \dot{\mathbf{s}}_i} = m_i (g \ddot{\mathbf{s}}_i + \dot{g} \dot{\mathbf{s}}_i) \quad (\text{B.5})$$

Together with equation (B.2) we obtain

$$\ddot{\mathbf{s}}_i = - \frac{g^{-1}}{m_i} \frac{\partial E}{\partial \mathbf{s}_i} - g^{-1} \dot{g} \dot{\mathbf{s}}_i \quad (\text{B.6})$$

Now we consider the cell derivatives:

$$\frac{\partial \mathcal{L}}{\partial \mathbf{h}} = \frac{\partial}{\partial \mathbf{h}} \left(\sum_{i=1}^N \frac{m_i}{2} \dot{\mathbf{s}}_i^T g \dot{\mathbf{s}}_i \right) - \frac{\partial E(\{\mathbf{s}_j\}, h)}{h} - P\eta \quad (\text{B.7})$$

$$\frac{\partial \mathcal{L}}{\partial \dot{\mathbf{h}}} = W\dot{\mathbf{h}} \quad (\text{B.8})$$

$$\frac{d}{dt} \frac{\partial \mathcal{L}}{\partial \dot{\mathbf{h}}} = W\ddot{\mathbf{h}} \quad (\text{B.9})$$

We simply rewrote $\text{Tr}(\dot{h}^T \dot{h}) = \sum_{\alpha} \sum_{\beta} \dot{h}_{\alpha\beta}$ and used the following identity:

$$\frac{\partial \Omega}{\partial h} = \det(h)(h^{-1})^T = \Omega(h^{-1})^T \quad (\text{B.10})$$

or equivalently

$$\eta := \{\mathbf{b} \times \mathbf{c}, \mathbf{c} \times \mathbf{a}, \mathbf{a} \times \mathbf{b}\} = \frac{\partial \Omega}{\partial h} \quad (\text{B.11})$$

The first term of equation (B.7) can be reformulated to:

$$\frac{\partial}{\partial h_{kl}} \left(\sum_{i=1}^N \frac{m_i}{2} \dot{\mathbf{s}}_i^T g \dot{\mathbf{s}}_i \right) = \frac{\partial}{\partial h_{kl}} \left(\sum_{i=1}^N \frac{m_i}{2} (h\dot{\mathbf{s}}_i)^T (h\dot{\mathbf{s}}_i) \right) \quad (\text{B.12})$$

$$= \frac{\partial}{\partial h_{kl}} \left(\sum_{i=1}^N \frac{m_i}{2} \sum_{\alpha} \left(\sum_{\beta} h_{\alpha\beta} \dot{\mathbf{s}}_i^{\beta} \sum_{\gamma} h_{\alpha\gamma} \dot{\mathbf{s}}_i^{\gamma} \right) \right) \quad (\text{B.13})$$

$$= \sum_{i=1}^N \frac{m_i}{2} \sum_{\alpha} \left(\delta_{k\alpha} \dot{\mathbf{s}}_i^l \sum_{\gamma} h_{\alpha\gamma} \dot{\mathbf{s}}_i^{\gamma} + \delta_{k\alpha} \dot{\mathbf{s}}_i^l \sum_{\beta} h_{\alpha\beta} \dot{\mathbf{s}}_i^{\beta} \right) \quad (\text{B.14})$$

$$= \sum_{i=1}^N m_i \dot{\mathbf{s}}_i^l \sum_{\gamma} h_{k\gamma} \dot{\mathbf{s}}_i^{\gamma} \quad (\text{B.15})$$

which is equivalent to

$$\frac{\partial}{\partial h} \left(\sum_{i=1}^N \frac{m_i}{2} \dot{\mathbf{s}}_i^T g \dot{\mathbf{s}}_i \right) = \sum_{i=1}^N m_i h \dot{\mathbf{s}}_i \dot{\mathbf{s}}_i^T \quad (\text{B.16})$$

The following identity is used to express $\dot{\mathbf{s}}_i^T$ with respect to the cell derivative:

$$h \dot{\mathbf{s}}_i \dot{\mathbf{s}}_i^T = h \dot{\mathbf{s}}_i (h^{-1} h \dot{\mathbf{s}}_i)^T = h \dot{\mathbf{s}}_i (h \dot{\mathbf{s}}_i)^T (h^{-1})^T = h \dot{\mathbf{s}}_i (h \dot{\mathbf{s}}_i)^T \frac{\eta}{\Omega} \quad (\text{B.17})$$

where the last equality is given by equations (B.10) and (B.11).

The equation of motion for the cell is thus

$$\ddot{h} = \frac{1}{W} \left(\frac{\eta}{\Omega} \sum_{i=1}^N m_i h \dot{\mathbf{s}}_i (h \dot{\mathbf{s}}_i)^T - \frac{\partial E(\{\mathbf{s}_j\}, h)}{h} - P\eta \right) \quad (\text{B.18})$$

$$= \frac{1}{W} \left(\frac{\eta}{\Omega} \left[\sum_{i=1}^N m_i h \dot{\mathbf{s}}_i (h \dot{\mathbf{s}}_i)^T - f^h h^T \right] - P\eta \right) \quad (\text{B.19})$$

$$= \frac{1}{W} (\Pi - P)\eta \quad (\text{B.20})$$

where we again used equations (B.10), (B.11) and (A.6) in (B.19), and finally equation (3.15) in (B.20).

Appendix C

E_{diff} parameter

We will prove here that $\alpha_2 = \frac{1}{\alpha_1}$ will ensure that, in average, half of the minima proposed by the inner loop will be accepted and half of them will be rejected.

Assume that a MHM simulation is started with some initial value of E_{diff}^i , and the final value is E_{diff}^f after N minima proposed by the inner loop. We see that

$$E_{\text{diff}}^f = \alpha_1^k \alpha_2^l E_{\text{diff}}^i \quad (\text{C.1})$$

where k and l are the number of accepted and rejected minima, respectively, and $k+l = N$. Without loss of generality we can set $E_{\text{diff}}^i = E_{\text{diff}}^f$ for large N , thus arriving at

$$1 = \alpha_1^k \alpha_2^l \quad (\text{C.2})$$

and

$$\alpha_2 = \left(\frac{1}{\alpha_1} \right)^{\frac{k}{l}} \quad (\text{C.3})$$

We require that half of the structures are accepted, thus $k = l$ and therefore

$$\alpha_2 = \frac{1}{\alpha_1} \quad (\text{C.4})$$

Additional material for Disilane

D.1 Dynamical stability and the structural evolution with pressure

Figure D.1 presents the phonon dispersion of the $Cmcm$ structure at 90 GPa (a), 230 GPa (b) and 260 GPa (c). This is the enthalpically most favored structure in the range of 95 GPa to 225 GPa. From 90 to 225 GPa all phonon frequencies are real, indicating that the $Cmcm$ phase is dynamically stable. However, at 230 GPa the phonon frequencies become imaginary at the Γ -point, thus indicating the limit of stability of the $Cmcm$ structure. At 260 GPa, further imaginary frequencies appear at the S -point.

A systematic study was carried out following the eigendisplacements of the imaginary acoustical modes at Γ and S , and then relaxing the perturbed structure. The displacements at Γ lead to a structure with slightly broken symmetry belonging to the space group $Cmc2_1$ (the structure is given in Table D.1), where the hydrogen atoms are displaced but the silicon framework is left intact. This new structure is the most stable in the pressure range from 230 up to 260 GPa. To analyze the eigendisplacements corresponding to the imaginary frequencies at S a $1 \times 4 \times 4$ supercell was constructed of the conventional $Cmcm$ cell containing 256 atoms. The resulting relaxed structure has low symmetry ($P1c1$ space group) and does not show any imaginary phonon frequencies. The atomic coordinates are given in Table D.2.

In the high pressure domain above 280 GPa (almost the experimental limit to date) several structures compete within a very small enthalpy interval, where a new structure was found with $P-1$ symmetry that has an enthalpy comparable to other previously proposed structures. The cell parameters at 300 GPa are $a = 4.141 \text{ \AA}$, $b = 2.984 \text{ \AA}$, $c = 4.020 \text{ \AA}$, $\alpha = 108.33^\circ$, $\beta = 81.85^\circ$ and $\gamma = 110.43^\circ$. The $2i$ sites are occupied by silicon atoms at

(0.337,0.426,0.239) and (0.915,0.700,0.240), and by hydrogen atoms at (0.380,0.106,0.681), (0.301, 0.963, 0.352), (0.360,0.696,0.619), (0.411,0.784,0.993), (0.035,0.742,0.622) and (0.832,0.047,0.027). The phonon dispersion of this structure is shown in Figure D.1(d).

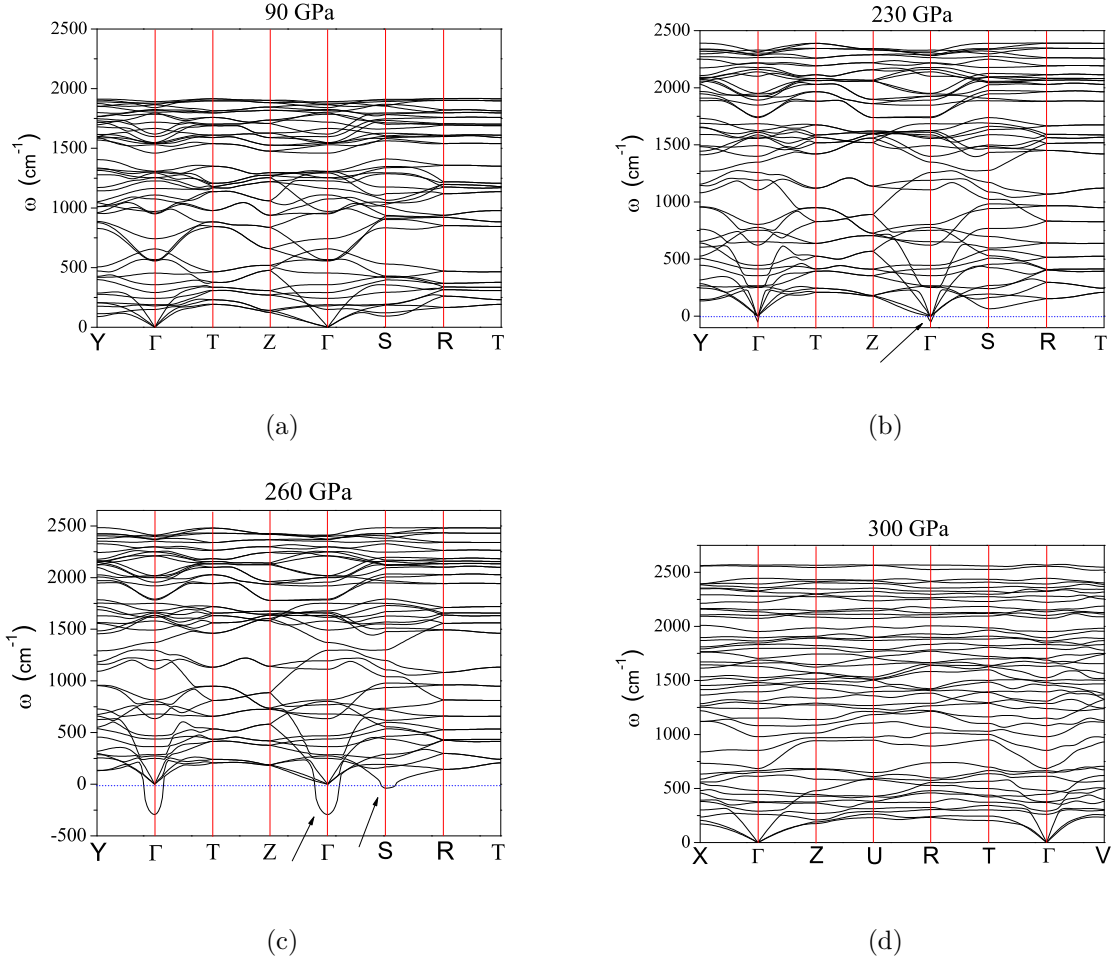


Figure D.1: The phonon band dispersion of the Cmc phase is shown at 90 GPa (a), at 230 GPa (b) and at 260 GPa (c). The phonon band dispersion of the $P-1$ phase is shown at 300 GPa (d). This high pressure $P-1$ structure is dynamically stable at 300 GPa and enthalpically favorable above 400 GPa.

D.2 Superconductivity

The superconducting transition temperature was estimated through McMillan's equation [211].

$$T_c = \frac{\Omega_{\log}}{1.2} \exp \left[-\frac{1.04(1+\lambda)}{\lambda - \mu^*(1+0.62\lambda)} \right] \quad (\text{D.1})$$

and the superconducting parameters were calculated using the Allen-Dynes modification of McMillan's formulation [212]. The parameter λ , the dimensionless measure of the electron-phonon interaction, reads

$$\lambda = \int \frac{\alpha^2 F(\omega)}{\omega} d\omega \quad (\text{D.2})$$

and Ω_{\log} , the weighted average of the phonon frequencies, is

$$\Omega_{\log} = \exp\left(\frac{\lambda}{2} \int \frac{\alpha^2 F(\omega)}{\omega} \ln(\omega) d\omega\right) \quad (\text{D.3})$$

and finally μ^* is the Coulomb pseudopotential.

The Eliashberg spectral function $\alpha^2 F(\omega)$ is shown in Figure D.2 for the *Cmcm* phase. Three different zones of the spectra contribute significantly to the electron-phonon coupling. First, the low-lying optical modes due to the vibration of the silicon framework contribute to the curve below 700 cm^{-1} . Second, two intense peaks appear at around 1100 and 1600 cm^{-1} . Finally, we observe high frequency optical modes related to vibrations of the hydrogen atoms above 2000 cm^{-1} . Additionally, the superconductivity parameters λ and ω_{\log} are summarized in Figure D.3 as a function of pressure.

Furthermore, the influence of the structural differences between the previously reported *P-1* phase in Ref. [207] and the *Cmcm* phase on the superconducting temperatures was investigated. As a general observation the two structures are completely different, in particular the *P-1* structure has considerably less symmetry than the *Cmcm* phase. Furthermore, the five-fold coordinated silicon framework of the *Cmcm* arrangement is no longer present in the *P-1* structure. As a result of the reduced symmetry, the lattice vibrations in the *P-1* phase are substantially different, as well as the electronic Fermi surfaces. In Figure D.4 we display the Fermi surfaces calculated at 200 GPa for the *P-1* and the *Cmcm* phase. The Fermi surface of the *P-1* structure is much larger (and therefore has a higher density of states at the Fermi energy) than the Fermi surface of the *Cmcm* phase. As a direct consequence, the electron-phonon coupling is also expected to be stronger in the *P-1* phase, explaining the very high T_c obtained for this material by Jin *et al.* [207].

Table D.1: Structure of the *Cmc2₁* phase of disilane at 280 GPa. Lattice parameters: $a = 7.731 \text{ \AA}$, $b = 2.589 \text{ \AA}$, $c = 4.581 \text{ \AA}$, $\alpha = \beta = \gamma = 90.0^\circ$

Element	x	y	z
Si1	-0.14089	0.00043	-0.00541
H1	0.20665	0.33782	-0.25571
H2	-0.41538	0.19038	-0.25344
H3	0.00000	0.29796	-0.38066
H4	0.00000	0.33688	-0.09697

Table D.2: Structure of the $P1c1$ phase of disilane at 280 GPa. Lattice parameters: $a = 4.567 \text{ \AA}$, $b = 15.470 \text{ \AA}$, $c = 5.193 \text{ \AA}$, $\alpha = \beta = \gamma = 90.0^\circ$

Element	x	y	z	Element	x	y	z
Si1	-0.00144	-0.07271	-0.01515	H17	-0.27211	0.39645	-0.33093
Si2	0.49306	-0.42711	-0.01525	H18	-0.23570	-0.10352	0.16957
Si3	-0.00680	-0.43181	0.01440	H19	-0.26440	0.45723	-0.15663
Si4	0.49872	-0.06814	0.01562	H20	-0.24396	-0.04274	0.34296
Si5	-0.00537	-0.32254	-0.23469	H21	0.26619	0.39807	-0.16960
Si6	-0.00148	0.18184	0.23484	H22	0.22578	-0.10211	0.33002
Si7	0.49887	0.32287	-0.23474	H23	0.25361	0.45744	-0.34448
Si8	0.49377	-0.18216	0.23408	H24	0.23815	-0.04240	0.15571
Si9	-0.00129	0.31818	-0.26451	H25	-0.23508	-0.39637	-0.32914
Si10	-0.00580	-0.17743	0.26508	H26	-0.27307	0.10363	0.17029
Si11	0.49393	-0.31788	-0.26706	H27	-0.25191	-0.45773	-0.15565
Si12	0.49841	0.17720	0.26518	H28	-0.25672	0.04228	0.34464
Si13	-0.00602	-0.06797	-0.48413	H29	0.36226	0.49911	-0.14327
Si14	-0.00274	0.42744	-0.01517	H30	0.41742	0.00175	0.32617
Si15	0.49796	-0.43218	-0.48314	H31	-0.13906	-0.49499	-0.35675
Si16	0.49431	0.07263	-0.01538	H32	-0.08287	-0.00610	0.17443
H1	0.22674	-0.14638	0.07956	H33	0.07625	-0.49846	-0.17349
H2	0.24327	-0.20771	-0.09459	H34	0.13168	-0.00089	0.35758
H3	-0.27450	-0.35194	-0.08038	H35	-0.42348	0.49347	-0.32621
H4	-0.26164	-0.29247	0.09447	H36	-0.36716	0.00526	0.14238
H5	0.26406	-0.35346	0.08088	H37	0.26372	-0.14634	-0.41935
H6	0.25653	-0.29275	-0.09349	H38	0.22668	0.35373	0.07917
H7	-0.23418	-0.14801	-0.07923	H39	0.25573	-0.20725	0.40699
H8	-0.23877	-0.20842	0.09476	H40	0.24382	0.29224	-0.09427
H9	0.41614	-0.25638	0.07609	H41	-0.23403	-0.35207	0.42101
H10	-0.08369	-0.24839	-0.07639	H42	-0.27408	0.14785	-0.08029
H11	0.13174	-0.24491	0.10717	H43	-0.23821	-0.29153	-0.40508
H12	-0.36994	-0.25088	-0.10711	H44	-0.26209	0.20750	0.09446
H13	0.22610	-0.39795	-0.17112	H45	0.41597	-0.24361	-0.42417
H14	0.26610	0.10189	0.32945	H46	-0.08366	-0.25165	0.42365
H15	0.23023	-0.45850	-0.34499	H47	0.13164	-0.25506	-0.39292
H16	0.26163	0.04164	0.15519	H48	-0.36927	-0.24911	0.39292

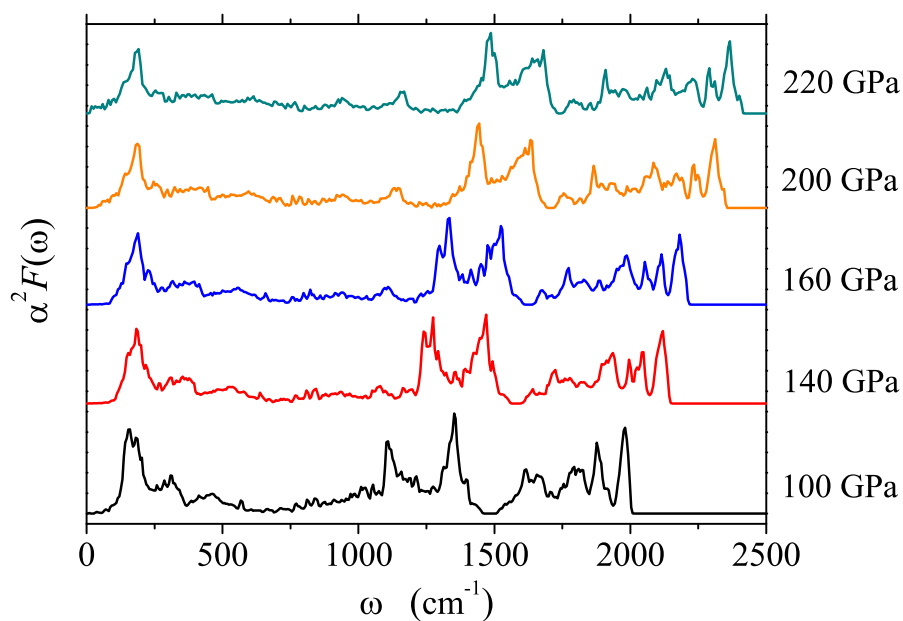


Figure D.2: Eliashberg spectral function $\alpha^2 F(\omega)$ and its dependence on pressure for the $Cmcm$ phase of disilane.

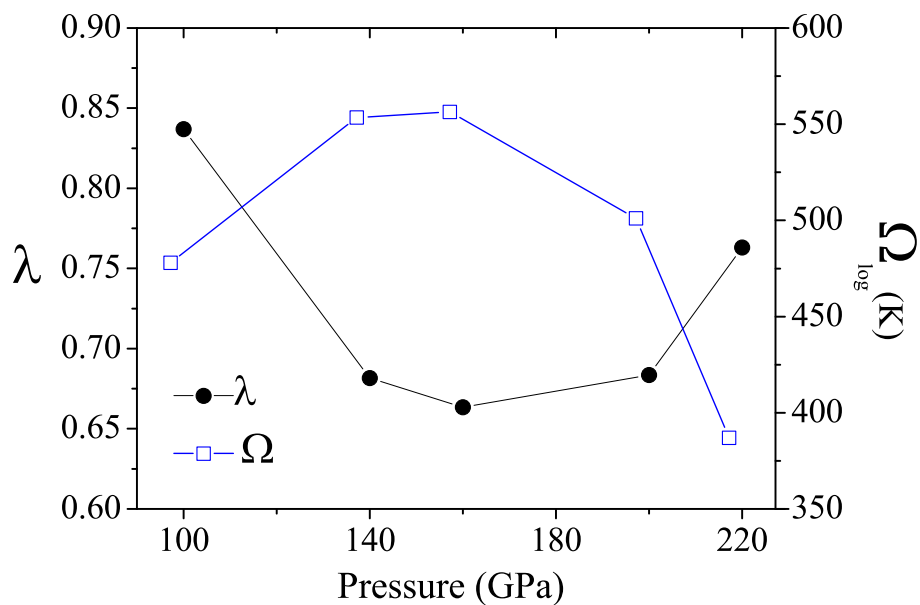


Figure D.3: Superconducting parameters of the $Cmcm$ structure as a function of pressure.

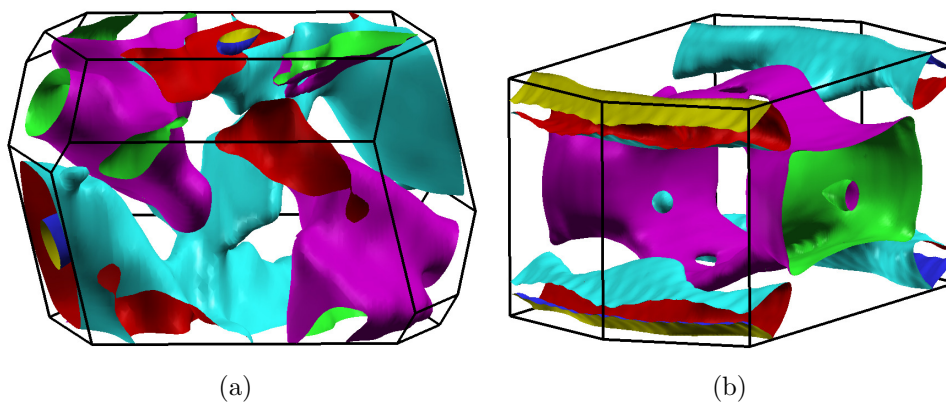


Figure D.4: Comparison of the Fermi surfaces at 200GPa of the previously reported $P-1$ phase (a) and the new $Cmcm$ phase (b).

D.3 Raman and IR activity

Table D.3 and Table D.4 summarize the calculated zone center Raman and infrared active phonons for the $Cmcm$ phase at two selected pressures, 100 GPa and 200 GPa. The mechanical representation of Raman and IR modes are:

$$\text{IR active modes: } \Gamma^{IR} = 5B_{1u} + 6B_{2u} + 4B_{3u}$$

$$\text{Raman active modes: } \Gamma^{Rmn} = 5A_g + 5B_{1g} + 4B_{2g} + 4B_{3g}$$

Table D.3: Raman and IR modes of the $Cmcm$ phase at 100 GPa.

Mode	Character	Frequency (cm ⁻¹)
A_g	Raman	556.4
A_g	Raman	958.7
A_g	Raman	1244.5
A_g	Raman	1323.2
A_g	Raman	1564.9
A_g	Raman	1662.0
A_g	Raman	1947.8
B_{1g}	Raman	309.5
B_{1g}	Raman	374.6
B_{1g}	Raman	766.6
B_{1g}	Raman	1324.9
B_{1g}	Raman	1589.1
B_{1g}	Raman	1805.0
B_{1g}	Raman	1916.2
B_{2g}	Raman	467.8
B_{2g}	Raman	1114.1
B_{2g}	Raman	1181.3
B_{2g}	Raman	1864.7
B_{2g}	Raman	1900.3
B_{3g}	Raman	101.3
B_{3g}	Raman	244.8
B_{3g}	Raman	919.7
B_{3g}	Raman	1737.2
B_{3g}	Raman	1897.6
B_{1u}	IR	184.0
B_{1u}	IR	548.5
B_{1u}	IR	1345.5
B_{1u}	IR	1608.4
B_{1u}	IR	1867.4
B_{2u}	IR	577.8
B_{2u}	IR	1333.4
B_{2u}	IR	1500.1
B_{2u}	IR	1844.7
B_{2u}	IR	1923.8
B_{3u}	IR	670.9
B_{3u}	IR	965.1
B_{3u}	IR	1099.6
B_{3u}	IR	1278.1
B_{3u}	IR	1582.4
B_{3u}	IR	1642.5
B_{3u}	IR	1867.9
A_u	Silent	204.7
A_u	Silent	1300.5
A_u	Silent	1600.0
A_u	Silent	1953.2

Table D.4: Raman and IR modes of the $Cmcm$ phase at 200 GPa.

Mode	Character	Frequency (cm ⁻¹)
A_g	Raman	681.3
A_g	Raman	1107.5
A_g	Raman	1494.7
A_g	Raman	1555.2
A_g	Raman	1714.7
A_g	Raman	1902.5
A_g	Raman	2268.8
B_{1g}	Raman	392.2
B_{1g}	Raman	442.9
B_{1g}	Raman	789.9
B_{1g}	Raman	1535.7
B_{1g}	Raman	1880.6
B_{1g}	Raman	2117.9
B_{1g}	Raman	2177.9
B_{2g}	Raman	612.9
B_{2g}	Raman	1311.1
B_{2g}	Raman	1440.8
B_{2g}	Raman	2134.5
B_{2g}	Raman	2218.5
B_{3g}	Raman	244.6
B_{3g}	Raman	321.6
B_{3g}	Raman	1320.5
B_{3g}	Raman	2130.6
B_{3g}	Raman	2185.8
B_{1u}	IR	178.3
B_{1u}	IR	278.2
B_{1u}	IR	1632.3
B_{1u}	IR	1874.6
B_{1u}	IR	2230.6
B_{2u}	IR	609.3
B_{2u}	IR	1542.0
B_{2u}	IR	1805.0
B_{2u}	IR	2135.7
B_{2u}	IR	2247.0
B_{3u}	IR	759.7
B_{3u}	IR	1064.2
B_{3u}	IR	1228.2
B_{3u}	IR	1508.9
B_{3u}	IR	1721.4
B_{3u}	IR	1893.3
B_{3u}	IR	2235.2
A_u	Silent	252.3
A_u	Silent	1519.7
A_u	Silent	1921.3
A_u	Silent	2293.6

Appendix E

Additional material for LiAlH₄

E.1 Structural data

In this section we list all atomic coordinates of the structures reported in section 4.4. Table E.1 lists the energies and the space group index of 10 structures containing AlH₄-frameworks. The first column indicates the structure index according to the energy ordering, linked to the list of coordinates provided subsequently in this section.

Table E.1: The energies and space group (SPG) numbers of the low-lying LiAlH₄ phases

Index	Symmetry	SPG index	ΔE (meV)	$\Delta E + \Delta ZPE$ (meV)
1	$P2_1/c$	14	-111.1	-63.7
2	$P2_1$	4	-82.6	-34.2
3	$Pnc2$	30	-81.9	-30.9
4	$P2_1/m$	11	-81.2	-32.4
5	$Cmmm$	65	-66.3	-15.4
6	$P-1$	2	-65.2	-12.2
7	$P2_1/c$	14	-64.4	-15.8
8	$P1$	1	-56.8	-4.2
9	$P2/c$	13	-54.1	-0.7
10	$P-42_1m$	113	-49.5	-1.9

Table E.2: Structure index 1, $P2_1/c$ phase of LiAlH₄.Lattice parameters: $a = 5.1617 \text{ \AA}$, $b = 4.2796 \text{ \AA}$, $c = 5.0837 \text{ \AA}$, $\alpha = \gamma = 90.0^\circ$, $\beta = 66.8382^\circ$

Element	x	y	z
Li1	0.50000	0.00000	0.00000
Al1	0.00000	0.00000	0.50000
H1	-0.13071	0.22290	-0.18004
H2	0.31588	0.17529	0.37445

Table E.3: Structure index 2, $P2_1$ phase of LiAlH₄.Lattice parameters: $a = 8.9522 \text{ \AA}$, $b = 4.2573 \text{ \AA}$, $c = 5.6512 \text{ \AA}$, $\alpha = \gamma = 90.0^\circ$, $\beta = 72.1798^\circ$

Element	x	y	z
Li1	0.37461	-0.28109	-0.06017
Li2	-0.12449	-0.28728	0.17229
Al1	0.12438	0.21974	0.31108
Al2	-0.37430	0.21173	-0.44003
H1	0.22047	0.41440	0.05001
H2	-0.27635	0.43413	-0.26440
H3	-0.02781	-0.47809	-0.14526
H4	-0.47209	-0.00541	0.38427
H5	-0.22185	-0.08229	-0.49594
H6	-0.46930	0.03899	-0.17030
H7	0.27817	-0.11330	-0.29156
H8	-0.02611	-0.48378	0.41001

Table E.4: Structure index 3, $Pnc2$ phase of LiAlH₄.Lattice parameters: $a = 4.7435 \text{ \AA}$, $b = 4.2166 \text{ \AA}$, $c = 5.1015 \text{ \AA}$, $\alpha = \beta = \gamma = 90.0^\circ$

Element	x	y	z
Li1	0.00000	0.00000	0.46670
Al1	0.50000	0.00000	0.15681
H1	-0.19723	0.29855	-0.31621
H2	-0.35599	-0.25401	-0.08131

Table E.5: Structure index 4, $P2_1/m$ phase of LiAlH_4 .Lattice parameters: $a = 6.6334 \text{ \AA}$, $b = 6.0095 \text{ \AA}$, $c = 5.6475 \text{ \AA}$, $\alpha = \gamma = 90.0^\circ$, $\beta = 114.2789^\circ$

Element	x	y	z
Li1	0.24063	0.25000	-0.38651
Li2	-0.25260	0.25000	-0.38848
Al1	-0.24879	0.25000	0.13393
Al2	0.25209	0.25000	0.11282
H1	0.42832	0.25000	0.42620
H2	0.04258	0.25000	0.23618
H3	0.45710	0.25000	-0.00978
H4	0.06261	0.25000	-0.19183
H5	-0.25945	0.05289	-0.10712
H6	0.24023	-0.44500	-0.35125

Table E.6: Structure index 5, $Cmmm$ phase of LiAlH_4 .Lattice parameters: $a = 6.4901 \text{ \AA}$, $b = 5.8844 \text{ \AA}$, $c = 2.7557 \text{ \AA}$, $\alpha = \beta = \gamma = 90.0^\circ$

Element	x	y	z
Li1	0.00000	0.00000	0.00000
Al1	0.50000	0.00000	0.50000
H1	0.00000	-0.21522	0.50000
H2	-0.32249	0.00000	0.00000

Table E.7: Structure index 6, $P-1$ phase of LiAlH_4 .Lattice parameters: $a = 2.7569 \text{ \AA}$, $b = 4.3541 \text{ \AA}$, $c = 4.3787 \text{ \AA}$, $\alpha = 95.0297^\circ$, $\beta = 84.5438^\circ$, $\gamma = 90.0033^\circ$

Element	x	y	z
Li1	0.00000	0.00000	0.00000
Al1	0.50000	0.50000	0.50000
H1	-0.00001	-0.32244	0.32242
H2	-0.49997	-0.21517	-0.21524

Table E.8: Structure index 7, $P2_1/c$ phase of LiAlH₄.Lattice parameters: $a = 6.8369 \text{ \AA}$, $b = 4.6187 \text{ \AA}$, $c = 6.5976 \text{ \AA}$, $\alpha = \gamma = 90.0^\circ$, $\beta = 100.8716^\circ$

Element	x	y	z
Li1	0.35392	-0.24393	-0.35675
Al1	-0.17790	-0.24612	0.19125
H1	-0.29783	0.43923	-0.39057
H2	-0.39237	-0.07112	-0.30750
H3	0.16886	0.11659	-0.44669
H4	-0.05444	0.42903	0.29655

Table E.9: Structure index 8, $P1$ phase of LiAlH₄.Lattice parameters: $a = 4.2763 \text{ \AA}$, $b = 5.1905 \text{ \AA}$, $c = 9.4717 \text{ \AA}$, $\alpha = 102.6938$, $\beta = 91.9368^\circ$, $\gamma = 90.2980^\circ$

Element	x	y	z
Li1	-0.29613	-0.18745	0.40694
Li2	0.19162	-0.11230	0.16033
Li3	0.20938	0.10289	-0.08504
Li4	0.21769	-0.26712	-0.34354
Al1	-0.28125	0.19784	-0.33837
Al2	-0.30497	0.41083	0.15726
Al3	0.20640	0.31589	0.41019
Al4	-0.30247	-0.39101	-0.09449
H1	-0.48570	-0.07398	-0.41639
H2	0.46523	-0.39050	0.05804
H3	0.44437	-0.21419	-0.16873
H4	-0.04326	0.23458	0.24865
H5	-0.09061	0.38046	-0.00357
H6	0.46312	0.48981	0.31524
H7	-0.10963	-0.30655	0.23017
H8	0.02576	-0.39915	0.47444
H9	-0.06258	0.14953	-0.49869
H10	-0.01361	0.03711	-0.25810
H11	0.45395	0.38823	-0.42862
H12	0.38507	0.03168	0.34270
H13	-0.04833	-0.15380	-0.01479
H14	0.46421	0.14947	0.08833
H15	0.49783	0.30261	-0.18179
H16	-0.09190	-0.49348	-0.25847

Table E.10: Structure index 9, $P2/c$ phase of LiAlH_4 .Lattice parameters: $a = 4.3574 \text{ \AA}$, $b = 5.1743 \text{ \AA}$, $c = 4.5446 \text{ \AA}$, $\alpha = \gamma = 90.0^\circ$, $\beta = 93.2116^\circ$

Element	x	y	z
Li1	0.50000	0.34696	0.25000
Al1	0.00000	-0.15966	0.25000
H1	-0.21018	0.10659	0.07092
H2	-0.25348	-0.36711	0.09608

Table E.11: Structure index 10, $P-42_1m$ phase of LiAlH_4 .Lattice parameters: $a = b = 4.2377 \text{ \AA}$, $c = 5.6650 \text{ \AA}$, $\alpha = \beta = \gamma = 90.0^\circ$

Element	x	y	z
Li1	0.00000	0.50000	0.38938
Al1	0.00000	0.50000	-0.12818
H1	0.30049	0.80049	-0.10235
H2	0.30535	0.80535	0.34141

E.2 Neutron diffraction

Figure E.1 shows the simulated and experimental neutron diffraction pattern of the p - $P2_1/c$ and α -LiAlH₄ phase, respectively.

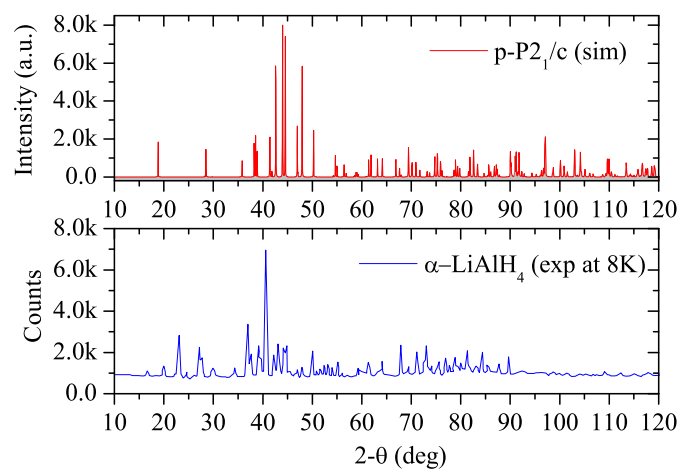


Figure E.1: Simulated and experimental (from Ref. [227]) neutron diffraction pattern are compared.

Bibliography

- [1] J. MADDOX, *Nature* **335**, 201 (1988).
- [2] M. A. NEUMANN, F. LEUSEN, and J. KENDRICK, *Angew. Chem. Int. Ed.* **47**, 2427 (2008).
- [3] G. M. DAY, T. G. COOPER, A. J. CRUZ-CABEZA, K. E. HEJCZYK, H. L. AMMON, S. X. M. BOERRIGTER, J. S. TAN, R. G. DELLA VALLE, E. VENUTI, J. JOSE, S. R. GADRE, G. R. DESIRAJU, T. S. THAKUR, B. P. VAN EIJCK, J. C. FACELLI, V. E. BAZTERRA, M. B. FERRARO, D. W. M. HOFMANN, M. A. NEUMANN, F. J. J. LEUSEN, J. KENDRICK, S. L. PRICE, A. J. MISQUITTA, P. G. KARAMERTZANIS, G. W. A. WELCH, H. A. SCHERAGA, Y. A. ARNAUTOVA, M. U. SCHMIDT, J. VAN DE STREEK, A. K. WOLF, and B. SCHWEIZER, *Acta Crystallogr. Sect. B* **65**, 107 (2009).
- [4] G. CEDER, *Science* **280**, 1099 (1998).
- [5] S. CURTAROLO, D. MORGAN, K. PERSSON, J. RODGERS, and G. CEDER, *Phys. Rev. Lett.* **91**, 135503 (2003).
- [6] G. CEDER and K. J. TIBBETTS, Data mining for structure type prediction, <http://dspace.mit.edu/handle/1721.1/34413>, 2004.
- [7] C. C. FISCHER, K. J. TIBBETTS, D. MORGAN, and G. CEDER, *Nature Mater.* **5**, 641 (2006).
- [8] S. GOEDECKER, *J. Chem. Phys.* **120**, 9911 (2004).
- [9] S. GOEDECKER, W. HELLMANN, and T. LENOSKY, *Phys. Rev. Lett.* **95**, 055501 (2005).
- [10] W. HELLMANN, R. G. HENNIG, S. GOEDECKER, C. J. UMRIGAR, B. DELLEY, and T. LENOSKY, *Phys. Rev. B* **75**, 085411 (2007).

-
- [11] A. WILLAND, M. GRAMZOW, S. A. GHASEMI, L. GENOVESE, T. DEUTSCH, K. REUTER, and S. GOEDECKER, *Phys. Rev. B* **81**, 201405 (2010).
- [12] S. DE, A. WILLAND, M. AMSLER, P. POCHE, L. GENOVESE, and S. GOEDECKER, *Phys. Rev. Lett.* **106**, 225502 (2011).
- [13] S. ROY, S. GOEDECKER, M. J. FIELD, and E. PENEV, *J. Phys. Chem. B* **113**, 7315 (2009).
- [14] K. BAO, S. GOEDECKER, K. KOGA, F. LANÇON, and A. NEELOV, *Phys. Rev. B* **79**, 041405 (2009).
- [15] S. A. GHASEMI, S. GOEDECKER, A. BARATOFF, T. LENOSKY, E. MEYER, and H. J. HUG, *Phys. Rev. Lett.* **100**, 236106 (2008).
- [16] P. POU, S. A. GHASEMI, P. JELINEK, T. LENOSKY, S. GOEDECKER, and R. PEREZ, *Nanotechnology* **20**, 264015 (2009).
- [17] M. AMSLER, S. A. GHASEMI, S. GOEDECKER, A. NEELOV, and L. GENOVESE, *Nanotechnology* **20**, 445301 (2009).
- [18] S. A. GHASEMI, M. AMSLER, R. G. HENNIG, S. ROY, S. GOEDECKER, T. J. LENOSKY, C. J. UMRIGAR, L. GENOVESE, T. MORISHITA, and K. NISHIO, *Phys. Rev. B* **81**, 214107 (2010).
- [19] M. AMSLER and S. GOEDECKER, *J. Chem. Phys.* **133**, 224104 (2010).
- [20] M. AMSLER, J. A. FLORES-LIVAS, L. LEHTOVAARA, F. BALIMA, S. A. GHASEMI, D. MACHON, S. PAILHÈS, A. WILLAND, D. CALISTE, S. BOTTI, A. SAN MIGUEL, S. GOEDECKER, and M. A. L. MARQUES, *Phys. Rev. Lett.* **108**, 065501 (2012).
- [21] J. A. FLORES-LIVAS, M. AMSLER, T. J. LENOSKY, L. LEHTOVAARA, S. BOTTI, M. A. L. MARQUES, and S. GOEDECKER, *Phys. Rev. Lett.* **108**, 117004 (2012).
- [22] M. AMSLER, J. A. FLORES-LIVAS, T. D. HUAN, S. BOTTI, M. A. L. MARQUES, and S. GOEDECKER, *Phys. Rev. Lett.* **108**, 205505 (2012).
- [23] M. AMSLER, J. A. FLORES-LIVAS, M. A. L. MARQUES, S. BOTTI, and S. GOEDECKER, *Eur. Phys. J. B* **86**, 1 (2013).
- [24] G. HENKELMAN and H. JÓNSSON, *J. Chem. Phys.* **113**, 9978 (2000).
- [25] B. PETERS, A. HEYDEN, A. T. BELL, and A. CHAKRABORTY, *J. Chem. Phys.* **120**, 7877 (2004).
- [26] W. E. W. REN, and E. VANDEN-EIJNDEN, *Phys. Rev. B* **66**, 052301 (2002).
- [27] W. E. W. REN, and E. VANDEN-EIJNDEN, *J. Chem. Phys.* **126**, 164103 (2007).

-
- [28] R. GRANOT and R. BAER, *J. Chem. Phys.* **128**, 184111 (2008).
- [29] S. A. GHASEMI and S. GOEDECKER, *J. Chem. Phys.* **135**, 014108 (2011).
- [30] D. WALES, *Energy Landscapes: Applications to Clusters, Biomolecules and Glasses*, Cambridge University Press, 1 edition, 2004.
- [31] R. S. BERRY, N. ELMACI, J. P. ROSE, and B. VEKHTER, *Proc. Natl. Acad. Sci. USA* **94**, 9520 (1997).
- [32] R. G. PARR and W. YANG, *Density-Functional Theory of Atoms and Molecules*, Oxford University Press, 1994.
- [33] R. M. MARTIN, *Electronic Structure: Basic Theory and Practical Methods*, Cambridge University Press, 2004.
- [34] P. HOHENBERG and W. KOHN, *Phys. Rev.* **136**, B864 (1964).
- [35] W. KOHN and L. J. SHAM, *Phys. Rev.* **140**, A1133 (1965).
- [36] J. P. PERDEW, *Phys. Rev. B* **33**, 8822 (1986).
- [37] C. LEE, W. YANG, and R. G. PARR, *Phys. Rev. B* **37**, 785 (1988).
- [38] A. D. BECKE, *Phys. Rev. A* **38**, 3098 (1988).
- [39] J. P. PERDEW, K. BURKE, and M. ERNZERHOF, *Phys. Rev. Lett.* **77**, 3865 (1996).
- [40] A. D. BECKE, *J. Chem. Phys.* **98**, 1372 (1993).
- [41] O. H. NIELSEN and R. M. MARTIN, *Phys. Rev. B* **32**, 3780 (1985).
- [42] V. FOCK, *Z. Phys. A-Hadron. Nucl.* **63**, 855 (1930).
- [43] J. TERSOFF, *Phys. Rev. B* **39**, 5566 (1989).
- [44] F. H. STILLINGER and T. A. WEBER, *Phys. Rev. B* **31**, 5262 (1985).
- [45] M. Z. BAZANT and E. KAXIRAS, *Phys. Rev. Lett.* **77**, 4370 (1996).
- [46] M. Z. BAZANT, E. KAXIRAS, and J. F. JUSTO, *Phys. Rev. B* **56**, 8542 (1997).
- [47] J. F. JUSTO, M. Z. BAZANT, E. KAXIRAS, V. V. BULATOV, and S. YIP, *Phys. Rev. B* **58**, 2539 (1998).
- [48] T. J. LENOSKY, B. SADIGH, E. ALONSO, V. V. BULATOV, T. D. RUBIA, J. KIM, A. F. VOTER, and J. D. KRESS, *Model. Simul. Mater. Sci. Eng.* **8**, 825 (2000).
- [49] M. I. BASKES, *Phys. Rev. Lett.* **59**, 2666 (1987).

-
- [50] T. J. LENOSKY, J. D. KRESS, I. KWON, A. F. VOTER, B. EDWARDS, D. F. RICHARDS, S. YANG, and J. B. ADAMS, *Phys. Rev. B* **55**, 1528 (1997).
- [51] L. GENOVESE, A. NEELOV, S. GOEDECKER, T. DEUTSCH, S. A. GHASEMI, A. WILLAND, D. CALISTE, O. ZILBERBERG, M. RAYSON, A. BERGMAN, and R. SCHNEIDER, *J. Chem. Phys.* **129**, 014109 (2008).
- [52] S. GOEDECKER, T. DEUTSCH, and L. BILLARD, *Phys. Rev. Lett.* **88**, 235501 (2002).
- [53] F. H. STILLINGER and T. A. WEBER, *Phys. Rev. A* **25**, 978 (1982).
- [54] F. H. STILLINGER and T. A. WEBER, *Science* **225**, 983 (1984).
- [55] F. H. STILLINGER, *Science* **267**, 1935 (1995).
- [56] A. R. OGANOV and M. VALLE, *J. Chem. Phys.* **130**, 104504 (2009).
- [57] D. SHEPPARD, P. XIAO, W. CHEMELEWSKI, D. D. JOHNSON, and G. HENKELMAN, *J. Chem. Phys.* **136**, 074103 (2012).
- [58] W. H. PRESS, B. P. FLANNERY, S. A. TEUKOLSKY, and W. T. VETTERLING, *Numerical Recipes in Fortran: The Art of Scientific Computing*, Cambridge University Press, 2 edition, 1992.
- [59] E. K. P. CHONG and S. H. ZAK, *An Introduction to Optimization, 2nd Edition*, Wiley, 2 edition, 2001.
- [60] E. BITZEK, P. KOSKINEN, F. GÄHLER, M. MOSELER, and P. GUMBSCH, *Phys. Rev. Lett.* **97**, 170201 (2006).
- [61] M. PROBERT, *J. Comput. Phys.* **191**, 130 (2003).
- [62] M. PARRINELLO and A. RAHMAN, *Phys. Rev. Lett.* **45**, 1196 (1980).
- [63] V. M. GOLDSCHMIDT, *Naturwissenschaften* **14**, 477 (1926).
- [64] D. G. PETTIFOR, *Solid State Commun.* **51**, 31 (1984).
- [65] D. G. PETTIFOR, *J. Phys. C: Solid State Phys.* **19**, 285 (1986).
- [66] R. O. DUDA and P. E. HART, *Pattern classification and scene analysis*, Wiley, 1973.
- [67] D. W. M. HOFMANN and J. APOSTOLAKIS, *J. Mol. Struct.* **647**, 17 (2003).
- [68] F. H. ALLEN, *Acta Crystallogr. Sect. B* **58**, 380 (2002).

-
- [69] H. ZENASNI, H. AOURAG, S. R. BRODERICK, and K. RAJAN, *Phys. Status Solidi B* **247**, 115 (2010).
- [70] P. V. BALACHANDRAN, S. R. BRODERICK, and K. RAJAN, *Proc. R. Soc. A* (2011).
- [71] S. R. BRODERICK, H. AOURAG, and K. RAJAN, *Physica B* **406**, 2055 (2011).
- [72] S. KIRKPATRICK, C. D. GELATT, and M. P. VECCHI, *Science* **220**, 671 (1983).
- [73] V. ČERNÝ, *J. Optimiz. Theory App.* **45**, 41 (1985).
- [74] M. W. DEEM and J. M. NEWSAM, *Nature* **342**, 260 (1989).
- [75] J. PANNETIER, J. BASSAS-ALSINA, J. RODRIGUEZ-CARVAJAL, and V. CAIGNAERT, *Nature* **346**, 343 (1990).
- [76] J. C. SCHÖN and M. JANSEN, *Angew. Chem. Int. Ed.* **35**, 1286 (1996).
- [77] F. JENSEN, *Introduction to Computational Chemistry*, Wiley, 1998.
- [78] P. SALAMON, P. SIBANI, and R. FROST, *Facts, Conjectures, and Improvements for Simulated Annealing*, Society for Industrial and Applied Mathematic, 2002.
- [79] J. C. SCHÖN and M. JANSEN, *Ber. Bunsenges. Phys. Chem.* **98**, 1541 (1994).
- [80] A. MÖBIUS, A. NEKLIODOV, A. DÍAZ-SÉNCHÉZ, K. H. HOFFMANN, A. FACHAT, and M. SCHREIBER, *Phys. Rev. Lett.* **79**, 4297 (1997).
- [81] A. MÖBIUS, K. HOFFMANN, and C. SCHÖN, Optimization by Thermal Cycling, pp. 215–219, World Scientific Publishing Co. Pte. Ltd., 2005.
- [82] P. SALAMON, J. D. NULTON, J. R. HARLAND, J. PEDERSEN, G. RUPPEINER, and L. LIAO, *Comput. Phys. Commun.* **49**, 423 (1988).
- [83] G. RUPPEINER, J. M. PEDERSEN, and P. SALAMON, *J. Phys. I* **1**, 455 (1991).
- [84] C. TSALLIS, *J. Stat. Phys.* **52**, 479 (1988).
- [85] C. TSALLIS and D. A. STARIOLO, *Physica A* **233**, 395 (1996).
- [86] G. DUECK and T. SCHEUER, *J. Comput. Phys.* **90**, 161 (1990).
- [87] A. LAIO and M. PARRINELLO, *Proc. Natl. Acad. Sci. USA* **99**, 12562 (2002).
- [88] R. MARTOŇÁK, A. LAIO, and M. PARRINELLO, *Phys. Rev. Lett.* **90**, 075503 (2003).
- [89] R. MARTOŇÁK, A. LAIO, M. BERNASCONI, C. CERIANI, P. RAITERI, F. ZIPOLI, and M. PARRINELLO, *Z. Kristallogr.* **220**, 489 (2005).

-
- [90] R. MARTOŇÁK, D. DONADIO, A. R. OGANOV, and M. PARRINELLO, *Nature Mater.* **5**, 623 (2006).
- [91] J. BEHLER, R. MARTOŇÁK, D. DONADIO, and M. PARRINELLO, *Phys. Status Solidi B* **245**, 2618 (2008).
- [92] D. J. WALES and J. P. K. DOYE, *J. Phys. Chem. A* **101**, 5111 (1997).
- [93] J. P. K. DOYE and D. J. WALES, *Phys. Rev. Lett.* **80**, 1357 (1998).
- [94] D. J. WALES and H. A. SCHERAGA, *Science* **285**, 1368 (1999).
- [95] Z. LI and H. A. SCHERAGA, *Proc. Natl. Acad. Sci. USA* **84**, 6611 (1987).
- [96] J. H. HOLLAND, *Adaptation in Natural and Artificial Systems: An Introductory Analysis with Applications to Biology, Control and Artificial Intelligence*, The University of Michigan Press, 1975.
- [97] D. E. GOLDBERG, *Genetic Algorithms in Search, Optimization, and Machine Learning*, Addison-Wesley Professional, 1 edition, 1989.
- [98] T. S. BUSH, C. R. A. CATLOW, and P. D. BATTLE, *J. Mater. Chem.* **5**, 1269 (1995).
- [99] J. MESTRES and G. E. SCUSERIA, *J. Comput. Chem.* **16**, 729 (1995).
- [100] D. M. DEAVEN and K. M. HO, *Phys. Rev. Lett.* **75**, 288 (1995).
- [101] D. DAVEN, N. TIT, J. MORRIS, and K. HO, *Chem. Phys. Lett.* **256**, 195 (1996).
- [102] J. A. NIESSE and H. R. MAYNE, *J. Chem. Phys.* **105**, 4700 (1996).
- [103] S. M. WOODLEY, P. D. BATTLE, J. D. GALE, and C. R. A. CATLOW, *Phys. Chem. Chem. Phys.* **1**, 2535 (1999).
- [104] B. HARTKE, Global geometry optimization of atomic and molecular clusters by genetic algorithms, in *Proceedings of the Genetic and Evolutionary Computation Conference (GECCO-2001)*, pp. 1284–1291, San Francisco, CA 94104, USA, 2001, Morgan Kaufmann.
- [105] B. HARTKE, Efficient Global Geometry Optimization of Atomic and Molecular Clusters, in *Global Optimization*, edited by J. D. PINTÉR and P. PARDALOS, volume 85 of *Nonconvex Optimization and Its Applications*, pp. 141–168, Springer, 2006.
- [106] N. L. ABRAHAM and M. I. J. PROBERT, *Phys. Rev. B* **73**, 224104 (2006).
- [107] A. R. OGANOV and C. W. GLASS, *J. Chem. Phys.* **124**, 244704 (2006).

-
- [108] C. W. GLASS, A. R. OGANOV, and N. HANSEN, *Comput. Phys. Commun.* **175**, 713 (2006).
- [109] G. TRIMARCHI and A. ZUNGER, *Phys. Rev. B* **75**, 104113 (2007).
- [110] A. R. OGANOV and A. O. LYAKHOV, *J. Superhard. Mater.* **32**, 143 (2010).
- [111] W. BI, Y. MENG, R. S. KUMAR, A. L. CORNELIUS, W. W. TIPTON, R. G. HENNIG, Y. ZHANG, C. CHEN, and J. S. SCHILLING, *Phys. Rev. B* **83**, 104106 (2011).
- [112] M. VALLE and A. R. OGANOV, Crystal Structures Classifier for an Evolutionary Algorithm Structure Predictor, in *IEEE Symposium on Visual Analytics Science and Technology*, pp. 11–18, 2008.
- [113] A. O. LYAKHOV, A. R. OGANOV, and M. VALLE, *Comput. Phys. Commun.* **181**, 1623 (2010).
- [114] S. E. SCHÖNBORN, S. GOEDECKER, S. ROY, and A. R. OGANOV, *J. Chem. Phys.* **130**, 144108 (2009).
- [115] G. GAO, A. R. OGANOV, A. BERGARA, M. MARTINEZ-CANALES, T. CUI, T. IITAKA, Y. MA, and G. ZOU, *Phys. Rev. Lett.* **101**, 107002 (2008).
- [116] Y. MA, M. EREMETS, A. R. OGANOV, Y. XIE, I. TROJAN, S. MEDVEDEV, A. O. LYAKHOV, M. VALLE, and V. PRAKAPENKA, *Nature* **458**, 182 (2009).
- [117] A. R. OGANOV, J. CHEN, C. GATTI, Y. MA, Y. MA, C. W. GLASS, Z. LIU, T. YU, O. O. KURAKEVYCH, and V. L. SOLOZHENKO, *Nature* **457**, 863 (2009).
- [118] Q. LI, Y. MA, A. R. OGANOV, H. WANG, H. WANG, Y. XU, T. CUI, H. K. MAO, and G. ZOU, *Phys. Rev. Lett.* **102**, 175506 (2009).
- [119] M. MARTINEZ-CANALES, A. R. OGANOV, Y. MA, Y. YAN, A. O. LYAKHOV, and A. BERGARA, *Phys. Rev. Lett.* **102**, 087005 (2009).
- [120] X. ZHOU, A. R. OGANOV, X. DONG, L. ZHANG, Y. TIAN, and H. WANG, *Phys. Rev. B* **84**, 054543 (2011).
- [121] G. GAO, A. R. OGANOV, P. LI, Z. LI, H. WANG, T. CUI, Y. MA, A. BERGARA, A. O. LYAKHOV, T. IITAKA, and G. ZOU, *Proc. Natl. Acad. Sci. USA* **107**, 1317 (2010).
- [122] Y. XIE, A. R. OGANOV, and Y. MA, *Phys. Rev. Lett.* **104**, 177005 (2010).
- [123] A. R. OGANOV, Y. MA, Y. XU, I. ERREA, A. BERGARA, and A. O. LYAKHOV, *Proc. Natl. Acad. Sci. USA* **107**, 7646 (2010).

-
- [124] J. KENNEDY and R. EBERHART, Particle swarm optimization, in *IEEE International Conference on Neural Networks, 1995. Proceedings*, volume 4, pp. 1942–1948 vol.4, IEEE, 1995.
- [125] J. KENNEDY and R. EBERHART, A New Optimizer Using Particle Swarm Theory, in *IEEE International Conference on Neural Networks, 1995. Proceedings*, volume 4, pp. 1942–1948 vol.4, IEEE, 1995.
- [126] Y. WANG, J. LV, L. ZHU, and Y. MA, *Phys. Rev. B* **82**, 094116 (2010).
- [127] P. LI, G. GAO, Y. WANG, and Y. MA, *J. Phys. Chem. C* **114**, 21745 (2010).
- [128] L. ZHU, H. WANG, Y. WANG, J. LV, Y. MA, Q. CUI, Y. MA, and G. ZOU, *Phys. Rev. Lett.* **106**, 145501 (2011).
- [129] C. L. GUILLAUME, E. GREGORYANZ, O. DEGTYAREVA, M. I. MCMAHON, M. HANFLAND, S. EVANS, M. GUTHRIE, S. V. SINOGEIKIN, and H. MAO, *Nature Phys.* **7**, 211 (2011).
- [130] J. LV, Y. WANG, L. ZHU, and Y. MA, *Phys. Rev. Lett.* **106**, 015503 (2011).
- [131] Y. WANG, H. LIU, J. LV, L. ZHU, H. WANG, and Y. MA, *Nat. Commun.* **2**, 563 (2011).
- [132] L. ZHU, Z. WANG, Y. WANG, G. ZOU, H.-K. MAO, and Y. MA, *Proc. Natl. Acad. Sci. USA* **109**, 751 (2012).
- [133] R. L. ANDERSON, *J. Am. Stat. Assoc.* **48**, 789 (1953).
- [134] L. A. RASTRIGIN, *Avtomatika i Telemekhanika* **24**, 1467 (1963).
- [135] L. A. RASTRIGIN, *Automat. Rem. Contr.* **24**, 1337 (1964).
- [136] K. DEAN C., *Automatica* **1**, 111 (1963).
- [137] F. J. SOLIS and R. J. WETS, *Math. Oper. Res.* **6**, 19 (1981).
- [138] J. C. SPALL, *Introduction to Stochastic Search and Optimization*, Wiley, 1 edition, 2003.
- [139] C. J. PICKARD and R. J. NEEDS, *Phys. Rev. Lett.* **97**, 045504 (2006).
- [140] A. ZHIGLJAVSKY and A. ZILINSKAS, *Stochastic Global Optimization*, Springer, 1 edition, 2007.
- [141] C. J. PICKARD and R. J. NEEDS, *J. Phys.: Condens. Matter* **23**, 053201 (2011).
- [142] S. ROY, S. GOEDECKER, and V. HELLMANN, *Phys. Rev. E* **77**, 056707 (2008).

-
- [143] M. SICHER, S. MOHR, and S. GOEDECKER, *J. Chem. Phys.* **134**, 044106 (2011).
- [144] M. JI, C. WANG, and K. HO, *Phys. Chem. Chem. Phys.* **12**, 11617 (2010).
- [145] T. BUČKO, J. HAFNER, and J. G. ÁNGYÁN, *J. Chem. Phys.* **122**, 124508 (2005).
- [146] A. R. OGANOV and C. W. GLASS, *J. Phys.: Condens. Matter* **20**, 064210 (2008).
- [147] T. HAHN, editor, *International Tables for Crystallography, Volume A, Space-Group Symmetry*, Wiley, 5 edition, 2005.
- [148] V. URUSOV and T. NADEZHINA, *J. Struct. Chem.* **50**, 22 (2009).
- [149] F. WOOTEN, K. WINER, and D. WEAIRE, *Phys. Rev. Lett.* **54**, 1392 (1985).
- [150] J. C. JAMIESON, *Science* **139**, 762 (1963).
- [151] J. Z. HU and I. L. SPAIN, *Solid State Commun.* **51**, 263 (1984).
- [152] H. OLJNYK, S. SIKKA, and W. HOLZAPFEL, *Phys. Lett. A* **103**, 137 (1984).
- [153] M. I. MCMAHON and R. J. NELMES, *Phys. Rev. B* **47**, 8337 (1993).
- [154] L. L. BOYER, E. KAXIRAS, J. L. FELDMAN, J. Q. BROUGHTON, and M. J. MEHL, *Phys. Rev. Lett.* **67**, 715 (1991).
- [155] D. WEAIRE and R. PHELAN, *Phil. Mag. Lett.* **69**, 107 (1994).
- [156] G. B. ADAMS, M. O'KEEFFE, A. A. DEMKOV, O. F. SANKEY, and Y. HUANG, *Phys. Rev. B* **49**, 8048 (1994).
- [157] T. F. MIDDLETON, J. HERNÁNDEZ-ROJAS, P. N. MORTENSON, and D. J. WALES, *Phys. Rev. B* **64**, 184201 (2001).
- [158] D. J. WALES, Cambridge Cluster Database, <http://www-wales.ch.cam.ac.uk/CCD.html>.
- [159] J. E. JONES, *Proc. R. Soc. Lond. A* **106**, 463 (1924).
- [160] S. D. STODDARD and J. FORD, *Phys. Rev. A* **8**, 1504 (1973).
- [161] J. R. FERNÁNDEZ and P. HARROWELL, *J. Chem. Phys.* **120**, 9222 (2004).
- [162] F. P. BUNDY, *J. Chem. Phys.* **46**, 3437 (1967).
- [163] A. F. GONCHAROV, I. N. MAKARENKO, and S. M. STISHOV, *Sov. Phys. JETP* **69**, 380 (1989).
- [164] M. HANFLAND, H. BEISTER, and K. SYASSEN, *Phys. Rev. B* **39**, 12598 (1989).

-
- [165] W. UTSUMI and T. YAGI, *Science* **252**, 1542 (1991).
- [166] Y. X. ZHAO and I. L. SPAIN, *Phys. Rev. B* **40**, 993 (1989).
- [167] T. YAGI, W. UTSUMI, M.-A. YAMAKATA, T. KIKEGAWA, and O. SHIMOMURA, *Phys. Rev. B* **46**, 6031 (1992).
- [168] W. L. MAO, H.-K. MAO, P. J. ENG, T. P. TRAINOR, M. NEWVILLE, C.-C. KAO, D. L. HEINZ, J. SHU, Y. MENG, and R. J. HEMLEY, *Science* **302**, 425 (2003).
- [169] F. J. RIBEIRO, S. G. LOUIE, M. L. COHEN, and P. TANGNEY, *Phys. Rev. B* **72**, 214109 (2005).
- [170] K. UMEMOTO, R. M. WENTZCOVITCH, S. SAITO, and T. MIYAKE, *Phys. Rev. Lett.* **104**, 125504 (2010).
- [171] J. T. WANG, C. CHEN, and Y. KAWAZOE, *Phys. Rev. Lett.* **106**, 075501 (2011).
- [172] A. R. OGANOV, *Modern Methods of Crystal Structure Prediction*, Wiley, 1 edition, 2010.
- [173] X. GONZE, G. RIGNANESE, M. VERSTRAETE, J. BEUKEN, Y. POUILLON, R. CARACAS, F. JOLLET, M. TORRENT, G. ZERAH, M. MIKAMI, P. GHOSEZ, M. VEITHEN, J. RATY, V. OLEVANO, F. BRUNEVAL, L. REINING, R. GODBY, G. ONIDA, D. HARMANN, and D. ALLAN, *Z. Kristallogr.* **220**, 558 (2005).
- [174] F. BOTTIN, S. LEROUX, A. KNYAZEVA, and G. ZÉRAH, *Comp. Mater. Sci.* **42**, 329 (2008).
- [175] J. P. PERDEW, A. RUZSINSZKY, G. I. CSONKA, O. A. VYDROV, G. E. SCUSE-RIA, L. A. CONSTANTIN, X. ZHOU, and K. BURKE, *Phys. Rev. Lett.* **100**, 136406 (2008).
- [176] C. HARTWIGSEN, S. GOEDECKER, and J. HUTTER, *Phys. Rev. B* **58**, 3641 (1998).
- [177] H. J. MONKHORST and J. D. PACK, *Phys. Rev. B* **13**, 5188 (1976).
- [178] R. H. BAUGHMAN, A. Y. LIU, C. CUI, and P. J. SCHIELDS, *Synth. Met.* **86**, 2371 (1997).
- [179] X. GONZE and C. LEE, *Phys. Rev. B* **55**, 10355 (1997).
- [180] S. BARONI, S. DE GIRONCOLI, A. DAL CORSO, and P. GIANNOZZI, *Rev. Mod. Phys.* **73**, 515 (2001).
- [181] F. GAO, J. HE, E. WU, S. LIU, D. YU, D. LI, S. ZHANG, and Y. TIAN, *Phys. Rev. Lett.* **91**, 015502 (2003).

-
- [182] W. G. AULBUR, L. JÖNSSON, J. W. WILKINS, H. EHRENREICH, and F. SPAEPEN, Quasiparticle Calculations in Solids, in *Solid State Physics*, volume 54, pp. 1–218, Academic Press, 1999.
- [183] F. OCCELLI, P. LOUBEYRE, and R. LETOULLEC, *Nat. Mater.* **2**, 151 (2003).
- [184] V. BRAZHKIN, N. DUBROVINSKAIA, M. NICOL, N. NOVIKOV, R. RIEDEL, V. SOLOZHENKO, and Y. ZHAO, *Nat. Mater.* **3**, 576 (2004).
- [185] V. L. SOLOZHENKO, O. O. KURAKEVYCH, and A. Y. KUZNETSOV, *J. Appl. Phys.* **102**, 063509 (2007).
- [186] J. A. FLORES-LIVAS, L. LEHTOVAARA, M. AMSLER, S. GOEDECKER, S. PAILHÈS, S. BOTTI, A. SAN MIGUEL, and M. A. L. MARQUES, *Phys. Rev. B* **85**, 155428 (2012).
- [187] S. PRAWER, K. NUGENT, D. JAMIESON, J. ORWA, L. BURSILL, and J. PENG, *Chem. Phys. Lett.* **332**, 93 (2000).
- [188] T. IRIFUNE, A. KURIO, S. SAKAMOTO, T. INOUE, and H. SUMIYA, *Nature* **421**, 599 (2003).
- [189] N. W. ASHCROFT, *Phys. Rev. Lett.* **21**, 1748 (1968).
- [190] M. LÜDERS, M. A. L. MARQUES, N. N. LATHIOTAKIS, A. FLORIS, G. PROFETA, L. FAST, A. CONTINENZA, S. MASSIDDA, and E. K. U. GROSS, *Phys. Rev. B* **72**, 024545 (2005).
- [191] M. A. L. MARQUES, M. LÜDERS, N. N. LATHIOTAKIS, G. PROFETA, A. FLORIS, L. FAST, A. CONTINENZA, E. K. U. GROSS, and S. MASSIDDA, *Phys. Rev. B* **72**, 024546 (2005).
- [192] P. CUDAZZO, G. PROFETA, A. SANNA, A. FLORIS, A. CONTINENZA, S. MASSIDDA, and E. K. U. GROSS, *Phys. Rev. Lett.* **100**, 257001 (2008).
- [193] J. M. McMAHON and D. M. CEPERLEY, *Phys. Rev. B* **84**, 144515 (2011).
- [194] R. SZCZĘŚNIAK and M. JAROSIK, *Solid State Commun.* **149**, 2053 (2009).
- [195] P. LOUBEYRE, F. OCCELLI, and R. LETOULLEC, *Nature* **416**, 613 (2002).
- [196] M. STÄDELE and R. M. MARTIN, *Phys. Rev. Lett.* **84**, 6070 (2000).
- [197] N. W. ASHCROFT, *Phys. Rev. Lett.* **92**, 187002 (2004).
- [198] J. FENG, W. GROCHALA, T. JAROŃ, R. HOFFMANN, A. BERGARA, and N. W. ASHCROFT, *Phys. Rev. Lett.* **96**, 017006 (2006).

- [199] Y. YAO, J. S. TSE, Y. MA, and K. TANAKA, *Europhys. Lett.* **78**, 37003 (2007).
- [200] X. J. CHEN, J. L. WANG, V. V. STRUZHKIN, H. K. MAO, R. J. HEMLEY, and H. Q. LIN, *Phys. Rev. Lett.* **101**, 077002 (2008).
- [201] D. Y. KIM, R. H. SCHEICHER, S. LEBÈGUE, J. PRASONGKIT, B. ARNAUD, M. ALOUANI, and R. AHUJA, *Proc. Natl. Acad. Sci. USA* **105**, 16454 (2008).
- [202] J. S. TSE, Y. YAO, and K. TANAKA, *Phys. Rev. Lett.* **98**, 117004 (2007).
- [203] M. I. EREMETS, I. A. TROJAN, S. A. MEDVEDEV, J. S. TSE, and Y. YAO, *Science* **319**, 1506 (2008).
- [204] X. CHEN, V. V. STRUZHKIN, Y. SONG, A. F. GONCHAROV, M. AHART, Z. LIU, H.-K. MAO, and R. J. HEMLEY, *Proc. Natl. Acad. Sci. USA* **105**, 20 (2008).
- [205] O. DEGTYAREVA, J. E. PROCTOR, C. L. GUILLAUME, E. GREGORYANZ, and M. HANFLAND, *Solid State Commun.* **149**, 1583 (2009).
- [206] M. HANFLAND, J. E. PROCTOR, C. L. GUILLAUME, O. DEGTYAREVA, and E. GREGORYANZ, *Phys. Rev. Lett.* **106**, 095503 (2011).
- [207] X. JIN, X. MENG, Z. HE, Y. MA, B. LIU, T. CUI, G. ZOU, and H.-K. MAO, *Proc. Natl. Acad. Sci. USA* **107**, 9969 (2010).
- [208] X. GONZE, B. AMADON, P. ANGLADE, J. BEUKEN, F. BOTTIN, P. BOULANGER, F. BRUNEVAl, D. CALISTE, R. CARACAS, M. CÔTÉ, T. DEUTSCH, L. GENOVESE, P. GHOSEZ, M. GIANTOMASSI, S. GOEDECKER, D. HAMANN, P. HERMET, F. JOLLET, G. JOMARD, S. LEROUX, M. MANCINI, S. MAZEVET, M. OLIVEIRA, G. ONIDA, Y. POUILLON, T. RANGEL, G. RIGNANESE, D. SANGALLI, R. SHALTAF, M. TORRENT, M. VERSTRAETE, G. ZERAH, and J. ZWANZIGER, *Comput. Phys. Commun.* **180**, 2582 (2009).
- [209] C. J. PICKARD and R. J. NEEDS, *Nat. Phys.* **3**, 473 (2007).
- [210] S. J. DUCLOS, Y. K. VOHRA, and A. L. RUOFF, *Phys. Rev. Lett.* **58**, 775 (1987).
- [211] W. L. MCMILLAN, *Phys. Rev.* **167**, 331 (1968).
- [212] P. B. ALLEN and R. C. DYNES, *Phys. Rev. B* **12**, 905 (1975).
- [213] D. Y. KIM, R. H. SCHEICHER, C. J. PICKARD, R. J. NEEDS, and R. AHUJA, *Phys. Rev. Lett.* **107**, 117002 (2011).
- [214] A. KOKALJ, *Comp. Mater. Sci.* **28**, 155 (2003).
- [215] L. G. HECTOR JR and J. F. HERBST, *J. Phys.: Condens. Matter* **20**, 064229 (2008).

-
- [216] B. BOGDANOVIĆ and M. SCHWICKARDI, *J. Alloys Compd.* **253-254**, 1 (1997).
- [217] P. CHEN and M. ZHU, *Mater. Today* **11**, 36 (2008).
- [218] A. E. FINHOLT, A. C. BOND, and H. I. SCHLESINGER, *J. Am. Chem. Soc.* **69**, 1199 (1947).
- [219] J. CHEN, N. KURIYAMA, Q. XU, H. T. TAKESHITA, and T. SAKAI, *J. Phys. Chem. B* **105**, 11214 (2001).
- [220] H. BRINKS, B. HAUBACK, P. NORBY, and H. FJELLVÅG, *J. Alloys Compd.* **351**, 222 (2003).
- [221] J. BLOCK and A. P. GRAY, *Inorg. Chem.* **4**, 304 (1965).
- [222] P. CHEN, Z. XIONG, J. LUO, J. LIN, and K. L. TAN, *Nature* **420**, 302 (2002).
- [223] Z. XIONG, G. WU, J. HU, Y. LIU, P. CHEN, W. LUO, and J. WANG, *Adv. Funct. Mater.* **17**, 1137 (2007).
- [224] Z. XIONG, J. HU, G. WU, Y. LIU, and P. CHEN, *Catal. Today* **120**, 287 (2007).
- [225] Y. LIU, J. HU, G. WU, Z. XIONG, and P. CHEN, *J. Phys. Chem. C* **111**, 19161 (2007).
- [226] S. ORIMO, Y. NAKAMORI, J. R. ELISEO, A. ZÜTTEL, and C. M. JENSEN, *Chem. Rev.* **107**, 4111 (2007).
- [227] B. HAUBACK, H. BRINKS, and H. FJELLVÅG, *J. Alloys Compd.* **346**, 184 (2002).
- [228] O. M. LØVVIK, S. M. OPALKA, H. W. BRINKS, and B. C. HAUBACK, *Phys. Rev. B* **69**, 134117 (2004).
- [229] T. DYMOVA, D. ALEKSANDROV, V. KONOPLEV, T. SILIANA, and A. SIZAREVA, *Russ. J. Coord. Chem.* **20**, 263 (1994).
- [230] N. MAL'TSEVA and A. GOLOVANOVA, *Russ. J. Appl. Chem.* **73**, 747 (2000).
- [231] J. K. KANG, J. Y. LEE, R. P. MULLER, and W. A. GODDARD, *J. Chem. Phys.* **121**, 10623 (2004).
- [232] T. J. FRANKCOMBE and G. KROES, *Chem. Phys. Lett.* **423**, 102 (2006).
- [233] X. KE and C. CHEN, *Phys. Rev. B* **76**, 024112 (2007).
- [234] C. LEE and X. GONZE, *Phys. Rev. B* **51**, 8610 (1995).
- [235] J. HEYD, G. E. SCUSERIA, and M. ERNZERHOF, *J. Chem. Phys.* **118**, 8207 (2003).

- [236] J. PAIER, M. MARSMAN, K. HUMMER, G. KRESSE, I. C. GERBER, and J. G. ÁNGYÁN, *J. Chem. Phys.* **125**, 249901 (2006).
- [237] J. HEYD, G. E. SCUSERIA, and M. ERNZERHOF, *J. Chem. Phys.* **124**, 219906 (2006).
- [238] G. KRESSE and J. FURTHMÜLLER, *Phys. Rev. B* **54**, 11169 (1996).
- [239] R. F. W. BADER, *Atoms in Molecules: A Quantum Theory*, Oxford University Press, USA, 1994.
- [240] L. G. HECTOR, J. F. HERBST, W. WOLF, P. SAXE, and G. KRESSE, *Phys. Rev. B* **76**, 014121 (2007).
- [241] J. F. HERBST, L. G. HECTOR, and W. WOLF, *Phys. Rev. B* **82**, 024110 (2010).
- [242] M. P. BALOGH, C. Y. JONES, J. HERBST, L. G. HECTOR JR., and M. KUNDRAT, *J. Alloys Compd.* **420**, 326 (2006).
- [243] H. WU, *J. Am. Chem. Soc.* **130**, 6515 (2008).
- [244] E. C. ASHBY, G. J. BRENDEL, and H. E. REDMAN, *Inorg. Chem.* **2**, 499 (1963).
- [245] J. W. TURLEY and H. W. RINN, *Inorg. Chem.* **8**, 18 (1969).
- [246] E. ZINTL and A. HARDER, *Z. Phys. Chem.* **28**, 478 (1935).

Acknowledgments

I want to express my sincere and deep gratitude to my supervisor, Prof. Dr. Stefan Goedecker, for continuously encouraging and motivating me, and for giving me the unique opportunity to work on a highly interesting research topic in an inspiring environment. I also thank the other members of the thesis committee: Prof. Dr. Richard Needs and Dr. Luigi Genovese. I would like to thank Dr. Alireza S. Ghasemi for all the interesting discussions and useful advices, and José A. Flores-Livas for all the help during countless and long phone calls. I would like to thank Dr. Thomas Lenosky for providing his modified tight binding code, but even more for his inspiring ideas, and Prof. Dr. Artem Oganov for the helpful discussions. Furthermore, I would like to thank the secretaries of the Physics Department, Astrid Kalt and Barbara Kammermann, and Martin Jacquot and Damien Caliste for their technical support.

Curriculum Vitæ

Personal Data

Name: Maximilian Kei Amsler
Address: Oberwilerstrasse 124
4054 Basel
Switzerland
E-mail: m.amsler@unibas.ch
Date of birth: 29.09.1984
Place of birth: Tokyo, Japan
Nationality: Swiss
Marital status: Single

Education

06/2012 – present Postdoctoral researcher at the Basel University, Switzerland
10/2009 – 06/2012 Ph.D. in Computational Physics at the Basel University, Switzerland
09/2007 – 04/2009 M.Sc. in Physics at the Basel University, Switzerland
09/2004 – 09/2007 B.Sc. in Physics at the Basel University, Switzerland

List of Publications

Articles in peer-reviewed journals

- “Triatomic hydrogen in H-Cl binaries under moderate pressures”,
Amaury Mavel, **Maximilian Amsler**, Rafael Sarmiento-Pérez, Stefan Goedecker,
Silvana Botti, Miguel A.L. Marques, submitted
- “Minima hopping accelerated path search: an efficient method for finding complex
chemical reaction pathways”,
Bastian Schaefer, Stephan Mohr, **Maximilian Amsler**, Stefan Goedecker, accepted
for publication in *J. Chem. Phys.*
- Comment on “Towards Direct-Gap Silicon Phases by the Inverse Band Structure
Design Approach”,
Maximilian Amsler, José A. Flores-Livas, Silvana Botti, Miguel A.L. Marques,
Stefan Goedecker, accepted for publication in *Phys. Rev. Lett.* (2014)

- “Boron aggregation in the ground states of boron-carbon fullerenes”,
Stephan Mohr, Pascal Pochet, **Maximilian Amsler**, Bastian Schaefer, Ali Sadeghi,
Luigi Genovese, Stefan Goedecker, *Phys. Rev. B Rapid Comm.* **89**, 041404(R)
(2014)
- “Conducting boron sheets formed by the reconstruction of the α -boron (111) sur-
face”,
Maximilian Amsler, Silvana Botti, Miguel A.L. Marques, Stefan Goedecker, *Phys.*
Rev. Lett. **111**, 136101 (2013)
- “Sodium-gold binaries: novel structures for ionic compounds from ab initio struc-
tural search”,
Rafael Sarmiento-Pérez, Tiago F.T. Cerqueira, Irais Valencia-Jaime, **Maximilian**
Amsler, Stefan Goedecker, Aldo H. Romero, Silvana Botti, Miguel A. L. Marquess,
New J. of Phys. **15**, 115007 (2013)
- “Novel structural motif in low energy phases of $\text{NaSc}(\text{BH}_4)_4$ ”,
Tran Doan Huan, **Maximilian Amsler**, Silvana Botti, Miguel A. L. Marques, and
Stefan Goedecker, *J. Chem. Phys.* **140**, 124708 (2014)
- “The crystal structure of the p-type transparent conductive oxide CuBO_2 ”,
Tiago F.T. Cerqueira, Rafael Sarmiento-Pérez, Fabio Trani, **Maximilian Amsler**,
Stefan Goedecker, Miguel A. L. Marques, Silvana Botti, *MRS Comm.* **3**, 157 (2013)
- “Thermodynamic stability of alkali metal/zinc double-cation borohydrides at low
temperatures”,
Tran Doan Huan, **Maximilian Amsler**, Riccardo Sabatini, Vu Ngoc Tuoc, Nam
Ba Le, Lilia M. Woods, Nicola Marzari, and Stefan Goedecker, *Phys. Rev. B* **88**,
024108 (2013)
- Comment on “Topological Insulators in Ternary Compounds with a Honeycomb
Lattice”,
Maia G. Vergniory, Miguel A. L. Marques, Silvana Botti, **Maximilian Amsler**,
Stefan Goedecker, Eugene V. Chulkov, Arthur Ernst and Aldo. H. Romero, *Phys.*
Rev. Lett. **110**, 129701 (2013)
- “Low-Energy Polymeric Phases of Alanates”,
Tran Doan Huan, **Maximilian Amsler**, Miguel A. L. Marques, Silvana Botti,
Alexander Willand, Stefan Goedecker, *Phys. Rev. Lett.* **110**, 135502 (2013)
- “Carbon structures and defect-planes in diamond at high pressure”,
Silvana Botti, **Maximilian Amsler**, José A. Flores-Livas, Paul Ceria, Stefan Goedecker,
Miguel A. L. Marques, *Phys. Rev. B* **88**, 014102 (2013)

- “Prediction of a novel monoclinic carbon allotrope”,
Maximilian Amsler, José A. Flores-Livas, Silvana Botti, Miguel A.L. Marques, Stefan Goedecker, *Eur. Phys. J. B* **86**, 383 (2013)
- “Low-energy structure of zinc borohydride $\text{Zn}(\text{BH}_4)_2$ ”,
Tran Doan Huan, **Maximilian Amsler**, Vu Ngoc Tuoc, Alexander Willand, Stefan Goedecker, *Phys. Rev. B* **86**, 224110 (2012)
- “Low-energy silicon allotropes with strong absorption in the visible for photovoltaic applications”,
Silvana Botti, José A. Flores-Livas, **Maximilian Amsler**, Stefan Goedecker, Miguel A. L. Marques, *Phys. Rev. B, Rapid Comm.* **86**, 121204 (2012)
- “Raman activity of sp^3 carbon allotropes under pressure: A density functional theory study”,
José A. Flores-Livas, Lauri Lehtovaara, **Maximilian Amsler**, Stefan Goedecker, Stéphane Pailhès, Silvana Botti, Alfonso San Miguel, Miguel A.L. Marques, *Phys. Rev. B* **85**, 155428 (2012)
- “Novel structural motifs in low energy phases of LiAlH_4 ”,
Maximilian Amsler, José A. Flores-Livas, Tran Doan Huan, Silvana Botti, Miguel A.L. Marques, Stefan Goedecker, *Phys. Rev. Lett.*, **108**, 205505 (2012)
- “High pressure structures of disilane and their superconducting properties”,
José A. Flores-Livas, **Maximilian Amsler**, Thomas J. Lenosky, Lauri Lehtovaara, Silvana Botti, Miguel A.L. Marques, Stefan Goedecker, *Phys. Rev. Lett.* **108**, 117004 (2012)
- “Crystal structure of cold compressed graphite”,
Maximilian Amsler, José A. Flores-Livas, Lauri Lehtovaara, Felix Balima, Denis Machon, Stéphane Pailhès, Alexander Willand, Damien Caliste, Silvana Botti, Alfonso San Miguel, Stefan Goedecker, Miguel A.L. Marques, *Phys. Rev. Lett.* **108**, 065501 (2012)
- “Energy Landscape of Fullerene Materials: A Comparison of Boron to Boron Nitride and Carbon”,
Sandip De, Alexander Willand, **Maximilian Amsler**, Pascal Pochet, Luigi Genovese, Stefan Goedecker, *Phys. Rev. Lett.* **106**, 225502 (2011)
- “Crystal structure prediction using the minima hopping method”,
Maximilian Amsler, Stefan Goedecker, *J. Chem. Phys.* **133**, 224104 (2010)
- “Energy landscape of silicon systems and its description by force fields, tight binding schemes, density functional methods, and quantum Monte Carlo methods”,

S. Alireza Ghasemi, **Maximilian Amsler**, Richard G. Hennig, Shantanu Roy, Stefan Goedecker, Thomas J. Lenosky, C. J. Umrigar, Luigi Genovese, Tetsuya Morishita and Kengo Nishio, *Phys. Rev. B* **81**, 214107 (2010)

- “Adsorption of small NaCl clusters on surfaces of silicon nanostructures”, **Maximilian Amsler**, S. Alireza Ghasemi, Stefan Goedecker, Alexey Neelov and Luigi Genovese, *Nanotechnology* **20**, 445301 (2009)